Department of Earth Sciences
University College London (UCL)

Silicate Liquids in Extreme Conditions:
Giant Impacts and Super-Earth Interiors

Lee R. Bardon

Submitted in fulfillment of the requirements
for the degree of Master of Philosophy
at University College London

Dec 12th 2018

DECLARATION

I, Lee Richard Bardon, confirm that the work presented in this thesis is my own. Where information has been derived from other sources, I confirm that this has been indicated in the thesis.

ABSTRACT

In this work, I use first-principles molecular dynamics (FPMD) to examine the structural, thermodynamic and transport properties of silicate liquids in the extreme conditions associated with giant impacts and super-Earth interiors, with temperatures ranging between 3000 K and 20,000 K, and pressures of up to ~4 TPa. I focus primarily on $MgSiO_3$ liquid, with some initial results reported for the hydrated form of approximately 10 wt% water.

I found that mean Si-O coordination in $MgSiO_3$ increases linearly with pressure, from between 4 and 4.5 at upper Earth mantle conditions (~2 GPa), to between 6 and 6.5 in Earth's lower mantle (~130 GPa), and finally to between 8 and 8.5 in the conditions associated with super-Earth mantles and giant impacts (~2.5 to 3 TPa).

Average heat capacity, in the case of $MgSiO_3$ decreases on compression from ~4.6 N k at the reference volume of $V/V_x=1$ to ~3.35 N k at the highest compression level of $V/V_x=0.2$.

My analysis of self-diffusion over a very large pressure-temperature range may reveal the limitations of the Arrhenius form, when applied to self-diffusion in liquid silicates. Although the Arrhenius form describes diffusive behaviour across the T-P (temperature-pressure) regime of Earth's mantle, I discovered that self-diffusion coefficients in the conditions of super-Earth mantles are much larger than those obtained via Arrhenius extrapolation from lower-pressure. This suggests that chemical exchange between magma oceans and the crystals freezing out of them are not as limited as what once might have been thought.

This work represents the first step toward a complete set of results for all materials studied, including $MgSiO_3$, and hydrated $MgSiO_3$, across a wide temperature and pressure regime. The results may have important implications for our understanding of the behavior of silicate liquids in super-Earth magma oceans, and as the result of high velocity impacts. The work will motivate experimental studies of structure and physical properties of amorphous silicates over a wider pressure-temperature regime than has previously been explored.

IMPACT STATEMENT

The overarching goal of this thesis was to contribute to our understanding of how silicate liquids behave in the extreme conditions associated with planetary impact events and super-Earth mantles. Throughout my time on this project, I was involved with designing and implementing experiments, generating data, and analyzing and interpreting results. This lead to some valuable insights, particularly to other researchers within my own research field, but also to researchers more broadly involved with FPMD materials modelling who may wish explore the effects of ultra-high temperatures or pressures on their own experimental materials. Some of these insights were technical in nature, and derived from my attempts to adequately model silicate materials in extreme T-P regimes that have remained largely unexplored. In doing so, I identified some instances where existing analytical techniques proved inadequate.

For example, I noted that there were two popular methods for obtaining the heat capacity; the 'finite differences' method, and the 'fluctuations' method. 'Finite differences' allows from the heat capacity to be computed directly from FPMD results, but requires data from two simulation cells, and approximates the heat capacity at a temperature between the two. Conversely, the 'fluctuations' method can generate the heat capacity for any given simulation cell, but it requires that the researcher input some parameters from external models. I was keen to compare how each method performs across the T-P range of my own work. The two methods agreed well at temperatures below 10,000 K, but diverged at higher temperatures. On analysis, I identified that my group's method of estimating the electronic contribution to the heat capacity – as required by the 'fluctuations' method – broke down at high temperatures. A solution was engineered by R. Scipioni, and reported in Scipioni *et al.* 2017. Additionally, my self-diffusion analyses demonstrated that the method of linear extrapolation from lower temperature results does not yield accurate results.

Given the extreme conditions replicated in the current work, there are no clear commercial applications that could derive from my results. However, the study of silicate liquid properties in the conditions associated with Earth's mantle is of considerable importance to furthering our understanding of mantle dynamics and thermal evolution on Earth. These processes are linked to tectonic motion, to the transport properties of magma, and thus contribute to our understanding of volcanism and earthquakes.

Finally, while research of this nature may not have practical applications to commerce, and nor may it be particularly relevant to the great socio-political, economic, or technical challenges of our time, it is of paramount importance to our sense of wonder and curiosity about the universe around us, and our place within it. This is a powerful means of invoking a sense of perspective, and for encouraging us to face these great challenges together.

CONTENT

1. INTRODUCTION

Silicates are the most abundant materials on Earth; between them, silicon, oxygen and magnesium make up around 85% of the mantle, which itself comprises 2/3 of Earth's total mass (Robertson, 2007). These rock-forming materials are abundant throughout the rest of the solar system too, occupying a wide range of environments, from the freezing conditions at the surface of asteroids, to the extremely high temperature and pressure environments of the gas giant cores (Low et al., 1984; de Pater & Lissauer, 2015), with silicate materials thus occupying a corresponding range of physical states, from vapour, to liquid, to solid rock.

In the current work, we use first principles molecular dynamics (FPMD) to investigate thermodynamic properties and behaviours of fluid silicates. Here, we place an emphasis on extending the results of previous theoretical work spanning the conditions of Earth's mantle, into even higher pressure and temperature regimes; namely, those that are relevant to planetary impact events of a Moon-forming magnitude, and to the interior of super-Earth exoplanets.

Impacts are known to occur frequently as planetary systems accrete, stabilise and evolve (Ciesla et al., 2013). Although less frequent, giant impacts between planet-sized bodies also occur, and may be no less ubiquitous. Indeed, recent research by (Quintana et al., 2016) revealed that Earth-analogue planets orbiting Sun-like stars could expect to experience at least one giant impact during the first 2 Gyr of its evolution. When these cataclysmic events occur, they can generate large scale melting and vapourisation of both the target planet and the impactor, altering their thermal, chemical and dynamical evolution. Such an event is also the leading theory of Moon formation (Hartmann & Davis, 1975), although this scenario is complicated by the chemical and isotopic similarity of the Earth and the Moon. This implies that either the proto-Earth and its impactor were of almost identical composition (considered unlikely), or that extensive post-impact mixing occurred.

To gain some understanding of Earth's response to impacts - from post-impact mixing to the cooling and crystallization of magma oceans, and from liquid density and crystal buoyancy to melting points and phase transitions - we require an accurate understanding of the thermodynamic and transport properties of silicate materials in extreme conditions. However, while we have probed the temperature and pressure range of the Earth's mantle with both experimental and theoretical work, there is currently a paucity of data with respect to more extreme environments, due to the relative complexity of replicating these conditions.

What, more precisely, can we learn from directly studying silicates in extreme conditions? Let's look at density, in the first instance. Density is the primary factor that controls liquid silicate evolution at depth in the mantle, which guides us toward key questions over whether the melted material is less dense, or more dense than the surrounding solid, and thus whether is rises or remains trapped at depth. Certainly, there is seismological evidence of liquid silicates at the core-mantle boundary (Williams & Garnero, 1996), and theoretical evidence of the silicate liquid being denser than the coexisting solid in the same pressure-temperature regime (Stixrude & Karki, 2005). But how does this relationship look in the much higher P-T regimes of giant impacts and Super-Earth interiors, which themselves may go through an early magma-ocean stage, or giant impact events?

We can follow similar lines of reasoning with respect to extending previously-explored quantities into the extremes of pressure and temperature. For example, we can explore the behavior of the equation of state, which controls the response of the material to impacts, and determines crystal buoyancy; we can calculate and extend the Hugoniot curve for easy comparison to shock wave experiments, and we can investigate whether the Grünisen parameter of the liquid continues to increase on compression, as surprisingly identified by Stixrude & Karki (2005). How does the heat capacity behave with respect to increases in temperature? Does it decrease, as per the fundamental measure theory (Rosenfeld and Tarazona, 1998)? Does it increase with pressure? How does the coordination of key silicate bonds (such as Si-O) behave in the liquid under these conditions? Do we see a liquid-liquid phase transition in $MgSiO_3$ liquid over the range ~300-400GPa and 10,000 – 16,000K as per Spaulding et al., 2012 , or don't we? And what of chemical diffusion in the liquid? Does its behavior continue to follow the Arrhenian form, as it does in the lower pressure and temperature regimes of Earth's mantle (Nevins et al., 2009)? What if we include common volatiles such as H_2O alongside our exploration of bulk silicates – does this significantly change any of our results? Finally, is the concept of a silicate-dynamo valid (Ziegler & Stegman, 2013) with respect to the electrical conductivity of silicate liquids in extreme conditions? And, if so, is its strength affected by proton conductivity in hydrated silicate melts?

Constraining these thermodynamic and transport properties is key not only to understanding Moon-formation, but early-Earth's evolution too, particularly in terms of its differentiation into core, mantle and crust. In addition, further exploring how silicates behave in extreme conditions will also allow us to probe conditions in the interior of super-Earth exoplanets, which reach temperatures and pressures that are substantially greater than those in the interior of Earth.

We explore liquid silicates at pressures and temperatures ranging from 2 GPa to 4.5 TPa, and from 3000 K to 20,000 K by performing first principles molecular dynamics simulations using VASP. Our primary material of interest is $MgSiO_3$ liquid, selected both for its abundance in the Earth's mantle, and for the wealth of previous experimental and theoretical data across a broad range of *P* and *T* regimes. This is supplemented with some preliminary studies on $MgSiO_3$ liquid with added water (10 wt%).

2. BACKGROUND

In this section, we will briefly review a selection of the background research, as relevant to both giant impacts (with a focus on the proposed Moon-forming impact) and super-Earth interiors, drawing on a variety of evidence from observational, experimental, and theoretical research. The aim of this section is to familiarise the reader with the body of research leading up to that generated by the author, both in terms of the more general work associated with the field, and in terms of the specific sets of results we aim to reproduce, and then extend into the conditions of interest. However, before we do so, it is first necessary to gain some understanding of the temperature-pressure regime relevant to giant impacts and super-Earth interiors, in order to obtain reasonable constraints for our own investigation.

2.1 Giant Impacts & Super-Earths

The physical and chemical evolution of Earth-like planets proceeds via the gravitational separation of a liquid phase into dense, metallic core, rocky mantle, and atmosphere (Davies, 1982). Giant, high-velocity impacts that occur during the latter stages of planetary accretion are likely to generate large-scale melting and result in extensive magma oceans that may encompass much of the rocky mantle (Canup, 2012; Elkins-Tanton, 2012). Any further freezing of the magma ocean would lead to a vast increase in mantle viscosity (by 10 to 15 orders of magnitude – Stixrude, 2014), and thus considerably influence the planets thermal evolution, geochemistry and magnetic field. Understanding the effects of planetary melting and freezing processes on the magnetic field is regarded by some as especially important, due to its role in protecting any extant surface life (as-we-know-it) from high-energy solar radiation, which may act to strip planetary atmospheres of water-vapour and other gases necessary for the development and sustenance of life (Tarduno et al., 2015).

Academic dialogue surrounding planetary impact events tends to pay special attention to the formation of the Moon; the Moon is, after all, our closest and most familiar astronomical body, and has been the subject of folklore and mythology through human history. In the modern era, a number of competing theories have been proposed to explain the origin of Earth's Moon, ranging from the Moon being gravitationally captured by the proto-Earth (Gerstenkorn, 1969; Öpik, 1972; Mitler, 1975), to dual-accretion (a.k.a. co-formation) from the protoplanetary disk (e.g. Weidenschilling et al., 1986).

In more recent years, a range of compelling evidence has supported the 'giant impact hypothesis', whereby the Moon accreted from an equatorial circum-terrestrial disk following an impact event between the proto-Earth and a Mars-sized impactor (e.g. Hartman & Davis, 1975; Canup & Asphaug, 2001; Canup, 2004). This impact lead to a differentiated Moon by roughly 4.51 billion years ago (Barboni et al., 2017), according to the latest findings.

Several lines of evidence support this hypothesis. For example, we know from studying lunar rock samples and their isotopic composition, and from a wide range of simulations, that the two bodies are likely to have shared a common origin, and that the surface of the Moon was likely to once have been molten (Wood, 1972; Wiechart et al., 2001; Brandon, 2007; Elardo et al., 2011; Young et al, 2016). The Earth's spin and the orbital dynamics of the Moon are matched, also corroborating a giant impact origin (Morishima & Watanabe, 2004; Ćuk et al., 2016). The Moon has a mean density of 3344 kg/m^3 to the Earth's 5514 kg/m^3 (NASA), which giant impact proponents suggest is expected, as it follows the conclusion that any dense, iron-rich material of the impactor's core gravitationally merged with the iron core of Earth, leaving the Moon to accrete from less dense mantle material.

Finally, it helps to explain why other planets do not have similar moons, such that if evolutionary processes were responsible for the Earth-Moon system, we should expect to see similar systems appear more commonly elsewhere; instead, invoking a stochastic catastrophe explanation, such as giant impact events, may better explain what we observe (Hartmann, 1997).

The giant impact hypothesis is by no means uncontested, and the evidence for it remains incomplete. For example, if the Moon accreted from ejected material orbiting the Earth's equator, then the Moon should orbit in the plane of the ecliptic, when it is instead tilted five degrees off. This implies that, although models have been successful in matching the Moons mass and the rotational rates of Earth and the Moon, some unknown dynamical process – for example, subsequent impacts - must be invoked in order to explain orbital tilt (e.g. Touma & Wisdom, 1998; Ward & Canup, 2000; Pahlevan & Morbidelli, 2015).

In addition, lunar and Earth materials are more isotopically similar than what is expected in the aftermath of an impact that does not violate angular momentum constraints. In other words, impact-based models that most accurately replicate Earth-Moon masses and dynamics, are also those in which the impactor is the primary contributor to the Moons mass, so we should expect to see more clear chemical differentiation in the samples (Burkhardt, 2014; Young et al., 2016). Despite these inconsistencies, for the giant impact scenario to work, researchers have, to-date, invoked sets of very specific conditions, each of which further reduce the probability of the event.

These evidential gaps have led some researchers to provide updated and alternative impact-oriented solutions to the Moon's origin story, in order to account for these inconsistencies. Rufu et al., (2017) suggest that the Moon originated not from a single impact event, but from a series of smaller impacts during the solar system's tumultuous early evolution. From their numerical simulations, they demonstrate a scenario and a timescale whereby each collision creates a debris disk around the proto-Earth which then accretes to form a 'moonlet'. They find that sub-lunar moonlets occur commonly following smaller impacts that are expected to have been common in the early Solar System, and that planetary rotation limits the drain of impact angular momentum. Their concept then requires that the separate moonlets each advance outward from Earth tidally, before eventually merging to form the Moon as we know it today (Fig. 1).

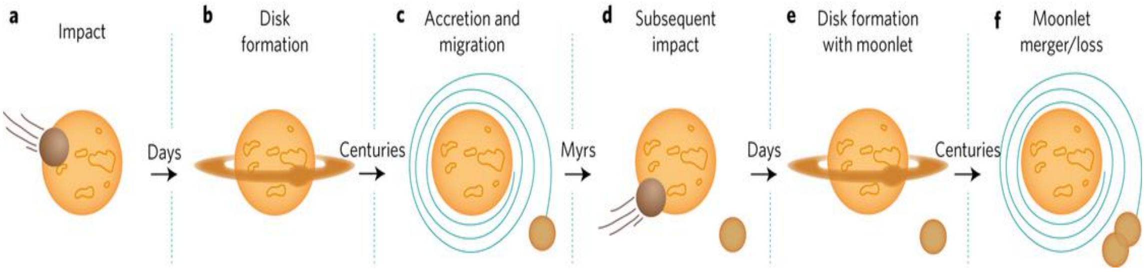

Figure 1: A multiple-impact origin for the Moon. A series of smaller impacts each create debris disks, which accrete into 'moonlets'. Moonlets migrate outward before eventually merging to become the Moon. Image from Rufu et al., (2017).

Meanwhile, Ćuk & Stewart (2012) and Ćuk et al., (2016) propose a variant of the single-impact origin in which Earth-Moon system is a product not of a single, glancing blow, but of an extremely high-velocity, high-energy, head-on collision. During this collision, the energy is such that the material from the proto-Earth and the impactor become highly mixed, accounting for the isotopic similarities that we see today. They find that an impact of this nature results initially with the accretion of the Moon from highly-mixed material in equatorial orbit around an initially fast-spinning, high-obliquity Earth. As their model evolves dynamically, the Moon's orbit is affected by solar perturbations, inducing the lunar inclination and lessening the angular momentum of the Earth-Moon system. Canup (2012) also explored Moon-formation with an extra-large impactor, showing that these can produce a disk with a composition similar to that of Earth's mantle, and suggested that angular momentum could be removed from the system via resonance with the Sun.

These latest Moon formation hypotheses therefore also support an impact origin, albeit with variations that attempt to negate prior inconsistencies. Thus, we consider it justifiable to use some of the more recent, and well-received studies in constraining the temperature-pressure environment of the current work. To model the Moon-forming giant impact, Canup (2004) conducts around 100 smooth particle hydrodynamic simulations; a Lagrangian technique whereby a large number of overlapping particles which are tracked over time (in terms of changes in e.g. position, velocity, internal energy) and used to represent a given material. They consider impactors and targets with a composition of 30% iron and 70% silicate (forsterite/dunite) by mass, differentiated into core and mantle, respectively, and include up to 120,000 particles per simulation.

In generating their initial conditions, one approach used by Canup (2004) was via collisional generation, whereby an iron particle is projected into a dunite target. For a nearly-Earth sized target with a nearly-Mars sized impactor, this process generates temperatures ranging between 2000 K and 20,000 K, which the authors state would be expected temperatures if a planet had recently experienced another large impact, or had cooled inefficiently (they call this a 'hot start' scenario). As such, although the simulations themselves generate post-impact silicate temperatures of between 2000 K to 10,000 K (Fig. 2), we select 20,000 K as the upper-bound temperature for our own work, to account for the possibility of a 'hot start'.

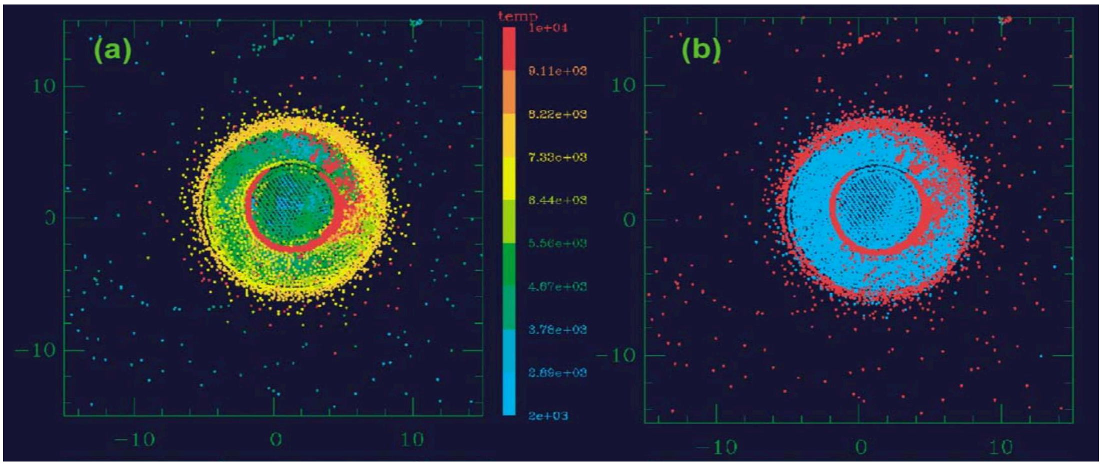

Figure 2: The post-impact proto-Earth. (a) The temperatures (K) of a 2000 km thick slice through the proto-Earth, parallel with the equatorial plane of the planet. (b) The same slice, however, in this case colour scales to particle origin, with the red particles originating from the impactor, and blue from the target. From Canup (2004).

To gain some understanding of the maximum pressures experienced by materials during impacts, we first turn to the Rankine-Hugoniot equations, first derived by W.J.M. Ranking (1870a, 1870b) and P.H. Hugoniot (1887, 1889). During an impact event, both the projectile and the target are compressed, generating strong shock waves. The Rankine-Hugoniot equations relate quantities in front of the shock (subscript 0) to quantities behind the shock (no subscript), as shown below:

$$\rho\left(U - u_p\right) = \rho_0 U \qquad [1]$$

$$P - P_0 = \rho_0 u_p U \qquad [2]$$

$$E - E_0 = \frac{1}{2}(P + P_0)\left(\frac{1}{\rho_0} - \frac{1}{\rho}\right) \qquad [3]$$

where P is pressure, ρ is density, u_p is particle velocity behind the shock, (any unshocked material is assumed to be at rest), U is shock velocity, and E is internal energy (per unit mass). Respectively, these relations represent the conservation of mass, momentum and energy across the shock front. In order to specify the outcome of (in this case) an impact, we must supplement these relations with an equation of state, which relates pressure, density and internal energy ($P = P(\rho, E)$) for all materials. When used in combination, we are able to compute the maximum pressure, particle velocity and shock velocity of a given impact (Melosh, 1989).

Table 1: Maximum shock pressures in vertical impacts. From Melosh (2013).

Impact Velocity (km/s)	**Pressure (GPa)**		
	Iron on Basalt	*Basalt on Basalt*	*Serpentinite on Ice*
5	78	48	22
7.5	150	93	44
10	250	150	73
15	500	320	160
30	1800	1200	580
45	3900	2500	1300

Stixrude (2014) explored the melting of silicate materials both as a response to giant impacts, and in the interior of super-Earths. Following Tonks and Melosh (1993), the author selected dunite as a reasonable and convenient analogue material for the rocky component of planetary mantles, primarily because its Hugoniot is well-characterised and studied. They found that the isobaric core of the impact (an internal tangent sphere with a radius equal to that of the impactor) is entirely melted following an impact with a critical velocity of just 8.6 km/s (Fig. 3). This is equivalent to the escape velocity for a planet of just $0.5M_{\oplus}$ (Earth masses), and is a low velocity compared with typical impact velocities of late-stage accretion, which, according to the Nice model (Gomes et al., (2005)), was approximately $21 - 25\ \mathrm{km/s}$. Thus, we can feasibly justify an exploration of impact-generated fluid silicates within a pressure-temperature regime constrained up to 20,000 K, and up to several TPa.

The analysis of Tonks & Melosh (1993) was also applied by Stixrude (2014) to understanding impact melting in more general terms, taking into account a wide range of rocky-planet masses – from sub-Earth to super-Earth - and the possibility of impacts occurring during accretion and heating the proto-planets, and concluded that many super-Earths may be entirely molten by the end of accretion.

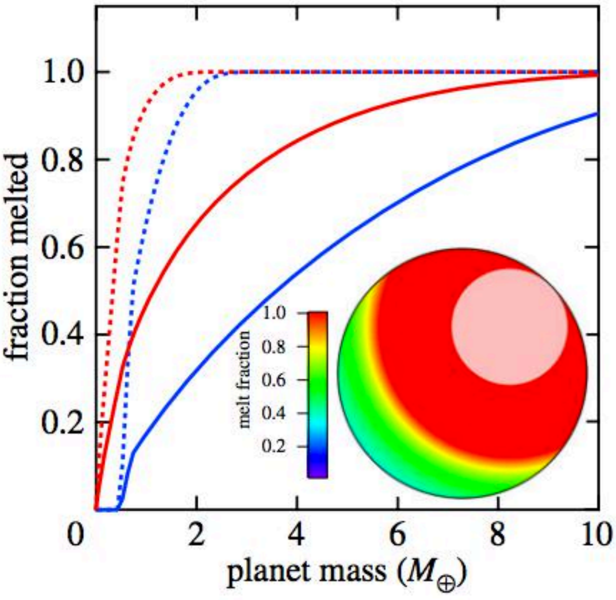

Figure 3: The fraction of planetary mass melted during impact as a function of planetary mass, assuming the minimal impact velocity of 11.2 km/s. $\frac{M_i}{M_P} = 0.1$ *for solid lines and* $\frac{M_i}{M_P} = 0.4$ *for dashed lines (where* M_i *and* M_p *are impactor and planet mass, respectively). The blue lines represent an initial temperature of 300 K while the red lines are the solidus temperature. Inset bottom right is the distribution of melt fraction for* $M_p = 5M_\oplus$, $\frac{M_i}{M_P} = 0.1$ *and initial temperature is at the solidus temperature. The pink circle is entirely molten. From Stixrude (2014).*

But what are the conditions experienced by materials in the *interior* of super-Earth exoplanets, and do we expect silicate materials to occupy a fluid state in these extreme pressure environments, even at temperatures as high as 20,000 K? To gain some understanding, particularly in terms of constraining the pressure-temperature regime of super-Earth interiors, we turn to the example of previous theoretical and experimental work in the literature. Among the more recent experimental studies, Millot et al., (2015) used laser-driven shock experiments to emulate the pressure and temperature conditions expected within rocky exoplanets, ranging from $1\ M_\oplus$ to roughly $15\ M_\oplus$. Here, they expose a variety of Earth materials (namely fused silica, α-quartz and stishovite) to intense laser-driven shock compression, obtaining pressure-density data for up to 2.5 TPa and several tens of thousands of Kelvin (Fig. 4).

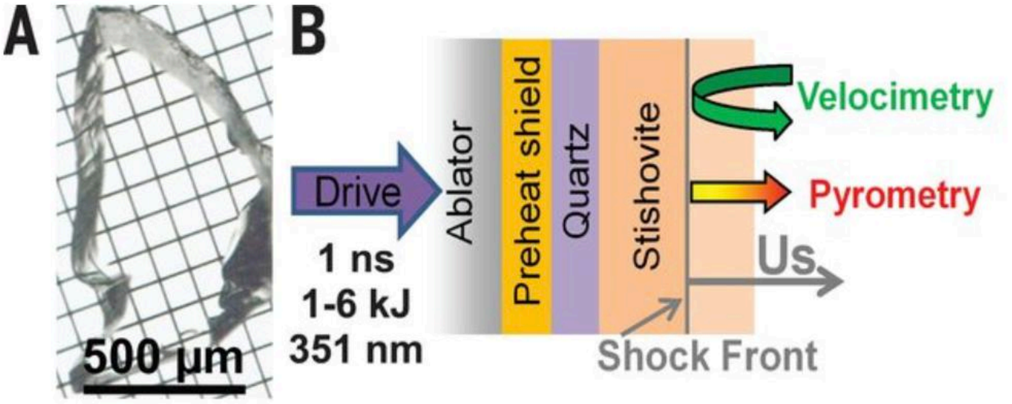

Figure 4: Laser shock compression of silicate materials; experimental concept. (A) A large stishovite crystal is synthesized at 13.5 GPA and 1800 K. (B) Intense laser pulse is focused on the ablator layer and a shock wave is sent through the planar package. From Millot et., al. (2015)

They documented the pressure-temperature equation-of-state of each of their starting materials, as well as optical properties (and hence electrical conductivity). They also derived a new experimental SiO_2 melting line, and plotted it alongside derived and extrapolated melting lines for $MgSiO_3$, MgO, and Fe, with a scale that shows the expected core-mantle boundary pressure for Earth-like large exoplanets. We can see from Fig. 5 that the derived melting line for $MgSiO_3$ that, at 20,000 K, $MgSiO_3$ is expected to be molten at core-mantle pressure boundaries for super-Earths of up to 10 $M_{\oplus}$ (roughly 1 TPa).

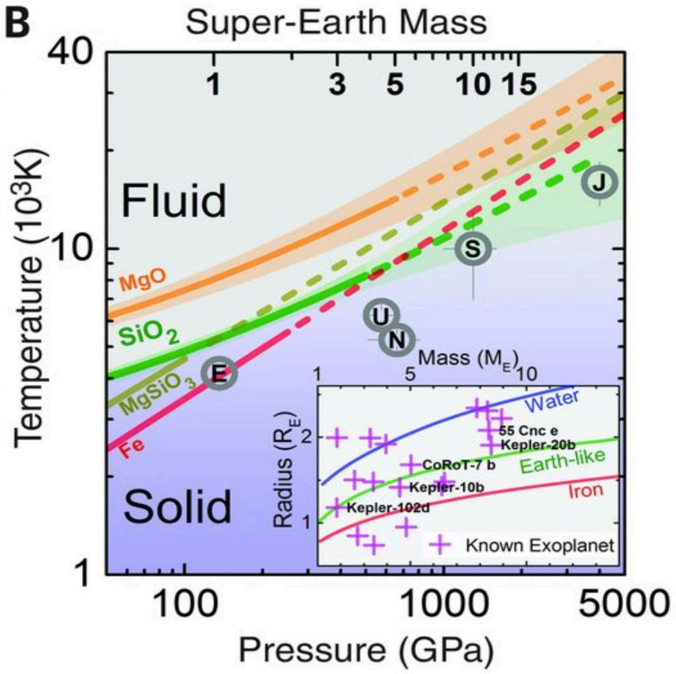

Figure 5: Taken from Millot et al., 2015 (Fig. 3b). Experimental SiO_2 melting line and core-mantle boundaries (gray circle) for Earth, Uranus, Neptune, Saturn and Jupiter (E, U, N, S, J, respectively). Melting lines of other materials ($MgSiO_3$ line from Stixrude, 2014) shown for comparison. Dashed lined indicate extrapolation. Top scale gives core-mantle boundary pressure conditions for Earth-like exoplanets as a multiple of earth's mass (e.g. 1 .. 15$M_{\oplus}$). Inset shows discovered exoplanets and the mass-radius relation for pure iron, water, or Earth-like structures that allow us to identify potentially terrestrial exoplanets.

From the perspective of probing fluid silicate behaviours within super-Earths, it thus seems reasonable to explore temperatures ranging up to 20,000 K and pressures up to several TPa, as these conditions are as equally applicable to the super-Earth temperature-pressure regime as to the super-Earth interior temperature-pressure regime. Now that we have a better idea of our constraints, we can discuss the specific materials that we wish to examine, and the properties that we might like to analyse in order to better understand the behavior of fluid silicates in extreme conditions.

2.2. Silicate Melts

For the purposes of the current thesis, we have decided to focus primarily on $MgSiO_3$. This selection has been made both because $MgSiO_3$ perovskite is the most abundant mineral phase in Earth's mantle (Murakami et al., 2007), and because the abundance of previous experimental and theoretical work on $MgSiO_3$ melt in less extreme conditions (including that produced by the current authors research group) provides an excellent reference point upon which we can extend. The main body of work is supplemented with some preliminary results from a short investigation into how the addition of water can affect a variety of material properties in these conditions. Before we discuss the background theory of first principles molecular dynamics (the computational approach used to model and investigate our chosen materials), and the specific methods employed in generating our results, we must first specify the properties of interest in the current study, and explore the related academic landscape.

Broadly speaking, the work contained in this thesis can be broken into three distinct 'groups' of results: those related to the structural, the thermodynamic, or the transport properties of a given system. Structural properties describe how the atoms in a system relate to one another. Here, we consider the radial distribution function, mean coordination number, and average bond length, throughout the body of work. The thermodynamic properties that we examine include pressure, heat capacity, and Grüneisen parameter, as well as the equation of state, which, for example, is an important factor in understanding the relative density of partial melts produced during impacts or in the extreme conditions of super-Earth interiors, and whether the melts are likely to rise or sink (Karki et al., 2006). Finally, the dynamical properties of interest include the self-diffusion coefficients of the material components, which relate to the rate of chemical reactions between liquids and their surroundings, and which can be related to viscosity and thus rate of transport. Note that this material will be covered in a primarily qualitative manner in this section; they will be given a more rigorous, quantitative treatment in the 'Methods' section below. For now, our aim is merely to provide an overview of some of the previous work that has informed the basis of this thesis. We start with the structural properties, and continuing to thermodynamic and finally, transport properties.

The radial distribution function (RDF) describes the probability of finding another atom at a distance *r* from another atom. We can use the periodicity of computed supercells (described in 'Methods') to extend the system and calculate the RDF at distances that are larger than the sizes of the simulation cells. We can also calculate the partial RDFs between specific atomic pairs (such as Si-O, Mg-O or O-O) to determine the level of short or long range order of the system. In this study, we primarily use the RDF as a diagnostic tool, in terms of gauging whether the order of the system, and contribute to confirming whether or not we are dealing with a solid or a liquid, as outlined in later sections. As such, we will not discuss the RDF in detail here, in terms of the results that we wish to compare to.

Thus, the first structural property that we will discuss is coordination number, and, in doing so, we will take the opportunity to introduce the specific paper that forms the basis for much of this thesis, in terms of replicating – and extending upon – results. Stixrude et al. (2005) performed a similar set of analyses to those performed over the course of the current work. Using first principles molecular dynamics, they analysed the structure and thermodynamic properties of $MgSiO_3$ liquid over the pressure regime of the Earth's mantle, and at temperatures ranging between 3000 K and 6000 K. With respect first to coordination number, they inspected the equilibrated liquid structure and found that compression had a substantial effect on atomic arrangement. At the reference volume (an experimental zero-pressure volume, as used in the current work, and discussed in 'Methods'), Si-O coordination is four-fold, as it is for the stable crystalline phase (pyroxene) at that pressure, minus the long-range order exhibited by the crystal.

Through the analysis of data produced via first-principles molecular dynamics (FPMD) simulations, Stixrude et al. (2005) found that Si-O coordination number changed almost linearly from 4 to 6 across the pressure range of the mantle (up to ~150 GPa - see Fig. 6) contrary to the predictions of Rigden et al., (1988), who suggested that the coordination change would take place over a narrow pressure interval. Spera et al., (2011), used empirical potential molecular dynamics (EPMD) to investigate liquid $MgSiO_3$ over temperature and pressure ranges relevant to the Earth's mantle, and found results in agreement with the FPMD results of Stixrude and Karki (2005). In the current work, we aspire to extend this analysis of mean coordination number (and coordination fraction, given the greater disorder of the molten system as opposed to crystalline) into the ultrahigh temperature and pressure regime of super-Earths and giant impacts.

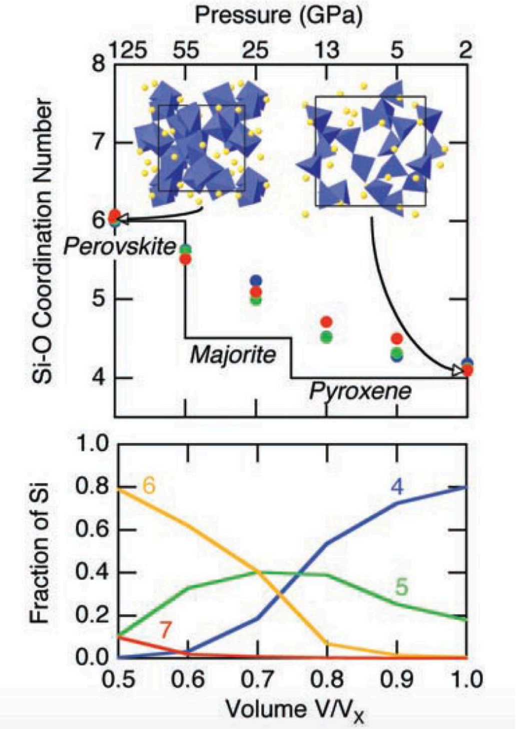

Figure 6: (Top) Mean Si-O coordination in $MgSiO_3$ liquid at 3000 K (blue), 4000 K (green), 6000 K (red), with crystalline phases shown over approximate range of stability. (Bottom) Distribution of Si-O coordination environments along the 3000 K isotherm. Snapshots from V/V_x=1.0 (right) and V/V_x=0.5 (left) are also shown, with Si-O polyhedral in blue and Mg ions in yellow. Taken from Stixrude et al., (2005).

Stixrude et al., (2005) also computed the isochoric heat capacity (C_v) and the Grüneisen parameter of the liquid directly from their simulations. They found that the isochoric heat capacity decreases by around 10% over the pressure regime of the mantle, while the Grüneisen parameter (γ) increases by roughly a factor of three over the same range, reflecting the increase in thermal pressure (see Fig. 7 & 8). This was an important result, given that all known mantle crystalline phases show a decrease in γ on compression (Stixrude & Lithgow-Bertelloni, 2005).

The authors explained that this unusual behavior was best understood from the perspective of changes in liquid structure in compression. For crystalline phases, experimental data shows that compression reduces the value of γ in each individual mineral phase, but polymorphic phase transformations have a larger and opposing effect, with the larger value of γ being shown by the higher coordinated phase. Given that the coordination number of the liquid increases on compression, the liquid adopts values of γ that are characteristic of the more highly coordinated state; this is consistent with theoretical and experimental analyses of how coordination changes on increased pressure can influence γ (Jeanloz & Roufosse, 1982; Wasserman et al., 1996; Vočadlo et al., 2003), and the theoretical results from FPMD have been repeated on several occasions since the publication of Stixrude et al., (2005)(see e.g. Karki et al., (2007) and De Koker & Stixrude (2009)).

However, what is currently unknown, is whether this approximately linear increase in γ on compression will continue into the ultrahigh temperature and pressure regimes.

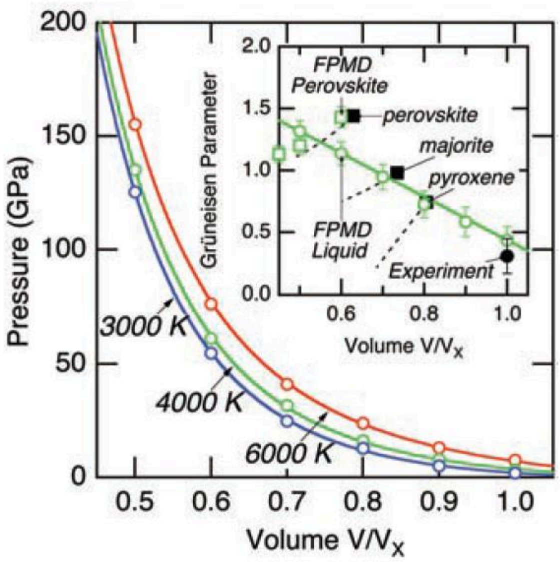

Figure 7: Mie-Grüneisen equation of state for $MgSiO_3$ liquid (lines) with FPMD results (open symbols) plotted at 3000 K, 4000 K and 6000 K (blue, green and red, respectively). (Inset) Grüneisen parameter of the liquid (open circles) and perovskite (open squares) from FPMD simulations, with experimental value for the liquid at ambient melting point. γ for the solidus crystalline phases at ambient conditions (filled squares) and under compression (dotted lines) also shown. From Stixrude et al., (2005).

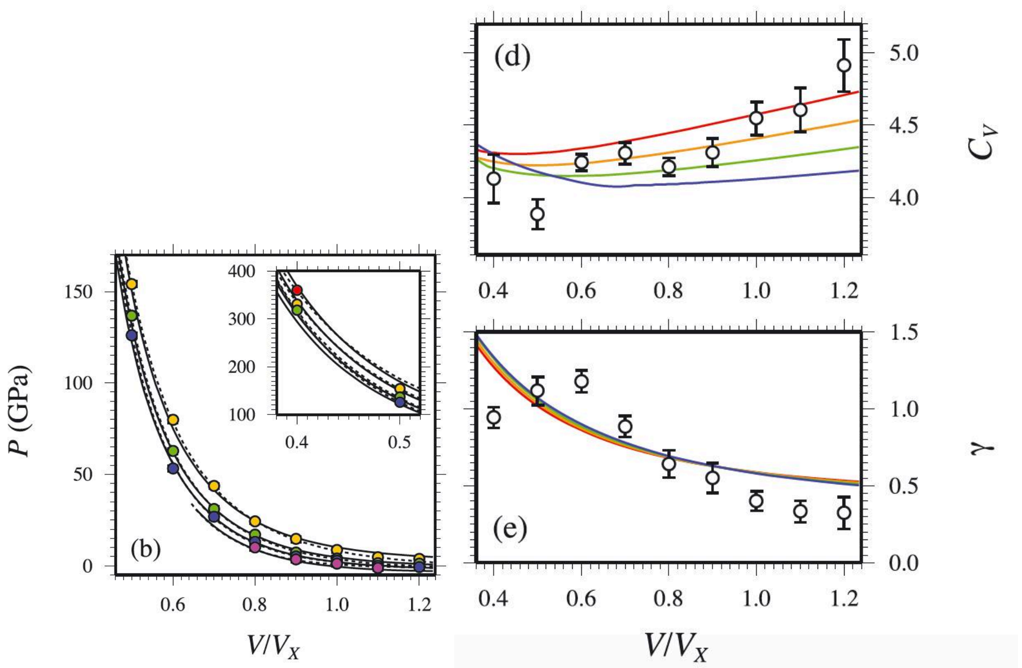

Figure 8: (b) Equation of State for $MgSiO_3$ liquid, where purple circles are at 2000 K, blue is 3000 K, green is 4000 K, yellow is 6000 K and red is 8000 K. (d) is isochoric heat capacity and (e) is Grüneisen parameter, where in each case the white circles are average values from Stixrude and Karki (2005), except at the V/Vx=0.4 volumes, and the 2000 K cases.

In the current work, we also consider both the mean squared displacements and the self-diffusion coefficients. This allows us to gain some insight into the rate of mass transfer, and ultimately, the time taken for a system to reach thermodynamic equilibrium. In this work, we don't explicitly examine chemical diffusion – defined broadly as both local and directional mass transfer in response to chemical potential differences. Instead, we consider the measure of the random walk of a material's constituents in the absence of chemical gradients – i.e. self-diffusion.

In previous FPMD work across the temperature-pressure range of Earth's mantle, self-diffusivities of Mg, Si and O in $MgSiO_3$ and Mg_2SiO_4 liquid, have shown a pressure and temperature dependence that fits very well to an Arrhenian form, and the fit parameters are found to be independent of temperature over this range (Lacks et al., 2007; De Koker et al., 2007; Nevins et al., 2009). According to the FPMD simulations of Karki & Stixrude (2010), the overall viscosity of $MgSiO_3$ liquid increases with temperature and pressure, with a 10-fold increase along model geotherms, from the surface to the base of the mantle. On the introduction of water to this temperature-pressure environment, viscosity is systematically lowered, thus increasing mean self-diffusion. Will this remain true for the ultrahigh temperature and pressure regimes of interest in this work?

These FPMD findings are corroborated by Adjaoud et al. (2011), who performed large-scale classical molecular dynamics simulations (2016 ions, 288 formula units) on self-diffusivity and viscosity in Mg_2SiO_4 melt. They found that a closed Arrhenius expression was readily fitted to both transport properties over the temperature and pressure regime explored (up to 32 GPa and between 2600 and 3200 K), however, it's worth noting that this range is much smaller than the range that we aim to explore in the current work.

Meanwhile, exploring the affect from volatile addition, the FPMD simulations of Ghosh & Karki, (2017), demonstrated that dissolved CO_2 – thought to be the second most abundant volatile in silicate melts on Earth - also systematically enhanced the diffusivity of the constituent elements of $MgSiO_3$, and the electrical conductivity, lowering viscosity by a factor of 1.5 – 3 over the pressure range of Earth's mantle.

In the case of hydrated $MgSiO_3$, some interesting research possibilities arise from tracking the diffusivity of hydrogen. For example, in extreme conditions, we might feasibly ask whether or not hydrogen is ionic, and thus, what the strength of any proton conductivity might be, in relation to the electrical conductivity of the system. It has been suggested that spontaneous, impact-generated magnetic fields might be behind the anomalously high thermal magnetic remanence observed in the early-Lunar impact melt returned from Apollo 17 (Sugiura, 1979) as well as a variety of more broad-scale magnetic anomalies (Crawford & Schultz, 1988; Oran et al., 2015)). How might this process have been affected for impacts on planets with water, and thus hydrogen?

These are, of course, arguably even more important considerations with respect to magnetic field generation in the interior of super-Earths, with the well-documented link between the survival of complex life on Earth, and its level of shielding from high energy solar and cosmic particles.

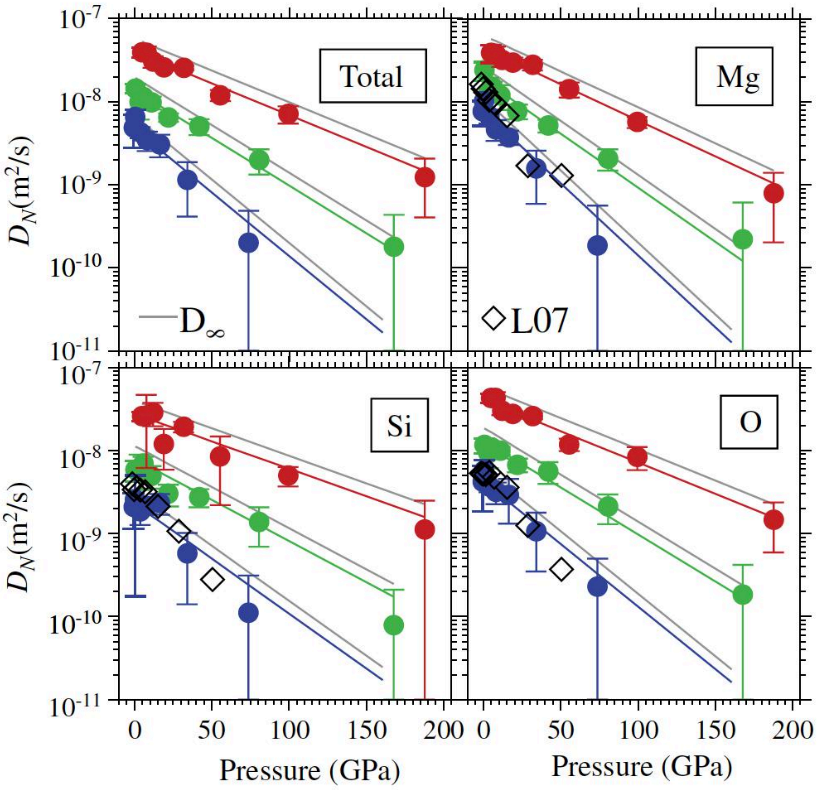

Figure 9: Self-diffusion of Mg_2SiO_4 liquid over the temperature-pressure range of Earth's mantle at 3000 K, 4000 K and 6000 K (blue, green, red, respectively), fit with an Arrhenius relation. Open diamonds show empirical potential calculations from Lacks et al., (2007). Taken from De Koker et al., (2008).

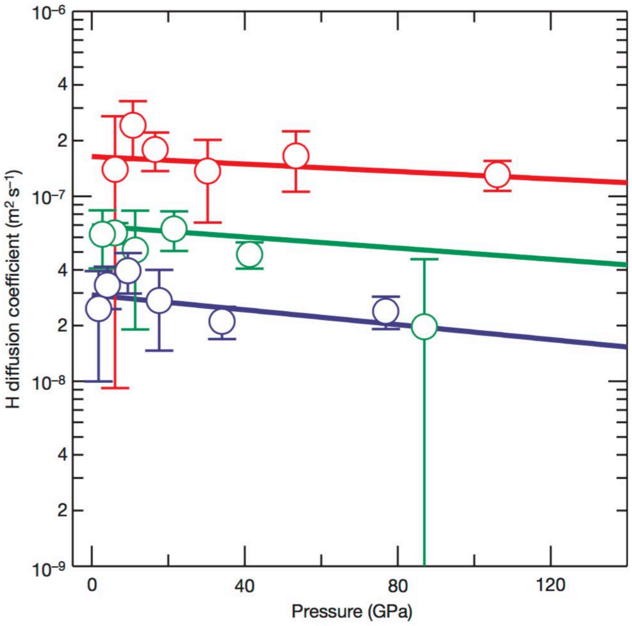

Figure 10: Self-diffusion of hydrogen in hydrated MgSiO3 liquid at 3000 K, where blue is 3000 K, green is 4000 K and red is 6000 K. Fitting performed via the Arrhenius relation. The value of diffusivity agrees well with that extrapolated to 3000 K from lower temperature, low pressure experiments on basaltic melt (Mookherjee et al., 2008) indicating that proton diffusivity is not strongly dependent on the composition of the melt.

$\rho(g/cm^3)$	$P(GPa)$	$D_O\ 10^{10} m^2/s$	$D_{Si}\ 10^{10} m^2/s$	$D_{Mg}\ 10^{10} m^2/s$
2.198	−1.09	23.1	15.5	114
2.3624	−0.32	25.4	19.8	108
2.6012	1.54	30.9	20.7	105
2.7967	3.67	34.7	25.6	99.9
2.9943	6.39	35.4	24.4	79.9
3.401	14.3	26.2	17.7	47.7
3.7982	26.9	12	7.66	24.2
4.1939	46.8	2.53	1.76	7.31

Table 2: Property data for MgSiO3 melt at 3000 K, from Lacks et al., (2007), including density, pressure, and diffusivity of the three atomic components

3. THEORY

The extreme conditions of temperature and pressure that are relevant to giant impact events – and to the interiors of Super Earth exoplanets – are largely inaccessible by experimental studies. However, direct experimental studies are only one way of investigating the properties of matter in a variety of conditions. Another method relies on the observation that many physical phenomena can be explained and predicted by analysing the behaviour of electrons as they interact with each other, with atomic nuclei, electromagnetic fields and other fundamental forces. Indeed, it is possible to quantitatively predict certain properties of materials in a given set of conditions, using quantum mechanical principals, the periodic table, and computational techniques.

The most commonly used method of achieving this – and that which is used in the current work - is to perform first principles molecular dynamics (FPMD) using density functional theory (DFT). In this chapter, we discuss the general background theory to this approach - including some basic electronic structure theory - and leading up to an overview of the development of DFT.

3.1 FUNDAMENTALS

In the current work, our primary objective is to understand the properties of common Earth materials ($MgSiO_3$ and select volatiles), by examining the behaviour of the same materials at the atomic scale. In approaching this problem, it is useful to recall that these materials are best conceptualised – in the first instance - as a collection of electrons and nuclei that are held together with a balance of attractive and repulsive forces governed by the Coloumb interaction.

It is instructive to observe how the kinetic energy of the electrons and nuclei, and the repulsive/attractive forces between electrons-electrons, nuclei-nuclei, and electrons-nuclei, all interact in atomic units as follows:

$$\hat{H} = -\frac{1}{2}\sum_i \nabla_i^2 + \sum_{i,I}\frac{Z_I}{|r_i - R_I|} + \frac{1}{2}\sum_{i\neq j}\frac{1}{|r_i - r_j|} - \sum_I \frac{1}{2M_I}\nabla_I^2 + \frac{1}{2}\sum_{I\neq J}\frac{Z_I Z_J}{|R_I - R_J|}, \qquad [4]$$

where $\hat{H}$ is the many-body Hamiltonian operator, summations over *i* and *j* represent the electrons of the system, and summations over *I* and *J* represent the nuclei. The kinetic energy terms are represented by the spatial differential operator ∇ and M_I is the mass of the I^{th} nucleus, Z_I the atomic number, and the positions of the electrons and nuclei are denoted by the three-dimensional vectors r_i and R_I, respectively.

We now introduce the wavefunction $\Psi(\boldsymbol{r^N},t)$, where *t* is time and $\boldsymbol{r^N}$ represents the positions of all the electrons in the system. The square of the wavefunction represents the probability density of electrons. Incorporating this probability density function brings us to the many-body Schrödinger equation; one of the core relations of quantum mechanics, and one that gives us almost everything we need to know to study the behavior of materials.

$$\left[-\sum_{i}\frac{\nabla_i^2}{2}-\sum_{I}\frac{\nabla_I^2}{2M_I}-\sum_{i,I}\frac{Z_I}{|r_i-R_I|}+\frac{1}{2}\sum_{i\neq j}\frac{1}{|r_i-r_j|}+\frac{1}{2}\sum_{I\neq J}\frac{Z_IZ_J}{|R_I-R_J|}+\right]\Psi=E_{tot}\Psi \qquad [5]$$

When materials are modelled using first principles methods, it is this version of the time-independent many-body Schrödinger equation that is most often used, clearly showing that only atomic numbers and masses are required as external parameters (Schrödinger, 1926).

However, in order to begin the process of solving the many-body Schrödinger equation for a system of interest, some simplifications are necessary. Equation [5] is not only very general, it also become extremely complex to solve in the case of many-electron systems, owing to the need to process solutions for 3N Cartesian coordinates in the many-body wavefunction $\Psi(\boldsymbol{r}_1,\boldsymbol{r}_2,\ldots,\boldsymbol{r_N})$. For example, Giustino (2014) demonstrated that obtaining a full quantum description of a unit cell of silicon in the diamond structure would mean performing a huge number of matrix operations, with the complexity of the solution scaling exponentially with system size.

The following few subsections will deal with the topic of simplifying equation [5] to allow us to solve it in a more practical manner; such is the aim of *ab initio* methods.

3.2 BORN OPPENHEIMER APPROXIMATION

One such simplification is known as the Born-Oppenheimer Approximation (Born & Oppenheimer, 1927), which effectively enables us to separate the electron-nuclei interaction term in equation [5]. In this approach, we assume that the degrees of freedom for both the electrons and the nuclei can be treated separately. This is justified via the observation that electrons are many orders of magnitude less massive than nuclei, but experience similar forces. Given the mass disparity, it can be seen that electrons will respond almost instantaneously to an applied force, whereas the nuclei may be considered as effectively stationary relative to the electron. We can further assume that, although the spatial configuration of the nuclei may change, the relative agility of the electrons will allow them to rapidly respond and adjust to these changes.

As such, in the Born-Oppenheimer Approximation, the nuclei in the system are fixed to some spatial configuration R_0, allowing for the effective parameterization of the equation [5], and simplifying our system to a sea of moving electrons interacting with each other, and with the stationary nuclei. Given the fixed position of the nuclei, the potential energy between them – described by the Coloumb repulsion – becomes constant, and we thus adopt the time-independent Schrödinger equation [Eq. 5]. To emphasize these points, we rewrite equation [5] as:

$$\left[-\sum_i \frac{\nabla_i^2}{2} + \sum_i V_{ext}(\boldsymbol{r_i}) + \frac{1}{2}\sum_{i \neq j} \frac{1}{|r_i - r_j|}\right]\Psi = E\Psi \qquad [6]$$

where $V_{ext}(\boldsymbol{r})$ is defined as the external Coulomb potential of the nuclei as experienced by the electrons, given by:

$$V_{ext}(\boldsymbol{r}) = -\sum_I \frac{Z_I}{|r - R_I|} \qquad [7]$$

We can thus define the many-electron Hamiltonian as:

$$\hat{H}(\boldsymbol{r}_1 \ldots \boldsymbol{r}_N) = \left[-\sum_i \frac{\nabla_i^2}{2} + \sum_i V_{ext}(\boldsymbol{r_i}) + \frac{1}{2}\sum_{i \neq j} \frac{1}{|r_i - r_j|}\right] \qquad [8]$$

Allowing us to simplify equation [5] as $\hat{H}\Psi = \mathrm{E}\Psi$, or, in a new, parameterized version as follows:

$$\hat{H} = \hat{T}_e(\boldsymbol{r}) + \hat{V}_{eN}(\boldsymbol{r}; \boldsymbol{R_0}) + \hat{V}_{ee}(\boldsymbol{r}) + E_{NN} \qquad [9]$$

where the various kinetic $\hat{T}$ and potential $\hat{V}$ operators refer to electrons e and nuclei N at positions $\boldsymbol{r}$ and $\boldsymbol{R}$, respectively, and E_{NN} is the constant potential energy from fixed nuclei interactions. It should be noted that we can consider the term $\hat{T}_e(\boldsymbol{r}) + \hat{V}_{eN}(\boldsymbol{r};\boldsymbol{R_0}) + \hat{V}_{ee}(\boldsymbol{r})$ as equal to the electronic Hamiltonian, $\hat{H}_e$.

Further to this, if we examine equation [5], we can see that, via the summative nature of the equation, it is reasonable to define a single-electron Hamiltonian as:

$$\hat{H}_0(\boldsymbol{r}) = -\frac{1}{2}\nabla^2 + V_{ext}(\boldsymbol{r}) \qquad [10]$$

and thus split the many-electron Hamiltonian up according to:

$$\hat{H}(\boldsymbol{r}_1 \ldots \boldsymbol{r}_N) = \sum_i \hat{H}_0(\boldsymbol{r_i}) + \frac{1}{2}\sum_{i\neq j}\frac{1}{|r_i - r_j|} \qquad [11]$$

Equation [9] demonstrates how a system of *N* electrons will behave in the presence of fixed atomic nuclei, as described by their spatial coordinates $\{r_i\}$. However, it does not include their spin state, an intrinsic angular momentum property that is necessary to include for a fuller description. In order to do so, we must include a fourth degree of freedom in addition to the three spatial degrees of freedom, as represented by the spin coordinate ω. This addition does not directly affect equation [9], given that the electronic Hamiltonian is not spin-dependent. However, it does lead us to one of the more famous quantum mechanical principles; the Pauli Exclusion Principle.

The Pauli Exclusion Principle states that fermions (such as electrons and nucleons) will cause the many-body wavefunction, Ψ, to change sign if they exchange variables (position, spin) with a like fermion. In other words, no two electrons can occupy the same quantum state in the same position in space. We can enforce the principal by constructing a wavefunction that is anti-symmetric, e.g. $f(x,y) = -f(y,x)$, meaning that an interchange of any two electrons in the system obeys: $\Psi(x_1 \ldots x_N) = -\Psi(x_1 \ldots x_N)$.

The many-body wavefunction (equation [5]) can be considered in terms of it being a probability amplitude; that is to say, the wavefunction describes the probability of finding an electron at a given position in space. To illustrate this concept, the wavefunction is typically normalized, e.g.

$$\int |\Psi(\boldsymbol{r}_1, \dots \boldsymbol{r}_N)|^2 d\boldsymbol{r}_1 \dots d\boldsymbol{r}_N = 1 \qquad [12]$$

where equation [12] describes a system of N electrons existing with a probability of 1. However, actually determining this ground state wavefunction – and thus, more usefully, the total energy of the system - for a system of N electrons is only really tractable for systems with very few electrons. In this section, we discuss how the many-body wavefunction can be broken into a series of single-particle wavefunctions, and how these single-particle wavefunctions can be combined to find the total energy of a many-electron system, without having to deal with exponential increases in the number of electron configurations that must be calculated to determine a ground state wavefunction from equation [5].

3.3 HARTREE-FOCK THEORY

When the Born-Oppenheimer approximation is applied to the time-independent Schrödinger equation, the result is the electronic Schrödinger equation, which we can state using the compact notation of equation [13] as:

$$\left[\hat{T}_e(\boldsymbol{r}) + \hat{V}_{eN}(\boldsymbol{r};\boldsymbol{R}) + \hat{V}_{NN}(\boldsymbol{R}) + \hat{V}_{ee}(\boldsymbol{r})\right]\Psi(\boldsymbol{r};\boldsymbol{R}) = E\Psi\,(\boldsymbol{r};\boldsymbol{R}) \qquad [13]$$

Solving the electronic Schrödinger equation also allows us to gain access to the electronic wavefunction, and with it a whole host of molecular properties.

Hartree-Fock theory allows us to move closer to solving the Schrödinger equation for a many-body system by making further assumptions about the interaction strength between electrons, and looking for solutions in the form of a Slater determinant.

The anti-symmetry principle - as a consequence of the Pauli Exclusion principle - can be satisfied for a two-electron system for any given orbital by the wavefunction:

$$\Psi(\boldsymbol{r_1}, \boldsymbol{r}_2) = \frac{1}{\sqrt{2}}[\phi_1(\boldsymbol{r}_1)\phi_2(\boldsymbol{r}_2) - \phi_1(\boldsymbol{r}_2)\phi_2(\boldsymbol{r}_1) \qquad [14]$$

or

$$\Psi(\boldsymbol{r_1},\boldsymbol{r}_2)=\frac{1}{\sqrt{2}}\begin{bmatrix}\phi_1(\boldsymbol{r}_1) & \phi_2(\boldsymbol{r}_1)\\ \phi_1(\boldsymbol{r}_2) & \phi_2(\boldsymbol{r}_2)\end{bmatrix} \qquad [15]$$

Which is known as a Slater determinant. This functional form – in opposition to a classical mean field approximation - coincides well with quantum mechanical principles, given that it allows for every electron to be associated with every orbital, and thus for electrons to remain indistinguishable, while obeying antisymmetry.

But how do we find the single-particle wavefunctions required by equation [15]? Consider the lowest energy quantum state Ψ, the energy, E, of which we may obtain by multiplying both sides of $\widehat{H}\Psi = \mathrm{E}\Psi$ by Ψ^* and integrating. This leads us to:

$$E=\int d\boldsymbol{r}_1 \dots d\boldsymbol{r}_N \;\; \Psi^{*}\widehat{H}\;\Psi \qquad [16]$$

Or, using Dirac’s bra-ket notation:

$$E=\langle\Psi|\widehat{H}|\Psi\rangle \qquad [17]$$

The Hartree-Fock equations (Fock, 1930b) are then obtained by minimizing E with respect to variations in the single-particle wavefunctions, with the requirement that:

$$\frac{\delta E}{\delta\phi_i^*}=0 \qquad [18]$$

and:

$$\int d\boldsymbol{r}\phi_i^*(\boldsymbol{r})\phi_j(\boldsymbol{r})=\delta_{ij} \qquad [19]$$

are orthonormal, where δ_{ij} is the Kronecker delta which is equal to 1 if $i=j$ or 0 when $i\neq j$. As we will see, the Hartree-Fock equations are distinguished from classical mean-field approximations by the appearance of what’s known as the

Fock exchange potential, $V_X(\boldsymbol{r},\boldsymbol{r}')$, which arises as a consequence of the Pauli Exclusion Principal, which forbids two electrons from occupying the same quantum state, and which is given as:

$$V_X(\boldsymbol{r},\boldsymbol{r}') = -\sum_j \frac{\phi_j^*(\boldsymbol{r}')\phi_j(\boldsymbol{r}')}{|\boldsymbol{r}-\boldsymbol{r}'|} \qquad [20]$$

The derivation of the Hartree-Fock equations involves a lengthy process. As this level of detail is not the primary focus of this thesis, we will merely state the equations below:

$$\left[-\frac{\nabla^2}{2} + V_{ext}(\boldsymbol{r}) + V_H(\boldsymbol{r})\right]\phi_i(\boldsymbol{r}) + \int d\boldsymbol{r}'\, V_x(\boldsymbol{r},\boldsymbol{r}')\phi_i(\boldsymbol{r}') = \varepsilon_i\phi_i(\boldsymbol{r}), \qquad [21]$$

$$n(\boldsymbol{r}) = \sum_i |\phi_i(\boldsymbol{r})|^2, \qquad [22]$$

$$\nabla^2 V_H(\boldsymbol{r}) = -4\pi n(\boldsymbol{r}) \qquad [23]$$

Where $n(\boldsymbol{r})$ is the distribution of electronic charge – also known as the electron density - generated according to Poisson's equation, and $V_H(\boldsymbol{r})$ is the potential energy of the electrons within the generated electrostatic charge, known as the Hartree potential.

While the addition of this non-local Fock potential makes progress toward the introduction of quantum electrons in solving the many-body Schrödinger equation, the Hartree-Fock equations are also quite tricky to evaluate in a practical way, owing to the need to integrate over the additional variable $\boldsymbol{r}'$ during their solution. In the next section, we discuss DFT more directly, including how we might replace the exchange potential V_X with a more practical local exchange potential.

3.4 DENSITY FUNCTIONAL THEORY

Density Functional Theory supposes that, instead of considering the ground state electronic wavefunction as the fundamental variable in our equations, we instead turn to a calculation of the ground state electron density. It turns out that this allows us to treat the many-body Schrödinger equation as a numerically solvable one-electron equation, and effectively to go from having a 3N degrees of freedom to calculate over, down to 3 degrees of freedom for an N-electron system. Although DFT is unable to handle excited states, it does provide a theoretically precise description of the ground state of the system, which yields many useful properties. Nonetheless, and as we shall see, it requires that we use an approximation of the so-called exchange-correlation functional, many of which exist and vary in levels of sophistication and computational cost.

3.4.1 HOHENBERG-KOHN

We can obtain the total energy, E, of a many-electron system according to equations [11] and [12], while the associated many-electron Hamiltonian is given by equation [5]. Given that the Hamiltonian's structure is independent of the specific material in question (Giustino, 2014), changes in the total energy of the system must be linked to changes in the many-body wavefunction, and thus that:

$$E = \mathcal{F}[\Psi] \qquad [24]$$

In 1964, Hohenberg and Kohn demonstrated that the groundstate energy of the system is a functional only of the electron density $n(\boldsymbol{r})$ $(\text{Hohenberg and Kohn, } 1964)$, rather than being a functional of the wavefunction as a whole, as is the case with any excited state. This observation is derived from the first of their two theorems:

Theorem 1: *The external potential V_{ext} acting on a system of electrons is uniquely determined – with the exception of a constant - by the ground state electron density $n_0(\boldsymbol{r})$*

If true, we can see how the we can obtain the Hamiltonian operator from the external potential and total number of electrons, and thus the wavefunctions of all states in the many-body system, leading to an elucidation of material properties.

Theorem 2: *A universal functional of the energy in terms of the density* $E[n(\boldsymbol{r})]$ *can be found variationally; the trial density that succeeds in minimizing the total energy is also the groundstate density.*

To elaborate, an energy functional given in terms of the density $n(\boldsymbol{r})$ can be defined according to an external potential. The global minimum of the energy functional, is the ground state energy of the system, and the density that minimized the functional, is the groundstate density. In other words, $n(\boldsymbol{r})$ determines $V_{ext}(\boldsymbol{r})$, while N and $V_{ext}(\boldsymbol{r})$ determine $\widehat{H}$ and thus Ψ, ergo: $E = F[n]$.

However, Hohenberg and Kohn's seminal work is only applicable for non-degenerate, zero temperature many-body systems. Later work by Mermin (Mermin, 1965), Levy (Levy, 1979) and Lieb (Lieb, 1983)(Jones and Gunnarsson, 1989), was able to extend the work to include nonzero temperatures, and degenerate goundstates.

3.4.2 – Kohn-Sham theory

While the Hohenberg-Kohn theorem developed in 1964 demonstrates that the total groundstate energy of the electrons in the system is a functional of the electron density, it does not tell us anything regarding how we might go about constructing such a functional. Indeed, the exact form of the functional remains unknown to this day.

Various approximations and approaches have been put forward since, including the Thomas-Fermi approach (as detailed in (Jones and Gunnarsson, 1989)), which suffered from the problem of requiring the kinetic energy term – a considerable contribution to the total energy of the system – to be approximated.

Kohn and Sham (Kohn and Sham, 1965) approach the issue by assuming that the many-body Hamiltonian – in which the electrons fully interact - can be replaced by a similar 'auxiliary Hamiltonian' in which the electrons do not interact, but which nonetheless leads to the same solution, such that the groundstate density is the same as that of a system of interacting electrons. Crucially, the Kohn-Sham approach leads to a Hamiltonian that preserves the original kinetic energy operator $\widehat{T} = -\frac{1}{2}\nabla$ but replaces the original potential with an effective *ficticious* potential, and stipulates that a given electron at a given point in space will effectively interact with only its nearest neighbors.

In practical terms, Kohn and Sham derived a functional that separately pieced together external potential terms, kinetic terms and Hartree energy terms, plus an extra term known as the *exchange and correlation* energy:

$$E = F[n] = \hat{T}_0[n] + \int n(\boldsymbol{r}) \left[\hat{V}_{ext}(\boldsymbol{r}) + \frac{1}{2} \hat{V}_H(\boldsymbol{r}) \right] dr + E_{XC}[n] \qquad [25]$$

where $\hat{T}_0$ is the kinetic energy of the system with electron density n within which the electrons do not interact with one another and $\hat{V}_H$ is the Hartree potential (the classical electronic Coulomb potential). The extra term, $E_{XC}[n]$ incorporates the exchange and correlation energy, and fundamentally serves to relate a system of non-interacting electrons with an equivalent interacting system. In general, we can think of the exchange energy as the energy released when two electrons are exchanged symmetrically or unsymmetrically (changing sign), while the correlation energy can be thought of as the energy associated with an electron's influence on the other electrons in the system. More specifically, E_{XC} in the current context, is the sum of the errors made from treating the electron-electron interaction as if they are non-interacting particles, or, more formally:

$$E_{XC}[n] = T[n] - T_0[n] + U_{XC}[n] \qquad [26]$$

Where $T[n] - T_0[n]$ is the kinectic energy difference between the interacting and non-interacting systems, and $U_{XC}[n]$ is the Coulomb interaction between electrons and the exchange-correlation hole (the space around an electron where electron correlation effects - due to instantaneous Coulomb repulsion - reduce the probability of finding another electron to almost zero).

It is pertinent to observe that being able to calculate the exchange and correlation energy would enable us to calculate the total groundstate energy of the system $E = F[n]$ via the electron density. In the previous section, we saw how the groundstate electron density is the function that minimizes the total energy. This is known as the Hohenberg-Kohn variational principle, and is given by:

$$\left. \frac{\delta F[n]}{\delta n} \right|_{n_0} = 0 \qquad [27]$$

If the derivative of the above functional must be equal to zero, as stated by the principle, then we can create an equation for the single-particle wavefunctions $\phi_i(\boldsymbol{r})$ which may be used in constructing the electron density, e.g:

$$n(\boldsymbol{r}) = \sum_i [\phi_i(\boldsymbol{r})]^2 \qquad [28]$$

The steps required to go from equation [28] to the one that follows will not be elaborated here, however, if we require the wavefunctions $\phi_i(\boldsymbol{r})$ to also be orthonormal, then the Hohenberg-Kohn variational principle gives us the following:

$$\left[-\frac{1}{2}\nabla^2 + V_n(\boldsymbol{r}) + V_H(\boldsymbol{r}) + V_{XC}(\boldsymbol{r})\right]\phi_i(\boldsymbol{r}) = \varepsilon_i\phi_i(\boldsymbol{r}) \qquad [29]$$

where ε_i is an eigenvalue of the wavefunction and $V_{XC}(\boldsymbol{r})$ is the exchange and correlation potential, as given by:

$$V_{XC}(\boldsymbol{r}) = \left.\frac{\delta E_{XC}[n]}{\delta n}\right|_{n(\boldsymbol{r})} \qquad [30]$$

This brings us back to the idea that there must be some functional $E_{XC}[n]$ that can give us the exact groundstate energy and allow us access to all many-body effects, and that the functional used is sufficiently inexpensive and accurate for a given purpose. And so, we proceed to consider some of the methods through which we might construct the functional, focusing on two of the most popular and relevant to the current thesis: the Local Density Approximation and the Generalised Gradient Approximation.

3.4.3. Local Density Approximation

The task of approximating E_{XC} has spawned a vast and active field of researchers, with different groups producing different ‘flavours’ of functional, the eventual usefulness of which is typically measured by agreement with experiment, where possible. The most standardized version of this approximated functional is known as the Local (spin-) Density Approximation (LDA), first introduced by Kohn and Sham (Kohn and Sham, 1965) (Jones and Gunnarsson, 1989).

The LDA approach was based on a homogenous, free-electron gas system, wherein the charge density is constant, as a result of a constant external potential, and the potential of the nuclei also remains constant. This system can be specified by the value of the constant electron density $\rho = N/V$. However, in addition to the free electron gas model, we also consider the electron-electron Coulomb interaction. It is possible to obtain the exchange energy directly, but the correlation energy must be calculated using numerical techniques.

When we apply this approach to materials other than a homogenous electron gas, we can nonetheless apply it to understanding exchange and correlation in discretized regions where the density varies slowly. Consider electron density over position in a molecular system, plotted along a given direction. This system may be partitioned into an arbitrary number of rectangular regions, which may then be decreased in width until they are infinitesimally small volume elements. We can then associate each of these volume elements, $d\boldsymbol{r}$, with a homogenous electron gas of local density $n(\boldsymbol{r})$ at a particular point $\boldsymbol{r}$. Each of these elements will contribute an exchange-correlation energy according to:

$$dE_{XC} = \frac{E_{XC}^{HEG}[n(\boldsymbol{r})]}{V} d\boldsymbol{r} \qquad [31]$$

where HEG is homogenous electron gas and $E_{XC}^{HEG}[n(\boldsymbol{r})]$ is obtained adding the exchange and correlation energies. This equation defines the local density approximation.

The exchange energy of the electron gas, E_x, is given by the simple analytical equation (given in Hartree units) below:

$$E_x = -\frac{3}{4}\left(\frac{3}{\pi}\right)^{\frac{1}{3}} n^{\frac{4}{3}} V \qquad [32]$$

and the exchange energy of the entire system is therefore:

$$E_x = -\frac{3}{4}\left(\frac{3}{\pi}\right)^{\frac{1}{3}} n^{\frac{4}{3}} V \int_V n^{\frac{4}{3}}(\boldsymbol{r}) d\boldsymbol{r} \qquad [33]$$

We do not have such a simple solution for the correlation energy, but stochastic numerical methods have been used to approximate it in a reasonable way, e.g. via Quantum Monte Carlo (Ceperley and Alder, 1980). The data collected by Ceperley and Alder has been used to obtain the correlation energy of the electron gas by removing known kinetic, exchange and Hartree potentials from the total energies, and the work has since been parameterized by Perdew and Zunger (1981), obtaining:

$$E_C = nV.\begin{cases} 0.0311\ln r_s - 0.0480 + 0.002 r_s \ln r_s - 0.0116 r_s & if\ r_s < 1 \\ \dfrac{-0.1423}{1 + 1.0529\sqrt{r_s} + 0.3334 r_s} & if\ r_s \geq 1 \end{cases} \qquad [34]$$

where r_s is the Wigner-Seitz radius, defined as the average spherical radius occupied by each electron.

Finally, and as previously mentioned, given the availability of a practical solution for obtaining the exchange and correlation energy, we can obtain the exchange and correlation potential $V_{XC}(\boldsymbol{r})$ via the functional derivative in equation [30], and thus solve the Kohn-Sham equations. Calculating the exchange potential is fairly straight forward - the result of the functional derivative gives us an expression that permits calculation of the exchange potential at point $\boldsymbol{r}$ via the local density at the same point $n(\boldsymbol{r})$.

$$V_x(\boldsymbol{r}) = -\left(\frac{3}{\pi}\right)^{\frac{1}{3}} n^{\frac{1}{3}}(\boldsymbol{r}) \qquad [35]$$

The expression for obtaining the correlation potential at point $\boldsymbol{r}$ is more complex; however, it nonetheless is also determined by the equivalent density (Giustino, 2014).

LDA has been very widely used by materials researchers since its inception, and is considered excellent for obtaining properties such as structure, vibrational properties, and elastic properties for a great many systems. However, since it approximates the energy of the actual density via the energy of the local density, it runs into issues in scenarios where the density changes rapidly, such as in molecular systems. In these scenarios, LDA tends to be less accurate when used to obtain dynamical properties such as chemical reaction energetics, e.g. calculating activation energy barriers, and binding energies (typically overestimated by 20-30%)(Harrison, 2003). For these more elaborate, involved properties, we require more elaborate and involved ways of approximating E_{XC}.

3.4.4. Generalised Gradient Approximation

The LDA gives us a fully-local way to approximate E_{XC}. However, as we've seen, it is known to have potential accuracy issues in certain situations, such as when the density of a given system undergoes rapid changes, and thus cannot easily be approximated via local density calculations.

The Generalised Gradient Approximation (GGA) approach to approximating E_{XC} depends on the density, as with LDA, but also defines a factor – known as the enhancement factor F_{XC} - that takes into account the gradient of the density $|\nabla n(\boldsymbol{r})|$, and thus the non-homogenous nature of the true electron density:

$$E_{XC}^{GGA}[n(\boldsymbol{r})] = \int n(\boldsymbol{r})\, \varepsilon_{XC}^{HEG}[n(\boldsymbol{r})] F_{XC}[n(\boldsymbol{r}), \nabla n(\boldsymbol{r})\,] d\boldsymbol{r} \tag{36}$$

where F_{XC} is typically defined in terms of the Wigner-Seitz radius, r_s, and the reduced density gradient, given as:

$$s(r) = \frac{|\nabla n(\boldsymbol{r})|,}{2k_F(\boldsymbol{r})n(\boldsymbol{r})} \tag{37}$$

where k_F is the Fermi-wavevector (Perdew et al., 1996). The GGA is not a unique function, thus a whole 'family' of different GGA functionals have been created by plotting $F_{XC}(r_s, s)$ against s for a range of r_s values, and examining and comparing the results. The end result has been a considerable reduction in the overestimate of the overbinding error seen with LDA in the case of solids and molecules (Harrison, 2003).

3.4.5. Basis Sets

Basis sets provide us with a practical, mathematical method for representing molecular orbitals in DFT calculations. We can represent the wavefunction $\phi_i(\boldsymbol{r})$ as a linear expansion of basis functions in a unit cell. Bloch's theorem states that if nuclei in a system are arranged periodically (as they are in all of our calculations), then the potential acting on the electrons must also be periodic. In other words:

$$V(\boldsymbol{r} + \boldsymbol{L}) = V(\boldsymbol{r}) \tag{38}$$

where L is a given lattice vector. If the potential is periodic, then so must be the density $n(\boldsymbol{r})$ and, by extension, the magnitude of the wavefunction, such that $n(\boldsymbol{r}) = |\phi(\boldsymbol{r})|^2$. The possible wavefunctions are all thus quasi-periodic:

$$\phi(\boldsymbol{r}) = e^{i\mathbf{k}\cdot\boldsymbol{r}} u_k(\boldsymbol{r}) \qquad [39]$$

where u_k is a periodic function ($u_k(\boldsymbol{r}+\boldsymbol{L}) = u_k(\boldsymbol{r})$) and $e^{\mathrm{ik}\cdot\boldsymbol{r}}$is an arbitrary phase factor, with k representing a wave-vector confined to the first Brillouin zone (the primitive unit cell defined in reciprocal space). Thus:

$$\phi_k(\boldsymbol{r}+\boldsymbol{L}) = e^{i\mathbf{k}\cdot(\boldsymbol{r}+\boldsymbol{L})} u_k(\boldsymbol{r}+\boldsymbol{L}) = e^{i\mathbf{k}\cdot\boldsymbol{L}} \phi_k(\boldsymbol{r}) \qquad [40]$$

The periodicity of $u_k(\boldsymbol{r})$ allows us to express it as a three-dimensional Fourier series:

$$u_k(\boldsymbol{r}) = \sum_G u_k(\boldsymbol{G}) e^{i\mathbf{G}\cdot\mathbf{r}} \qquad [41]$$

where G is the reciprocal space lattice of the simulation cell, $u_k(\boldsymbol{G})$ represents complex Fourier coefficients – where the lowest eigenvectors decrease exponentially with the kinetic energy $(\boldsymbol{k}+\boldsymbol{G})^2/2$ - and the sum is over all vectors up to a user-defined cut-off energy $(\boldsymbol{k}+\boldsymbol{G})^2/2 < E_{cut}$; i.e. we include only plane-waves with energies less than this cut-off in order to achieve a finite basis set. This value is selected on a trial-and-error basis, balancing the need for the total energies to converge, with the need to reduce computational expense and thus efficiency. The value also depends on the type of pseudopotential used in the simulation, which we will discuss in the next section.

3.4.6. Pseudopotentials

In an ideal world, where computational power is limitless, we would include every electron in our calculations. However, it is not efficient to do so, as the wavefunctions closest to the nuclei are generally not useful in understanding electronic, chemical or mechanical properties of materials. That is to say, in most conditions, they inhabit locations very close to the nucleus, and are not involved in and form of chemical process. Thus, provided the screening effect that the core electrons exert on the outer electrons, and the Coulomb attraction from the nucleus are taken into account, it is possible to create a modified pseudopotential that combines an atoms nucleus and its core electrons into an ion that exerts the same force on the outer electrons. With the projector augmented wave method (PAW, Kresse and Joubert, 1999), we are able to reduce the cut-off energy and thus the number of states we need to compute, increasing efficiency.

3.4.7. K-Points

Given that we used a periodic system, we replace the real-space integrals of the Bravais lattice over the infinitely extended system, with integrals over the finite first Brillouin zone in reciprocal space. When we specify the k-points value in VASP, we are describing how we want the calculation to be divided over reciprocal space. The more k-points that are included in the calculation, the more accurate it is, and the more expensive it is. Thus, in selecting this parameter, our aim is to find a balance between accuracy and calculation time.

Following convergence tests using a number of different k-points, we note that there is no difference between results from sampling the Brillouin zone at $k = 0$, also known as the Γ point, and any of the higher order k-points investigated, because the number of atoms in our system is large (order 100).

3.5 Molecular Dynamics

We've given an overview of the theory behind the 'first principles' portion of 'first principles molecular dynamics', but before we proceed to outline the specifics of the simulations and analyses performed over the course of the current work, we must first ensure that we have some understanding of molecular dynamics.

The specific type of molecular dynamics used in this work is Born-Oppenheimer Molecular Dynamics (BOMD). This type has been selected following previous work (Sun et al., 2011) where the authors noted that, although BOMD is more expensive than some of the popular alternatives such as Car-Parrinello dynamics (Car and Parrinello, 1985), it is more robust in certain circumstances. This is due to reported inaccuracies in Car-Parrinello dynamics of system with conduction electrons (Vorberger et al., 2007), such have occurred in the high temperature limit of other oxide liquid simulations (Karki et al., 2006), and which may thus be a factor in the present work.

In this BOMD regime, as we have seen, we are able to calculate the self-consistent electronic ground state and thus the forces acting on the ions by defining molecular dynamics on the 'Born-Oppenheimer surface' with electrons that are instantaneously in the ground state. Again, this assumption is a consequence of the mass disparity between electrons and nuclei, and the nuclei velocities being correspondingly many orders of magnitude slower, that the electrons can be thought to instantaneously relax to their ground state. We evaluate the forces acting on the ions on the system at each simulation time-step via the Hellmann-Feynman theorem (Feynman, 1939), and apply classical equations of motion to the nuclei, which are treated as point-particles. The force on an ion $\boldsymbol{F}_A$ is given by:

$$\boldsymbol{F}_A = M_I \boldsymbol{a} = -\frac{dE}{d\boldsymbol{r}_{\boldsymbol{A}}} = M_A \frac{d^2 \boldsymbol{r}_{\boldsymbol{A}}}{dt^2} \qquad [42]$$

where M_A is ionic mass, $\boldsymbol{r}_{\boldsymbol{A}}$ is the position and $\boldsymbol{a}$ is the acceleration, or the second derivative of position with respect to time, $\frac{d^2 \boldsymbol{r}_{\boldsymbol{A}}}{dt^2}$. For atomic propagation, and subsequently, to obtain each new set of atomic trajectories, the velocity Verlet algorithm (Swope et al., 1982) is used to integrate the equation of motion, and the forces are recalculated after allows the electrons in the system to reach self-consistently.

For the simulations in this work, the canonical ensemble is used (where the number of molecules, the volume, and the temperature are held constant), and the system is free to exchange energy with a heat bath by the Nose-Hoover thermostat (Nosé, 1984; Hoover, 1985).

4. METHODS

In the previous chapter, we gave an overview of the theory behind DFT, in effect setting the scene for what follows. In this chapter, we describe the specific computational methods and analyses used to produce the results gathered over the course of this thesis, including both FPMD simulations and data analysis, and the specific details required to enable the reader to understand – and replicate – results. We begin this section with a description of 'universal' processes and parameter selections that are common to setting up and running each of our experimental systems, before detailing the analyses specific to each system.

4.1. FPMD SIMULATIONS

In all cases (MgSiO3, MgSiO3 + H2O), the simulations in this work are performed using the Vienna Ab Initio Package (VASP) (Kresse and Hafner, 1993; Kresse and Furthmiller, 1996). They are based on DFT, as described earlier in this thesis, and are each performed in the canonical ensemble (NVT – where the number of atoms, volume of the simulation cell and the temperature are held constant) with a periodic boundary condition. We use the generalized gradient approximation of the exchange-correlation functional, rather than the LDA , primarily to avoid the overbinding issue reported in previous work on silicate oxides (e.g. Karki et al., 2001), among others (van de Walle and Ceder, 1999), thus eliminating the need for semi-empirical corrections. Specifically, we use the recently formulated PBEsol functional (Perdew et al., 2008), selected for its improved accuracy regarding equilibrium properties for condensed matter (which may be a factor in high pressure simulations). Projector augmented wave potentials are appropriated selected in each case, keeping the high pressure conditions in mind.

Despite some minor variations in the initial conditions and total simulation length, all material simulation sets begin by melting the initial configuration at 20,000 K, for between 8 and 10 ps. The presence of melt is confirmed via the use of Radial Distribution Function plots, and Mean Squared Displacements. Each melted volume is then cooled isochorically to the temperatures of interest – or, in the case of 20,000 K runs, extended for a further 8 – 10 ps. Here, we examine structural and dynamical properties at 20,000 K, 10,000 K, 6000 K, 4000 K and 3000 K. The first ~20-40% of each set of VASP results is removed before equilibration averages are calculated.

The energy cut-off for inclusion in the plane-wave basis set is 500 eV, chosen as a balance between obtaining a high degree of accuracy, and ensuring that ionic iterations can converge in a timely, and cost-effective manner. The Brillouin zone - the Wigner-Seitz cell of the reciprocal lattice - is sampled at the centre, where wavevector k = 0, the gamma point.

4.2. INITIAL CONDITIONS

The initial condition for all experimental $MgSiO_3$ simulations is perovskite crystal, homogenously strained into a cubic cell at the desired volume. In this case, we follow the method outlined in Stixrude and Karki (2005) by choosing the reference volume $V_x = 38.9\ cm^3\ mol^{-1}$, which is the experimental value for the liquid at the ambient-pressure melting point (1830 K)(Lange and Carmichael, 1987). We then explore a range of volumes from $V_x = 1$ to $V_x = 0.5$ at intervals of 0.1, and then from $V_x = 0.45$ to $V_x = 0.2$, at intervals of 0.05.

Note that, hereafter, all references to V_x in text and in figures, is referring to the above stated definition.

Stixrude and Karki (2005) used a similar method to investigate $MgSiO_3$ liquid with an 80 atom (16 formula unit) $MgSiO_3$ supercell, and run durations of 3 ps, using the final 2.4 ps to compute equilibrium averages. To test for possible size effects and sensitivity to initial conditions, the authors also performed simulations of 160 atom cells for a total of 6 ps, and found that their results were unchanged, within statistical uncertainty. Nonetheless, in this work, we used 135 atoms (27 formula units) for all $MgSiO_3$ volumes, and ran for a total of 8 to 10 ps, using the final 3 to 5 ps to compute equilibrium averages.

The initial condition for the mixture - $MgSiO_3$ + H_2O - is obtained using a separate method, that will be discussed in greater detail in the following section. In each case, we must first determine the number of molecules of each dopant that needs to be added such that the added molecule is equivalent to 10 wt% of the overall system. This proportion of the total system was selected for ease of comparison to results of Mookherjee et al., (2008).

We achieve this by obtaining the molecular mass of the current system (27 $MgSiO_3$ unit cells with a mass of 2710.48), and calculating x, where $x = 2710.48/0.9$ = 3011.64 is the new weight of the system with 10 wt% of H_2O added. Thus, we must find the number of H_2O molecules that is roughly equal in molecular mass to $3011.64 - 2710.48 = 301.16$. For the $MgSiO_3$ + H_2O system, we add 17 water molecules, bringing the total number of atoms in the system to $135 + 51 = 186$.

4.2.1. SUPERCELL CONSTRUCTION

The initial $MgSiO_3$ perovskite computation cell is constructed using an intuitive software package called Materials Studio. The $MgSiO_3$ unit cell is first built using experimental values of the lattice parameters, in order to reduce the computational cost of static the calculations in VASP required for finding the equilibrated crystal structure. Once obtained, simple functionality in Materials

Studio permits the symmetrical construction of a specified supercell in terms of atomic coordinates, which may then be exported as a *.cif* file. The *.cif* is then opened in another software package known as Vesta, and exported as a .vasp file. We now have a 135-atom $MgSiO_3$ supercell ready for use in VASP.

In the case of $MgSiO_3$ + H_2O the presence of two separate molecules means that we are unable to reduce the problem down to a simple multiplication of unit cells into a crystalline structure. Instead, we employ the 'skew start' method developed by Refson (2001) to populate our supercells. To integrate the equations of motion in a manner that remains numerically stable, no two atoms should be too close to one another. Thus the Skew Start method was developed to populate a supercell with atomic coordinates that, although not periodic, have a guaranteed minimum separation distance, a, allowing for more stable starting conditions.

The basic concept behind the Skew Start is to create a line upon which point particles – later assigned atomic properties – can be placed. The line is then folded back into itself within the specified boundaries of the supercell, lining up in 'slices' from one corner to the other, allowing the space to fill up well, corners excepted. Different atomic species may then be assigned to the various points along the line at random, with a separation distance given by:

$$a \approx d \approx LN^{-\frac{1}{3}} \qquad [43]$$

where a is the minimum separation distance between atoms on the line, d is the separation distance between 'slices', L is the length of the side and N is the number of atoms. This concept is illustrated in Fig. 11 below.

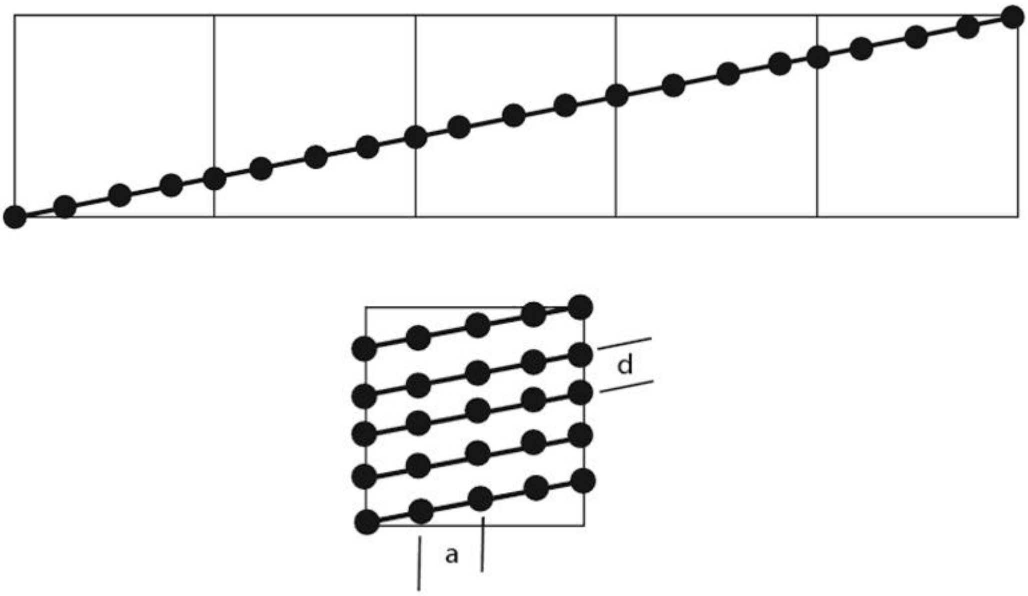

Figure 11: Illustration of the Skew-Start method of Refson (2001). Top: Atoms are placed onto a line with a minimum separation distance, a. Bottom: The line is folded within the boundaries of the simulation cell with a separation distance, d..

Initial velocities are assigned via a Gaussian distribution, and applied to a base velocity, v_{base}, as per Allen and Tildesley (1987), given by:

$$v_{base} = \sqrt{\frac{k_B T}{m_{atom}}} \qquad [44]$$

Upon testing, the Skew-Start method proved to be a success for our systems, using a starting temperature of 20,000 K, and using the software package VMD to visualize the trajectory and interaction of atoms after an initial run of 2000 time steps. A snapshot of the progress of one of these test runs on the $MgSiO_3$ + H_2O system has been included below for reference.

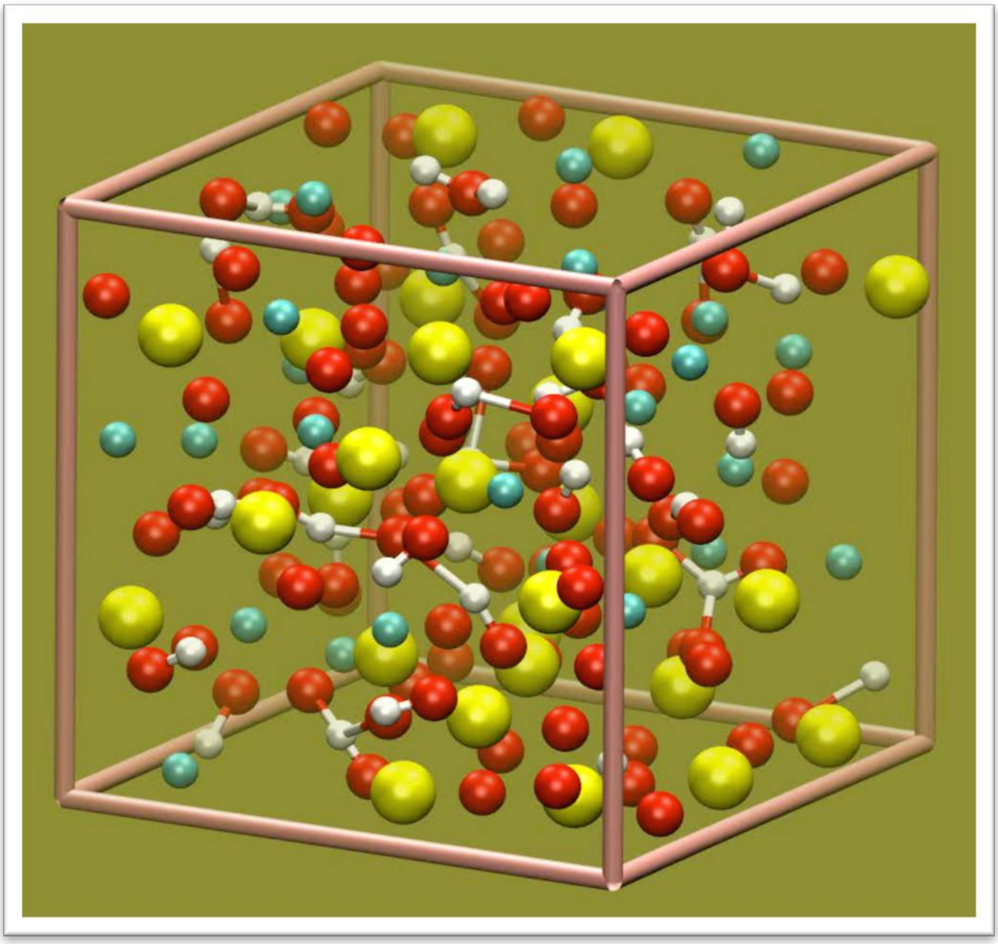

Figure 12: A snapshot from the MgSiO3 + H2O simulations at 3000 K and ~10 GPa. The yellow spheres represent Si atoms, the blue spheres are Mg, the red spheres are O and the white spheres are H. Images obtained using VMD software.

4.2.2. VASP SET-UP

Simulations are conducted in the canonical ensemble, wherein the number of particles, the volume and the temperature are held constant (NVT). We opt for a GGA functional throughout all the primary work in this thesis, given the nature of the research, in terms of examining various static and dynamic molecular and thermodynamic properties across a wide range of temperatures and pressures. Specifically, we use PBEsol (Perdew et al., 2008) on account of its greater performance for calculating e.g. equilibrium structures (Demichelis et al., 2010), which are particularly relevant to the structure-based results in this work.

The selection of appropriate PAW potentials must take into account the environments replicated over the course of the study. Given that we extend the simulations into comparatively high pressure and temperature regimes, we should seek to include an adequate number of valence electrons, where available. This allows us to account for a greater potential overlap in atomic orbitals, as compared to interactions at ambient temperature and pressure, for example. In the current work, we use: an Mg PAW potential with s2p6 valence configuration; an Si s2p2 PAW potential, and; an O s2p4 PAW potential, and a standard H pseudopotential.

We investigate 12 volumes in total, for each experimental system ($MgSiO_3$, $MgSiO_3$ + H_2O). For each volume, our first course of action is to produce a melted system. To obtain this the crystalline initial conditions are entered into an FPMD simulation at 20,000 K for a total run of 8 ps, with a timestep of 1.0 fs, numbering 8000 ionic iterations in total. This proved to be an adequate length for melting to occur in all experimental cases, as determined from inspection of the radial distribution functions, and then each volume is entered into an equilibration run of at least a further 8 ps the details of which will be discussed later in this section.

For each time step, VASP determines the electronic groundstate by initiating the runs with a trial density, and then progressing through a series of self-consistent electronic iterations until the specified value for convergence is reached. The iterations are said to be self-consistent because the density is updated when the wavefunctions are changed, such that they are consistent with each other.

In the current work, we specify the stopping criterion for the relaxation of electronic degrees of freedom to be 10^{-6} eV. In other words, we say the system is converged when the energy difference between electronic iterations drops below this value, and thus that the groundstate has been identified. Here, we set 200 electronic iterations as the convergence limit; that is, if the system has not converged to the stopping criterion before 200 iterations have lapsed, then the program is shut down, and we investigate the cause. Once these electronic iterations have converged, the internal energy is computed, along with the stress tensor and the forces acting on the nuclei, from which the Newtonian mechanics are applied (Stixrude et al., 2009).

4.3. DATA PROCESSING

In this section, we discuss the various techniques use to obtain the results reported in this thesis, beginning with the checks used to ascertain the structural and thermodynamic state of the system, and continuing with computing equilibrium averages and uncertainties, average coordination numbers and fractions, average bond lengths, equation of state, mean squared displacements and self-diffusion coefficients.

4.3.1. DETERMINING STATE

Before proceeding, we must first determine whether or not the system is in a liquid state. To do so, one of the first analyses we can perform, is to examine the radial distribution function $g(\boldsymbol{r})$, which describes the variation of density relative to a reference particle, and is mathematically defined as:

$$g(\boldsymbol{r}) = \frac{1}{N\rho}\sum_{i=1}^{N}\sum_{k\neq i}^{N}\langle\delta(\boldsymbol{r}+\boldsymbol{r}_k-\boldsymbol{r}_i)\rangle \qquad [45]$$

where N is total number of particles, ρ is the number density N/V, $\boldsymbol{r}$ is the distance to the particle from the reference particle, in angstroms, the subscripts i and k are individual species, and δ is the Dirac delta function.

The underlying premise of using the distribution function (RDF) to ascertain the state of matter is based on our understanding of typical atomic geometries in different states. In a solid, we can find neighbouring atoms to a reference atom at characteristic distances corresponding to bond lengths and packing coordination; or, in other words, we have both short and long range order, in the form of regular and predictable spacing between atoms. In a liquid, however, this spacing is irregular, and neighbouring atoms are identified at more approximate distances. Finally, in a gas, there will be an absence of long or short term ordering. One important point to consider is that an amorphous solid (such as a glass) will have an RDF that looks very similar to that of a liquid, so further steps must be taken to ascertain the state of the system when, for example, dealing with a system in which vitrification might occur. The diagram below has been added in order to illustrate these concepts visually.

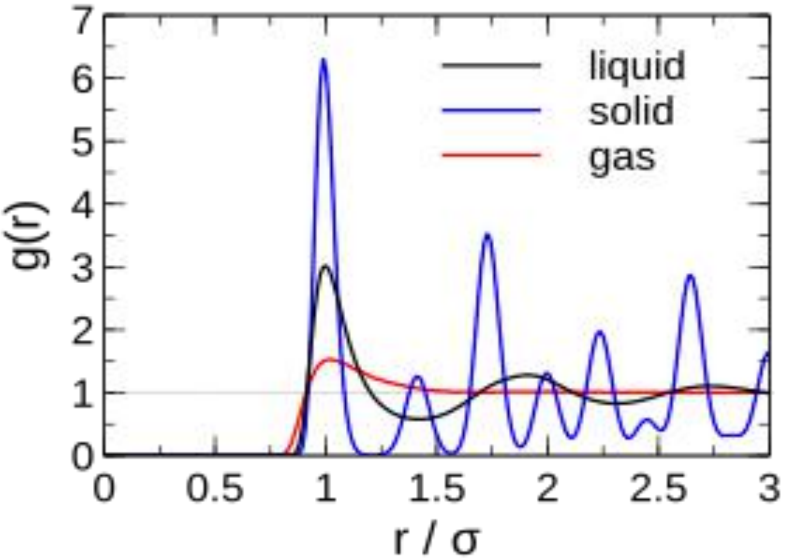

Figure 13: An RDF plot of the solid, liquid and gas states of Argon, at $T = 50\ K, T = 80\ K$ *and* $T = 300\ K$*, respectively. The radii are stated as reduced units of the molecular diameter* ($\sigma = 3.822$Å)*. The peaks represent favoured separation distances. At distances below that of an atomic diameter,* $g(\boldsymbol{r})$ *goes to zero, due to repulsive forces. The height of the peak is thus the probability that the reference atom will have a neighbor at that distance. Observing the solid line (blue), the first peak is the nearest neighbor shell, the second is the next nearest, and so on. This indicates the presence of both short and long range order. In the liquid plot, we can see that, although there is a reduced nearest neighbor peak, indicating the existence of molecular species, disorder increases with distance beyond that, while the gas is disordered throughout. Image from (Chandler 1987).*

A more practical way to consider how we might calculate the RDF from our simulation, it is useful first to conceptualise the RDF as:

$$g(\boldsymbol{r}) = \frac{\rho(\boldsymbol{r})}{\rho} \qquad [46]$$

Where $\rho(\boldsymbol{r})$ is the local density and ρ is the overall number density of the system.

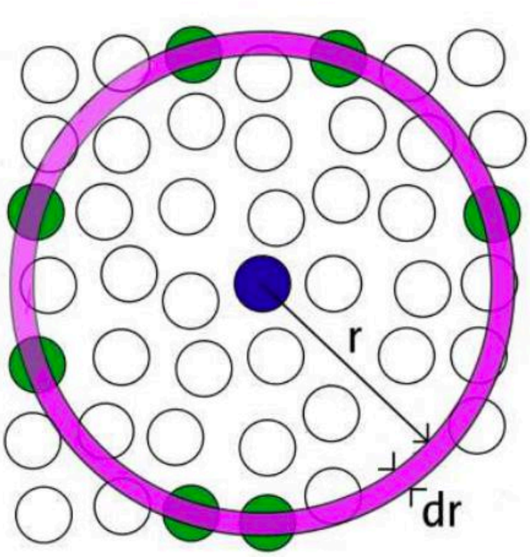

Figure 14: A visual illustration of the set-up and core components involved in calculating the radial distribution function. Image from R.I.N.G.S. (2010)

Starting with a single ‘snapshot’, we first measure the distances from reference atoms – say Si - to their nearest neighbours. Those distances are then measured for all the particles in the system, and an average is taken. Finally, we perform the same procedure for all – or a representative selection – of the snapshots across a given period of time. We calculate the RDF of a discrete spherical shell according to:

$$g(r) = \frac{< N\left(r \pm \frac{\Delta r}{2}\right) >}{\Omega\left(r \pm \frac{\Delta r}{2}\right)} \frac{1}{\rho} \qquad [47]$$

where $N\left(r \pm \frac{\Delta r}{2}\right)$ is the number of atoms in the interval $\Delta r,$ and $\Omega\left(r \pm \frac{\Delta r}{2}\right)$ is the volume of the shell dr, illustrated in Fig. 15 below:

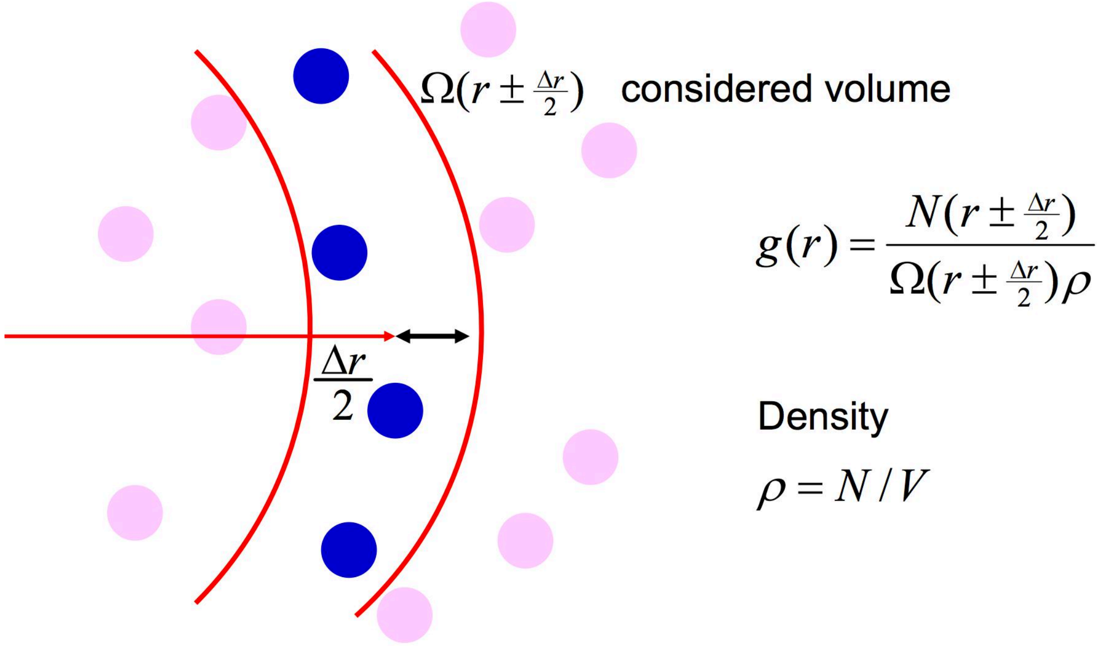

Figure 11: A visualisation of the process of RDF calculation (image from Buehler (2011)).

With respect to the time over which the distances are averaged, we must be careful not to include every snapshot. For example, our results might be compromised if we seek to understand the state of the system at the end of the run, if we include the state of the system at the beginning, if the two are expected to differ. We will consider this point in greater depth later in the thesis, when it comes to processing and analyzing our results.

Following an 8 ps melting period for all volumes from the crystalline initial condition, RDF plots were obtained for representative volumes in order to ascertain the presence of melt. Once satisfied that the systems were no longer in a crystalline state, each volume was then quenched to various temperatures of interest (3000 K, 4000 K, 6000 K, 10,000 K) and experimental runs were initiated for a further 8 ps, or simply extended for a further 8 ps, in the case of the 20,000 K volumes. These particular temperatures were chosen for the purposes of more direct and simple comparison to the earlier work of Stixrude & Karki (2005).

4.3.2. THERMODYNAMIC AVERAGES & UNCERTAINTIES

At the end of each experimental run, we remove the initial transient simulation steps and compute thermodynamic averages of internal energy and pressure. The transient removed is typically 20-40% of the total run, and is selected by plotting the time series of internal energy and pressure, as well as their moving averages, to diagnose when the system is approximately in equilibrium. If visibly large fluctuations continue to occur in the moving average toward the latter half of the run, we extend the simulation, monitoring time series and moving averages until the final ~5000 time steps are devoid of large fluctuations, and the moving average is stationary. When this occurs, we compute equilibrium averages for internal energy and pressure.

Of course, these ensemble averages must also be qualified through the estimate of statistical uncertainties. For this, we turn to the Blocking Method, as reported by Flyvbjerg and Petersen (1989). In this approach, the entire trajectory of N statistically independent snapshots is broken into M separate segments (or 'blocks') of initially a very short block length, n, for example $n = 1$. The relationship is thus $N = M \cdot n$, and the average of the observed value is calculated for each segment, such that we obtain M values for the observed quantity $\langle f \rangle_i$ for $i = 1 \ldots M$. We slowly increase the block length and recalculate the set of averages for each block length. In addition, for each n value, the standard deviation among the block averages, σ_n, is used in calculating an estimate of the overall standard error, according to:

$$BSE(f, n) = \frac{\sigma_n}{\sqrt{M}} \qquad [48]$$

Which we can thus describe as the standard error (or Block Standard Error, BSE), for the observable value, in the estimate of the mean based on trajectory segments of block length n. When block lengths are small (and when the number of blocks is large) for highly correlated consecutive blocks, then BSE underestimates the error, since the expression is only true when the blocks M are statistically independent. Conversely, when the blocks are statistically independent (when n is substantially greater than the correlation time) BSE will not vary with n, and will thus function as a reliable estimate of the true standard error of the mean (Grossfield & Zuckerman, 2009).

4.3.3. COORDINATION NUMBER & BOND LENGTH

We can use coordination statistics to give an indication of the short-range structure of a given material. They tell us how many nearest neighbor atoms of a particular species are within bonding distance of a reference atom, and can impart some insight into the coordination state of a particular species within a material, at temperature-pressure environments of interest. In order to compute the coordination statistics of atom β around that of a central atom α, we must compute the distance from a single α to every atom β. The number of these β atoms that are found within a shell - of a thickness less than the nearest neighbour cutoff distance – are then accumulated. This process if repeated for every central α in the system, first for that snapshot, and then over all other snapshots.

To describe this process mathematically, we must first extend our earlier discussion of the Radial Distribution Function. It is possible – and, indeed, preferable in this case - to compute a partial RDF, $g_{\alpha\beta}(\boldsymbol{r})$ - that is, the number of β atoms within a distance $\boldsymbol{r}$ from an α atom - by distinguishing the distinct atomic species in a system. Via the discretization method discussed earlier, we know that for a given central atom, we can compute the number of surrounding atoms $dn(\boldsymbol{r})$ at a distance between $\boldsymbol{r}$ and $\boldsymbol{r} + d\boldsymbol{r}$. When we distinguish the species in the system, we find the partial RDF via:

$$g_{\alpha\beta}(\boldsymbol{r}) = \frac{dn_{\alpha\beta}(\boldsymbol{r})}{4\pi r^2 d\boldsymbol{r}\rho_\alpha} \qquad [49]$$

where $\rho_\alpha = Nc_\alpha/V$ and c_α is the concentration of species α.

Recall that the RDF is a definition of the probability of finding an atom at a distance r from a reference atom. The coordination number thus is an indication of how many molecules may be found within the range of a coordination sphere, meaning that, if we integrate $g_{\alpha\beta}(r)$, in spherical coordinates, to the first minimum of the RDF, then we obtain the coordination number of a molecule:

$$Z_{\alpha\beta} = 4\pi p x_\beta \int_0^{r_{\alpha\beta}^{min}} r^2 g_{\alpha\beta}(\boldsymbol{r})\, dr \qquad [50]$$

where $r_{\alpha\beta}^{min}$ is the distance to the first minimum in $g_{\alpha\beta}$, p is the number density, and x_β is the number fraction of β (Sun et al., 2011). Applying this over all reference atoms in a given snapshot (for example, all Si atoms, α, coordinated to O atoms, β), and over all snapshots in the duration of interest, then we can use the results to obtain both coordination fraction and mean coordination number.

Finally, we can obtain the mean separation $\langle\boldsymbol{r}\rangle$ over the first coordination according to:

$$\langle r \rangle = \frac{\int_0^{r_{\alpha\beta}^{min}} r^3 g_{\alpha\beta}(\boldsymbol{r})\, dr}{\int_0^{r_{\alpha\beta}^{min}} r^2 g_{\alpha\beta}(\boldsymbol{r})\, dr} \qquad [51]$$

and bond length is defined as the mode of the first peak in the partial RDF (McQuarrie, 2000).

4.3.4. EQUATION OF STATE

The equation of state is a useful tool for bringing together state variables that can describe the thermodynamic properties of our system in a given temperature-pressure environment. Typically, it is used in order to enable correlation between fluid system densities and particular temperature and pressure regimes. In this work, we use the third-order isothermal Birch-Murnaghan equation of state, which approximates the relationship between volume and pressure, and which can be obtained via the expansion of the free energy as a function of Eulerian finite strain:

$$P(V) = \frac{3B_0}{2}\left[\left(\frac{V_0}{V}\right)^{7/3} - \left(\frac{V_0}{V}\right)^{5/3}\right]\left\{1 + \frac{3}{4}({B_0}' - 4)\left[\left(\frac{V_0}{V}\right)^{2/3} - 1\right]\right\} \qquad [52]$$

where B_0 is the bulk modulus, V_0 is a reference volume, V is the compressed volume and ${B_0}'$ is the derivative of the bulk modulus with respect to pressure. When computing the Birch-Murnaghan equation of state, we typically guess the bulk modulus and its derivative using any available experimental data, and run the computation across iterations until we find the best fitting values to the simulated pressure-volume data.

4.3.5. HEAT CAPACITY AND GRUNEISEN PARAMETER

A material's heat capacity informs us of the amount of energy that would be required to heat a given mass of that material to a given temperature; that is to say, heat capacity is quantitatively linked to enthalpy and entropy, but is also directly measurable. Heat capacity can take two separate forms, depending on whether the system is being held at constant pressure, or at constant volume. Here, we hold our systems constant in volume ($dV = 0$), but the pressure fluctuates, so we're concerned with the isochoric heat capacity, C_V.

We use two different method to obtain C_V values in the current work, primarily in order to compare and contrast the results. The first is a finite differences method; a discretization method in which finite differences approximate derivatives. This is trivial to obtain by utilizing the thermodynamic average quantities of internal energy at the same volume, over different temperatures, according to the following relation:

$$C_V = \left(\frac{\partial E}{\partial T}\right)_V \approx \left[\frac{dE}{dT}\right]_V = \left[\frac{E_2 - E_1}{T_2 - T_1}\right]_V \qquad [53]$$

Where the final result gives the value for C_V at a temperature midway between T_1 and T_2.

The other method for obtaining C_V used in this work allows us to obtain the value directly from the results of a single simulation cell. In the canonical ensemble, it is contact with a thermal bath (in this case the Nosé thermostat) that gives the system its temperature. Thus the system is no longer isolated and the Hamiltonian (total energy) is not conserved, so we should expect fluctuations. Thus, we must consider the total energy in thermodynamics as the ensemble average of the Hamiltonian in statistical mechanics. In other words:

$$(\Delta E)^2 \equiv \langle E^2 \rangle - \langle E \rangle^2 \qquad [54]$$

To consider this in terms of extracting a value of C_V from our simulations, it can further be shown, via derivation of the partition function, that:

$$\langle E^2 \rangle - \langle E \rangle^2 = k_B T^2 \left(\frac{\partial E}{\partial T}\right)_V = k_B T^2 C_{V\_FDT} \qquad [55]$$

where k_B is the Boltzman constant.

It should be noted, however, that to calculate C_V using this method, we do not use the total energy values that are outputted from VASP directly. The total energy itself has three contributions: the internal energy, primarily comprising the potential energy among atoms in the system; the kinetic energy from the translation-like motion of the atoms at finite temperature, and; the thermal energy of the electrons. In our simulations, the thermal energy of the electrons is fixed using a specific tag (SIGMA in VASP), and so fluctuation is not a property of the electronic subsystem. Thus, we instead use the internal energy from VASP when computing C_V, and separately add the kinetic energy contribution of the ions, and the heat capacity associated with the electron thermal excitation:

$$C_{V_{FDT}} = \frac{\langle U^2 \rangle - \langle U \rangle^2}{k_B T^2} + KE + C_{V_{elec}} \qquad [56]$$

where U is the internal energy of the system, KE is the kinetic energy of the ions, and $C_{V_{elec}}$ is the heat capacity associated with the thermal excitation of the electrons. We follow De Koker & Stixrude (2009) in approximating a functional fit for $C_{V_{elec}}$ as follows:

$$C_{V_{elec}} = T\left(\frac{dS_{el}}{dT}\right)_V \qquad [57]$$

where S_{el} is the electronic entropy, and can be fitted at different temperatures using the following expression:

$$S_{el} = \zeta\left[T - T_{el} - T_{el}\ln\frac{T}{T_{el}}\right] \qquad [58]$$

where T_{el} is the temperature in silicate liquids, above which electronic contributions become significant, and is related to the melting temperature, T is the temperature of the system, and ζ is the thermo-electronic heat capacity; both T_{el} and ζ must be assigned initial 'guess' values. We calculate S_{el} separately for the same volume across a range of temperatures, and fit the results to the following expression to estimate $C_{V_{elec}}$:

$$C_{V_{elec}}(V,T) = \begin{cases} \zeta(V)[T - T_{el}(V)] & T \geq T_{el} \\ 0 & T \leq T_{el} \end{cases} \qquad [59]$$

Thus enabling us to obtain fitted values for S_{el} and $C_{V_{elec}}$ ostensibly for any temperature, for a given volume (De Koker & Stixrude, 2009).

Finally, we obtain a value for the Grüneisen parameter, γ. In many materials, γ is independent of temperature or internal energy, and is thus a one-parameter function of volume, leading directly to the Mie-Grüneisen approximation and equation of state , and which is calculated via the finite differences method used to obtain C_V and discussed above:

$$\gamma = V\left(\frac{\partial P}{\partial E}\right)_V = \frac{V}{C_V}\left(\frac{\partial P}{\partial T}\right)_V \approx \frac{V}{C_V}\left[\frac{dP}{dT}\right]_V = \frac{V}{C_V}\left[\frac{P_2 - P_1}{T_2 - T_1}\right]_V \qquad [60]$$

4.3.6. MEAN SQUARE DISPLACEMENT AND SELF-DIFFUSION

The mean squared displacement (MSD) is a useful tool in statistical mechanics for diagnosing whether or not the atoms in a system are moving diffusively, and at what rate. Thus, we can use the MSD to ascertain dynamical convergence and whether or not our system is a fluid state. It is calculated according to:

$$MSD(\Delta t) = \langle (x(t) - x(t_0))^2 \rangle \qquad [61]$$

where $x(t)$ is the position of an atom at time t, with the average being taken over all snapshots from time origin t_0 (here we include just the final 3 ps of each equilibrium run) and Δt is taken as the difference between t and t_0. The system can be concluded to be in a fluid state and in dynamical convergence when the MSD shows a linear trend over time.

However, we must pay close attention to the fact that the ensemble average is taken over all atoms in the system, which can give misleading results if there is a large mass disparity between atomic components. For example, in $MgSiO_3$ + H_2O, hydrogen is substantially lighter than any other component. Observing the respective MSD plots, we may be tempted to conclude that, at the same temperature and pressure, $MgSiO_3$ + H_2O is substantially more diffusive than $MgSiO_3$, when in fact it is merely the hydrogen in the system artificially boosting the ensemble average.

Thus, it is useful also to examine the self-diffusion coefficient for atom types individually, to get a more thorough understanding of dynamical behaviours. The self-diffusion coefficient, D, is calculated by dividing the linear portion of the MSD according to:

$$D = \frac{1}{2d} \lim_{\Delta \to \infty} \frac{MSD(\Delta t)}{\Delta t} \qquad [62]$$

where d refers to the dimensionality of the system ($d = 3$ in our case).

5. RESULTS

In this section, we will examine our results-so-far, before outlining – in the next section – possible future work. This section will be organized by composition (homogenous $MgSiO_3$ and $MgSiO_3 + H_2O$) in the first instance, with each subsection comprising structural results, thermodynamic results, and transport properties.

5.1. $MgSiO_3$ STRUCTURAL PROPERTIES

In terms of structural properties, we have calculated the mean Si-O bond lengths and mean Si-O coordination number across all volumes ($V = Vx\ to\ V = \frac{Vx}{5}$) and all isotherms (3000 K, 4000 K, 6000 K, 10,000 K and 20,000 K). The Si-O coordination environments have also been plotted for the 3000 K and 4000 K isotherms. All results will be compared, where possible, with relevant previous research, including both experimental and theoretical work.

Prior to discussing our results, it would first be instructive to examine some of our radial distribution functions (Fig. 16), as per the discussion in section 4.3.1.

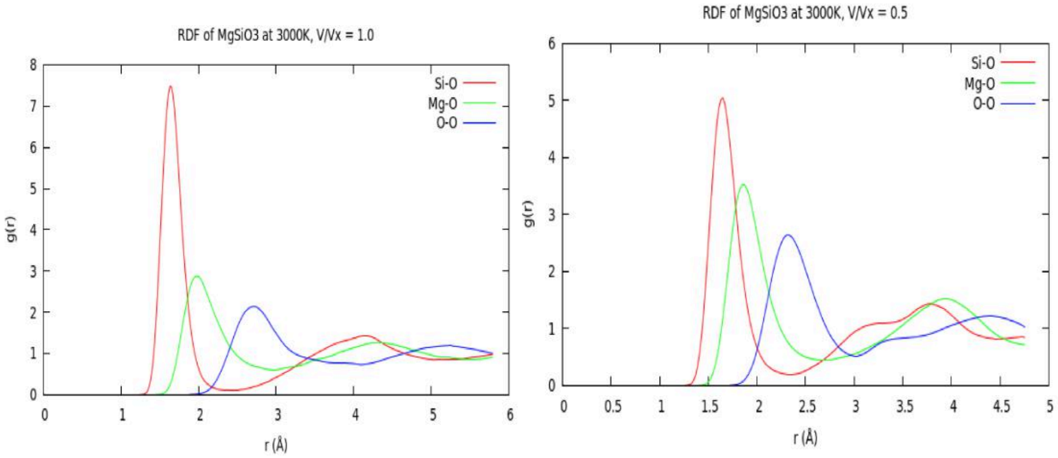

Figure 16: The RDF of Si-O, Mg-O and O-O pairs in $MgSiO_3$ at 3000K, for the volume $\frac{V}{V_x} = 1.0$ *(left) and* $\frac{V}{V_x} = 0.5$ *(right). Note that all species show nearest neighbour peaks, indicating strong charge ordering. However, the 'tails' are consistent with a liquid or amorphous solid state. From the current work.*

As we can see from the RDF plots from the 3000 K $MgSiO_3$ simulations, our system for each given volume is either liquid, or an amorphous glass. The RDF plots show a similar distribution for all examined volumes and temperatures. Analysis of the transport properties of these systems (discussed later in this section) will give a more clear insight into system state (i.e. whether liquid, or glass). For now, we assume that our system has indeed entered the liquid phase from a crystalline initial condition.

5.1.1. MEAN Si-O BOND LENGTHS

The method for calculating bond lengths is outlined in section 4.3.3. Here, we begin with an analysis of the mean Si-O bond length in $MgSiO_3$ liquid across all volumes and isotherms. These data are plotted in Fig. 17 below.

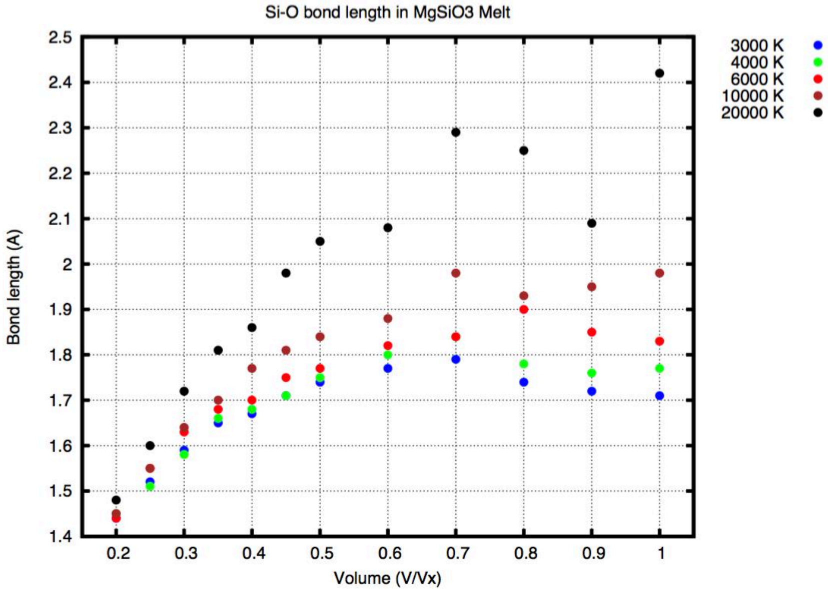

Figure 12: Mean Si-O bond length (in Å) of $MgSiO_3$ liquid at temperatures ranging from 3000 K to 20,000 K and pressures from 2 GPa to 2.9 TPa, where $V_x = 38.9\,cm^3\,mol^{-1}$, the experimental value for the liquid at the ambient-pressure melting point (1830 K), as per Lange and Carmichael, 1987. Note that some of these data points may represent systems that have undergone vitrification, particularly as volumes decrease. Note also that this work was among the earliest that I completed, and I made an assumption that the error bars would be smaller than the size of the points, as per work from other researchers in my group. The higher temperature results seem to invalidate this assumption.

The data for all isotherms behave almost linearly at the lower volumes (i.e. from V/Vx = 0.5 to V/Vx = 0.2), reflecting much more homogeneous compression, as compared with the large volumes where the Si-O bond actually expands on compression. This may be related, in some cases, to vitrified states, or it may simply be a function of reduced degrees of freedom due to extreme pressures. For the higher temperature, higher volume runs, the data behave erratically, especially on the 20,000 K isotherm. Further investigation is required to determine the cause of this behavior, which may be simply a function of much greater thermal energy and degrees of freedom and thus noise in the determination of the mode of the radial distribution function.

5.1.2. MEAN Si-O COORDINATION NUMBERS AND ENVIRONMENTS

The calculated mean coordination numbers are given in Fig. 18, and compare very well with the work completed previously by Stixrude & Karki (2005). It's interesting to note that the coordination number, for all but the highest temperature isotherm, continues to increase in a linear manner, reaching a maximum of between 8 and 8.5. Again, we see erratic behavior from the larger volume 20,000K points. For comparison, the equivalent plot from Stixrude & Karki (2005) is printed below (Fig. 19).

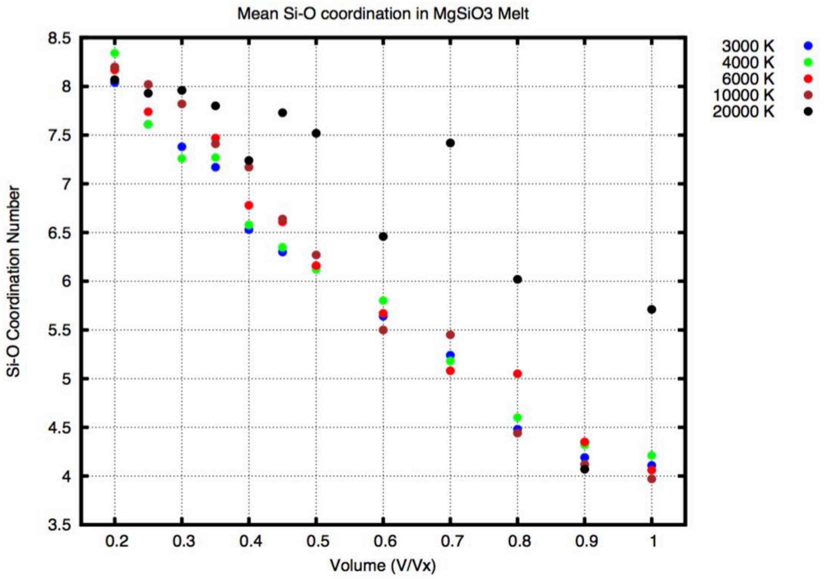

Figure 13: Mean Si-O coordination number of MgSiO$_3$ liquid at temperatures ranging from 3000 K to 20,000 K and pressures from 2 GPa to 2.9 TPa. The same caveat applies to the results for bond length, e.g. that some data points may be vitrified. Note that this work was among the earliest that I completed, and I made an assumption that the error bars would be smaller than the size of the points, as per work from other researchers in my group. The higher temperature results seem to invalidate this assumption.

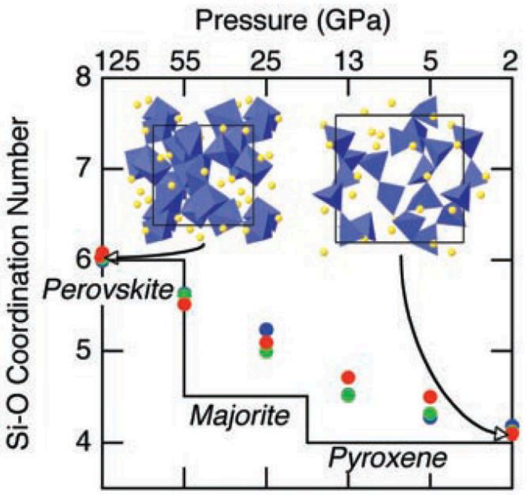

Figure 19: Mean Si-O coordination number in MgSiO$_3$ liquid, from Stixrude and Karki (2005). Red, green and blue dots represent 3000 K, 4000 K and 6000 K runs, respectively, with a pressure range that spans the Earth's mantle.

The coordination environment plots in Fig. 20 and Fig. 21 below, demonstrate the average coordination number of the silicon atoms in the system, and the fraction that are of coordination 4, 5, 6 and so on. These plots have thus far only been produced for the 3000 K and 4000 K systems, but excellent agreement is shown with that of previous work by Stixrude & Karki (2005). In addition, and as noted in the aforementioned work, there does not appear to be a significant temperature dependence on the overall shape of the coordination environments over the examined temperatures (3000 K and 4000 K).

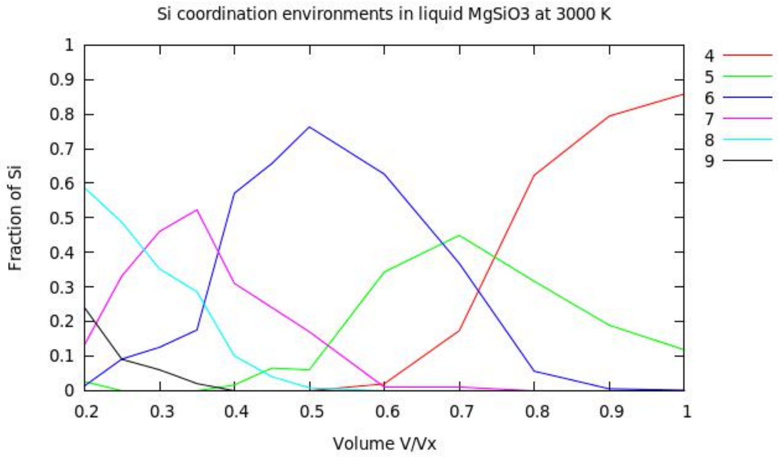

Figure 14: Si-O coordination environment in MgSiO$_3$ liquid at 3000K (this work).

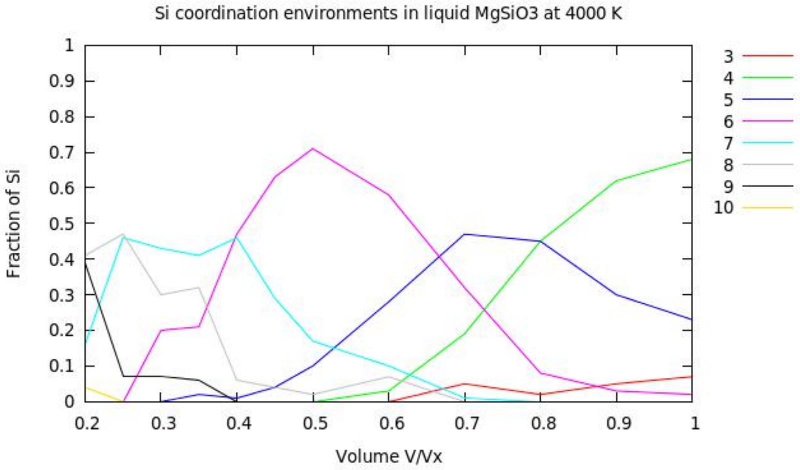

Figure 15: Si-O coordination environment in MgSiO$_3$ liquid at 4000K (this work)

5.2. $MgSiO_3$ THERMODYNAMIC PROPERTIES

5.2.1. EQUATION OF STATE

The equation of state (EOS) for silicate liquids has been explored experimentally, but has primarily been limited to the ambient and upper mantle temperature and pressure regimes (e.g. Lange & Carmichael, 1987; Courtial et al., 1997; Ai & Lange, 2008). The EOS at the higher temperatures and pressures of lower mantle environments has been probed by several shock loading and multi-anvil studies (e.g. Rigden et al. 1989; Chen et al., 2002; Sakamaki et al., 2006), but little exists in terms of experimental EOS data at the extremes of temperature and pressure considered in this paper. As a first step toward constraining the EOS for molten $MgSiO_3$ in these extreme conditions, we have calculated the Birch-Murnaghan EOS across all volumes and isotherms.

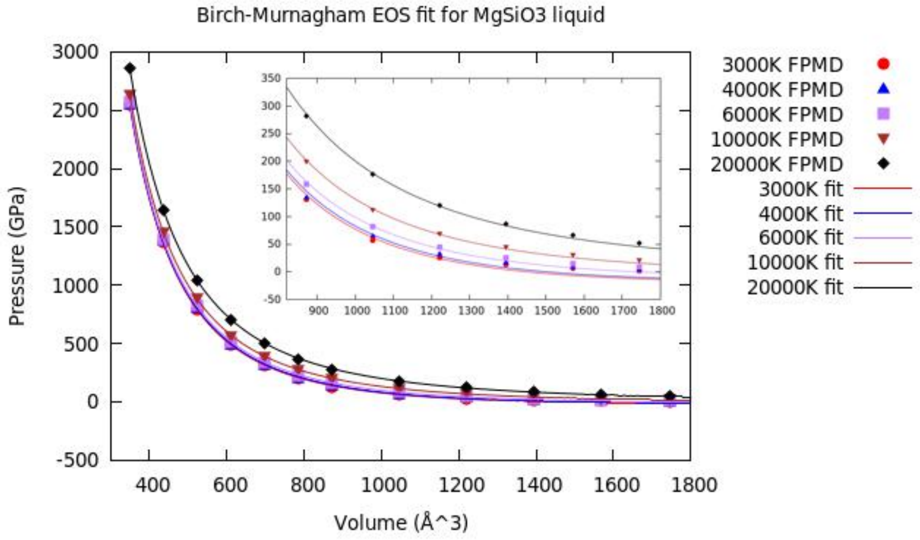

Figure 22: The BM-EOS for $MgSiO_3$ liquid, at temperatures ranging from 3000K to 20000K, and at pressures ranging from ~2 GPa to ~2.9 TPa. Note that the uncertainties in pressure are smaller than the FPMD symbols. Inset: A more close-up view of the higher-volume data points.

The EOS parameters found at 3000 K are volume V_0 of $1.45\ x\ 10^3 \dot{A}^3$ per cell, an isotheral bulk modulus, K_0, of 9.84 GPa with a bulk modulus pressure derivative, K_0' of 4.01.

Comparing our EOS in the inset portion of Fig. 22, with that of previous work (e.g. De Koker & Stixrude, 2009), we see a generally good agreement. However, the BM-EOS is physically based upon the concept that volumetric strain completely characterizes the thermodynamic properties of materials, and that temperature influence can be applied via the temperature dependence of parameters like the bulk modulus (Jing & Karato, 2011). This is valid when free-energy is influenced primarily by the internal energy of the system. If it transpires (as per Jing & Karato, 2011) that it is not the internal energy, but instead the entropy, that changes most when silicate liquids are compressed, then the BM-EOS may not be so simple to borrow from the analysis of solids to be used in the case of silicate melts. Thus, an alternative approach to calculating the EOS may be required.

5.2.2. HEAT CAPACITY

The heat capacity for each volume has been calculated using both the finite differences and fluctuation methods described in 4.3.5., and plotted in Fig. 23 below.

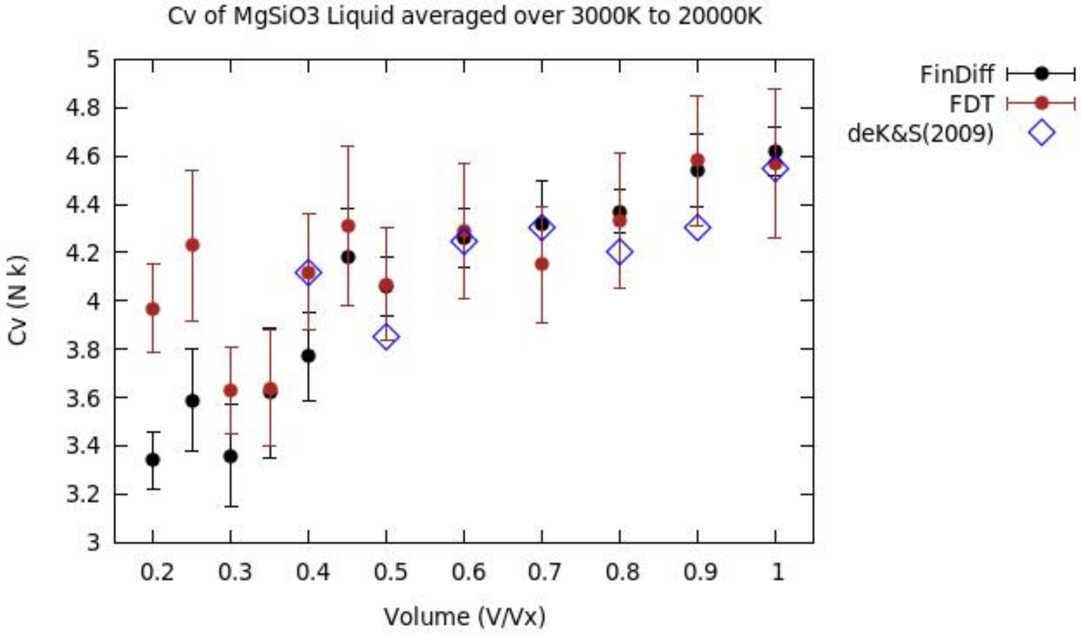

Figure 23: The average heat capacity for each volume, obtained using both the finite differences method (FinDiff, black) and the fluctuation formula (FDT, brown). Blue diamonds show values from De Koker & Stixrude (2009). Values per volume are calculated as averages from multiple isotherms, as described in section 4.3.5.

Heat capacity averages are calculated using volumes across isotherms (detailed in section 4.3.5) by methodological necessity in the case of FinDiff calculations, and by means of fair comparison in the case of fluctuation formula results. In order to compare with previous work (Stixrude & Karki, 2005; De Koker & Stixrude, 2009), during which 6000 K and 8000 K were the largest temperatures examined, respectively, we calculated averages values for the heat capacity using only 3000 K, 4000 K and 6000 K isotherms up to lower mantle pressures (V/Vx = 0.5, or roughly ~125 GPa).

In general, we see good agreement with the previous values of De Koker & Stixrude (2006) and Stixrude & Karki (2005), as well as good agreement between the two different methods used to calculate the heat capacity. However, this is only true until we reach the highest temperature isotherms at 10,000 K and 20,000

K. Here, we begin to see discrepancies between the results from the fluctuation formula and FinDiff calculations.

To investigate this discrepancy further, we first plotted the mean heat capacities calculated via fluctuation formula and FinDiff methods, in the higher temperature regimes. Fig. 24 below shows the mean values obtained using data from the 6000 K and 10000 K runs.

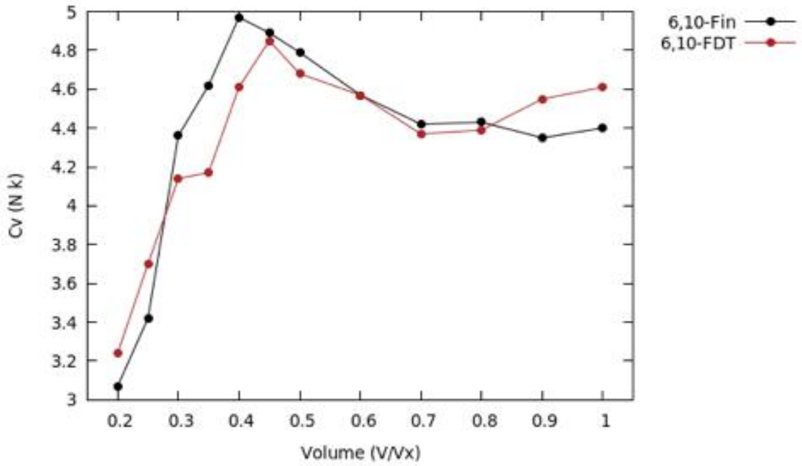

Figure 24: Mean heat capacities obtained as the average values of the heat capacity between 6000 K and 10,000 K results, using finite differences (black) and fluctuation methods (brown). Note that these plots (Fig. 24 and 25) are for illustrative purposes only, and should not be considered as results, hence the lack of error bars.

As we can see, when we use results from the 6000 K and 10,000 K runs, we retain good agreement between the heat capacity result obtained via each method. However, in Fig. 25 below, we begin to see a divergence.

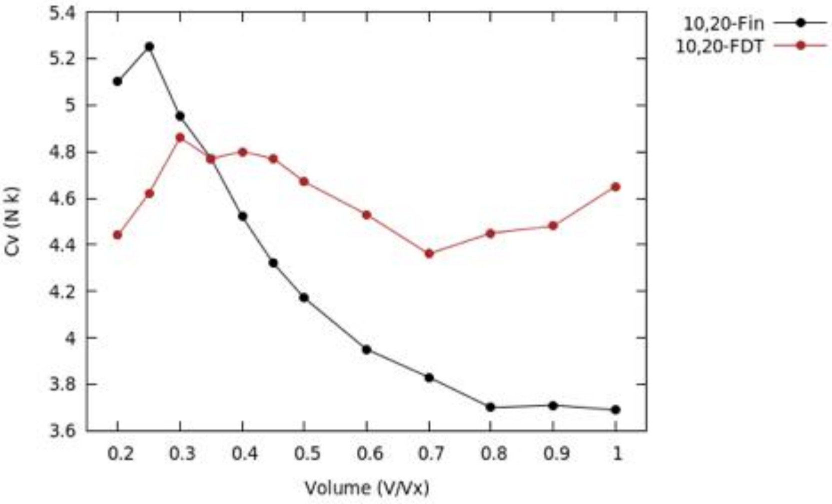

Figure 25: Mean heat capacities obtained as the average values of the heat capacity between 10,000 K and 20,000 K results, using finite differences (black) and fluctuation methods (brown).

As can be noted, we begin to see very notable divergence in the results from using these methods in the higher temperature regime. Given that both methods use the same raw data from the simulations, the difference in heat capacity must be down to the methods employed in obtaining the heat capacity. When using the fluctuation method, it is necessary to separately estimate and include the electronic contribution to the heat capacity. This estimate may be the source of this discrepancy. To examine the possibility, we plotted the heat capacity obtained from fluctuation formula calculations, both using the ionic heat capacity alone, and including the electronic contribution (Fig. 26 and 27).

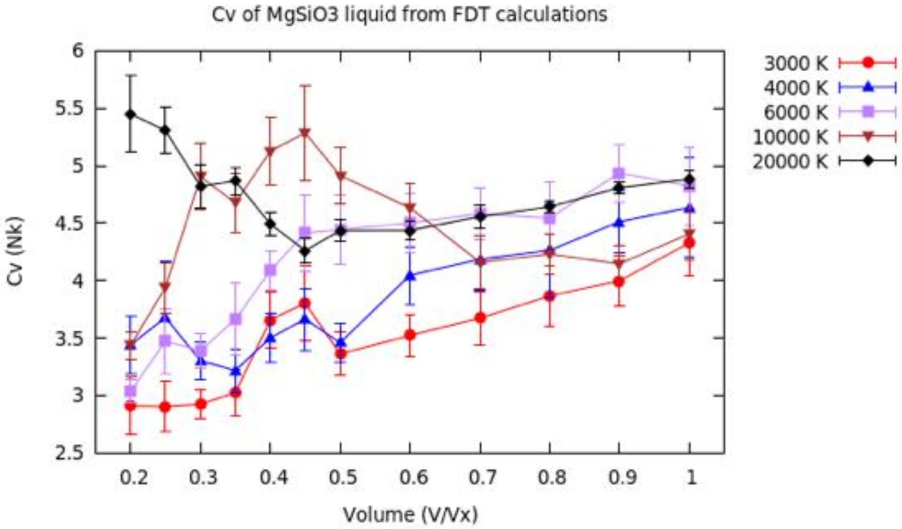

Figure 26: Heat capacity of $MgSiO_3$ liquid obtained from the fluctuation formula, including electronic and kinetic contributions to the total.

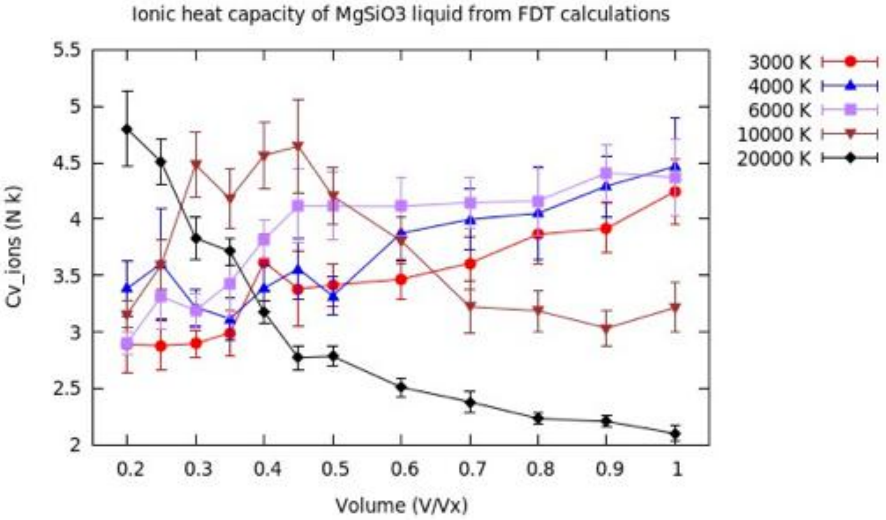

Figure 27: Ionic heat capacity of $MgSiO_3$ liquid, obtained from fluctuations in the internal energy, as calculated directly from VASP results.

From Fig. 26 and 27, we see that the electronic contribution to the heat capacity remains low for the 3000 K, 4000 K and 6000 K results, across volumes. However, this is not the case for the 10,000 K and especially for the 20,000 K results, where the electronic contribution clearly becomes much more significant. Thus, in moving forward with this work, we intend to investigate and clarify the suitability – for the higher temperature regimes - of the fitting function we currently use for estimating the electronic contribution to the heat capacity.

5.2.3. GRÜNEISEN PARAMETER

The Grüneisen parameter has traditionally been used in the study of solids, with respect to relating thermodynamic properties to lattice vibrational spectra. However, the concept has since been extended to understanding the structure and properties of liquids, include silicate melts (Arp et al., 1984). It has been consistently found that γ decreases upon compression in crystalline solids, including mantle materials (Stixrude & Lithgow-Bertelloni, 2005), yet, according to both theory and experiment, the opposite appears to be true for silicate liquids (Stixrude & Karki, 2005; Mosenfelder et al. 2007; De Koker & Stixrude, 2008; Asimow, 2012). This behavior has been understood as a consequence of pressure-induced structural changes in the liquid (Stixrude & Karki, 2005).

One of the initial questions that we sought to address through the course of this work, was whether γ would continue to increase almost linearly into the higher pressure and temperature regimes. In Fig. 28 below, we see good agreement with the work of previous authors where conditions overlap. We also see that this increase in the Grüneisen parameter on compression appears to reach a maximum of between ~1.0 and ~1.15, before again decreasing with pressure. The source of this behavior is yet to be determined, and some questions still remain over whether the material is indeed liquid or vitrified in the higher pressure volumes, especially at lower temperatures. This will be investigated in the following section.

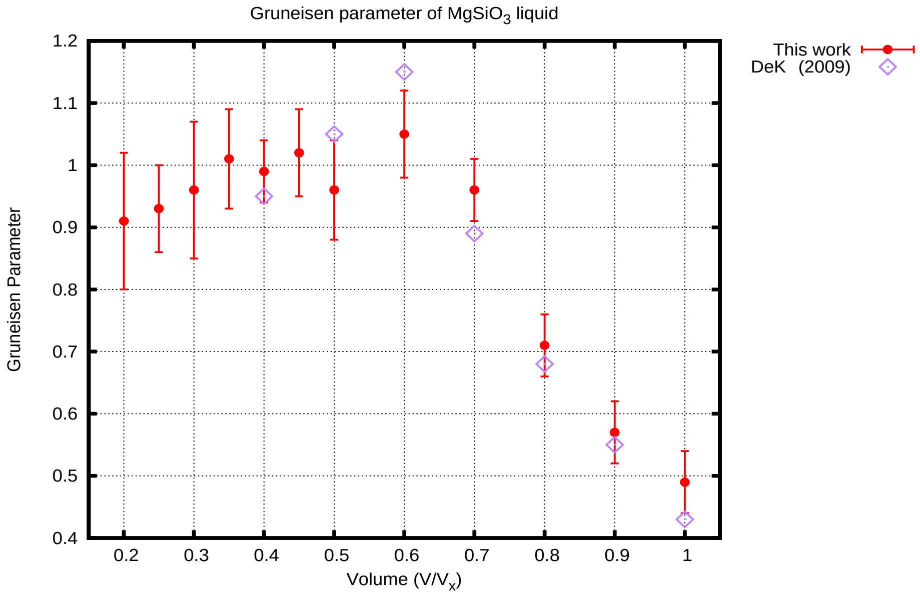

Figure 28: Grüneisen parameter of MgSiO$_3$ liquid, averaged across pressures ranging from ~2 GPa to ~2.9 TPa, and across temperatures of between 3000 K and 20,000 K. The red circles are from the current work, and the purple diamonds are taken from De Koker & Stixrude, 2009.

5.3. $MgSiO_3$ TRANSPORT PROPERTIES

Here, we investigate the transport properties of silicate liquids, and of their components, including both mean squared displacements, and self-diffusion coefficients. Doing so allows us to gain a greater understanding of the state of our system across the temperature and pressure regimes of interest, when combined with results from our various other analyses, as discussed earlier in this work (e.g. RDF). We first demonstrate the MSD results for each volume across each temperature studied, and follow this with a more in-depth analysis of the self-diffusion coefficients.

5.3.1. MEAN SQUARED DISPLACEMENTS

The method for calculating MSD results is outlined in section 4.3.6. Results are given for each temperature in Fig. 29 below. We can begin to diagnose the state of the system (liquid or glass) by observing the MSD plots for each volume; specifically, the closer a given plot line is to the horizontal, the less diffusive the atoms in the system are, on average. Especially in the lower temperature runs, we can see that numerous low volume MSD results seem to cluster together close to the horizontal, indicating very little mean diffusivity.

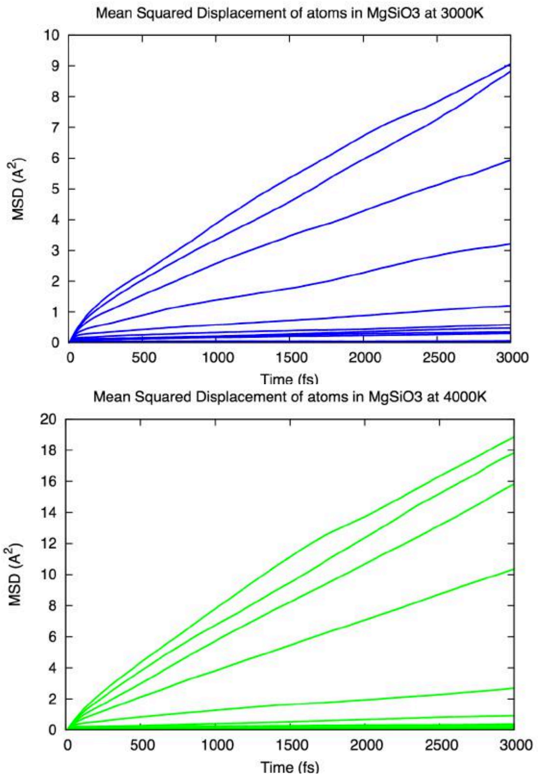

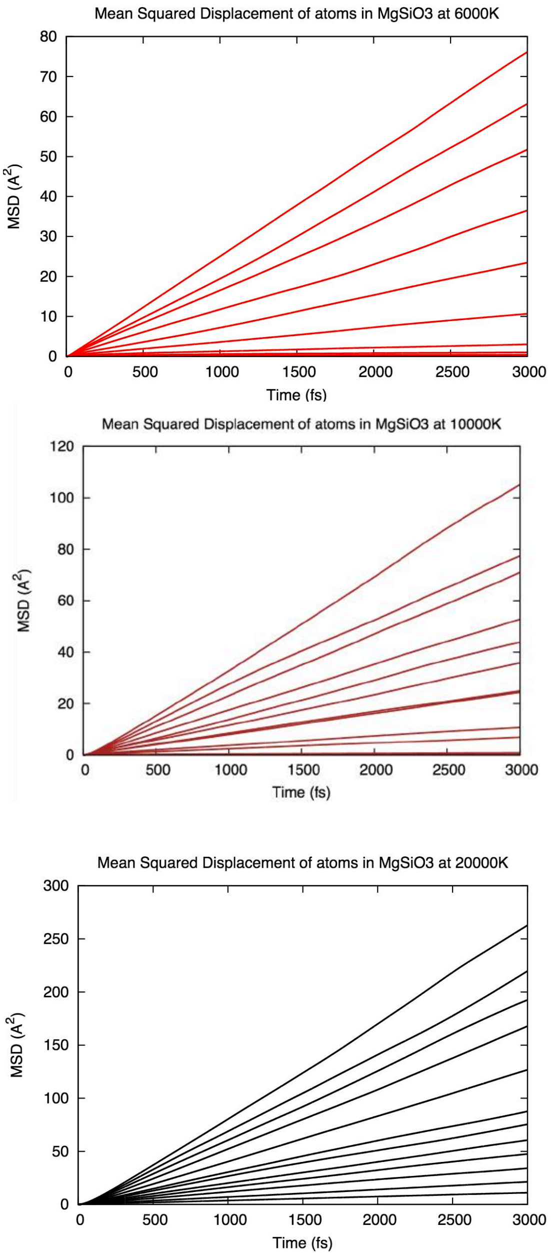

Figure 29: Mean Squared Displacements for atoms in $MgSiO_3$ liquid at temperatures ranging from 3000 K to 20,000 K. In each case, the line with the steepest gradient represents V/Vx = 1.0, while the line with the shallowest gradient represents V/Vx = 0.2.

5.3.2. SELF-DIFFUSION COEFFICIENTS

Self-diffusion is a measure of the amount of spontaneous molecular or atomic mixing that takes places within a system, in the absence of an applied concentration or potential gradient. Gaining some understanding of the diffusivity in a system can generate insight on a wide range of phenomena, from bulk mass transport, to proton currents and magnetic fields. Here, however, we begin with utilizing the self-diffusion coefficients in the first instance to ascertain the functional nature of diffusive behavior in silicate melts at extreme conditions, and to assist in diagnosing whether or not the system – at a specific temperature and volume – is likely to be liquid, or vitrified glass. We suggest that, should the atoms of the system be moving, on average, less than the distance of a typical Si-O bond (~1.5 x 10^{-10} m) in any direction, the system may reasonably be considered vitrified. Also note that we have selected a log-log plot, as opposed to the more common log-linear, to display this data. While the latter may be adequate for pressure regimes that span less widely than in the current study (see Fig. 9 and 10), we find the log-log plot more helpful in visualizing system transport behaviours in the current work. Fig. 30 shows each plot style side-by-side for a clear comparison, and to more clearly demonstrate the reasoning behind our decision to use log-log plots in this work.

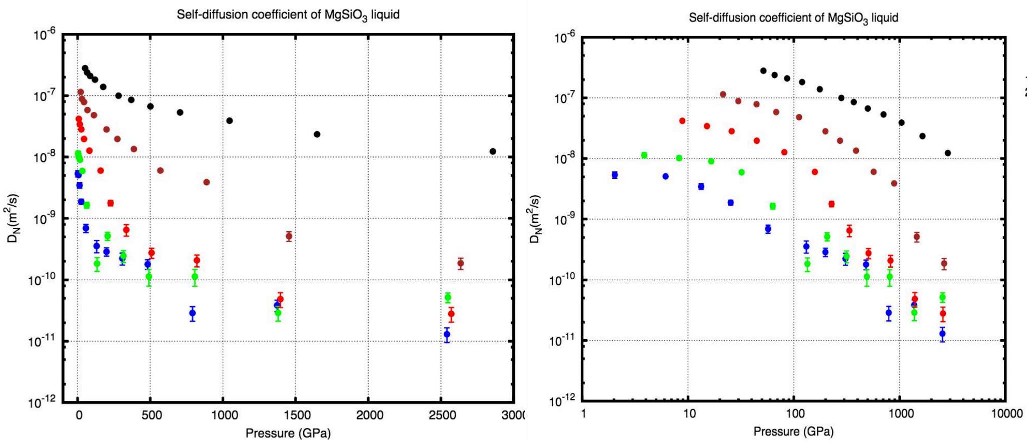

Figure 30: The mean diffusivity in $MgSiO_3$ melt simulations, visualized on a log-linear plot (left) and a log-log plot (right). The blue dots are at 3000 K, green 4000 K, red 6000 K, brown 10,000 K, black 20,000 K.

Of particular note here is the surprising result that the pressure and temperature dependence of the diffusivity across this regime does not follow an Arrhenian fit, as previously found for pressures ranging up to, and somewhat beyond, that of the lower mantle (e.g. De Koker et al, 2008). Observing the log-log plot, we can also see that, at a point between $D_N=10^{-9}$ m^2/s and $D_N=10^{-10}$ m^2/s, the data points lose their predictable, well-behaved trajectory, further suggesting a change in system state (e.g. vitrification).

A more useful, and in-depth, analysis of diffusivity involves examining each of the component atoms of a system individually. This is especially necessary when we compare e.g. $MgSiO_3$ with a hydrogen-bearing system (such as hydrated $MgSiO_3$). In the latter case, the large disparity in atomic weights and sizes means that the hydrogen continues to diffuse aggressively long after the other system components have stopped. This can skew the overall diffusivity rates, and, at first glance, lead the observer to conclude that the hydrated system is significantly more diffusive. As we shall see in a later set of results, this is not the case. Fig. 31 and 32 show the diffusivity of each species, grouped first according to temperature, and then by species, respectively.

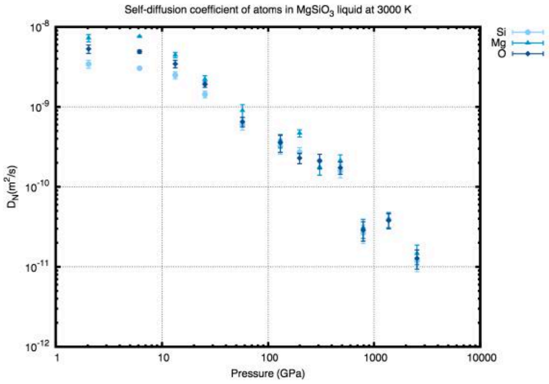
Self-diffusion coefficient of atoms in $MgSiO_3$ liquid at 3000 K
Si
Mg
O
$D_N(m^2/s)$
10^{-8}
10^{-9}
10^{-10}
10^{-11}
10^{-12}
1
10
100
1000
10000
Pressure (GPa)

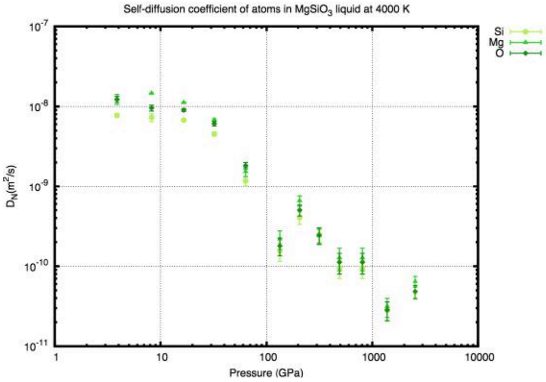
Self-diffusion coefficient of atoms in $MgSiO_3$ liquid at 4000 K
Si
Mg
O
$D_N(m^2/s)$
10^{-7}
10^{-8}
10^{-9}
10^{-10}
10^{-11}
1
10
100
1000
10000
Pressure (GPa)

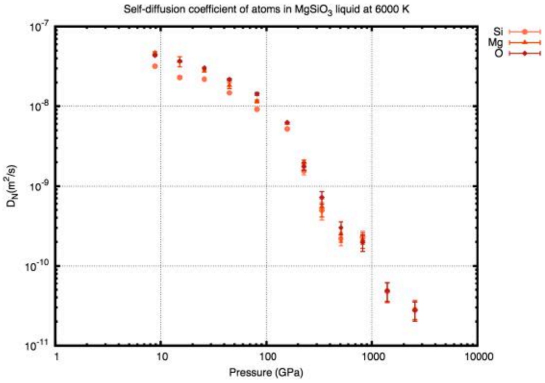
Self-diffusion coefficient of atoms in $MgSiO_3$ liquid at 6000 K
Si
Mg
O
$D_N(m^2/s)$
10^{-7}
10^{-8}
10^{-9}
10^{-10}
10^{-11}
1
10
100
1000
10000
Pressure (GPa)

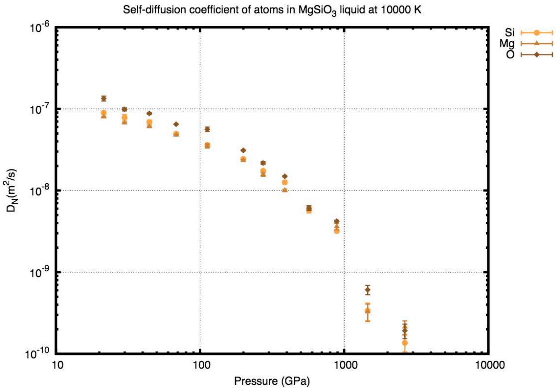
Self-diffusion coefficient of atoms in $MgSiO_3$ liquid at 10000 K
Si
Mg
O
$D_N(m^2/s)$
10^{-6}
10^{-7}
10^{-8}
10^{-9}
10^{-10}
10
100
1000
10000
Pressure (GPa)

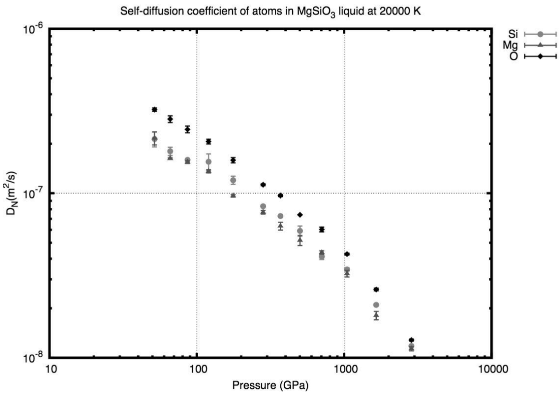

Figure 31: Diffusivity of Mg, Si and O in MgSiO$_3$ liquid, at temperatures ranging between 3000 K and 20,000 K and pressures ranging from 2 GPa to ~2.9 TPa, organized by temperature.

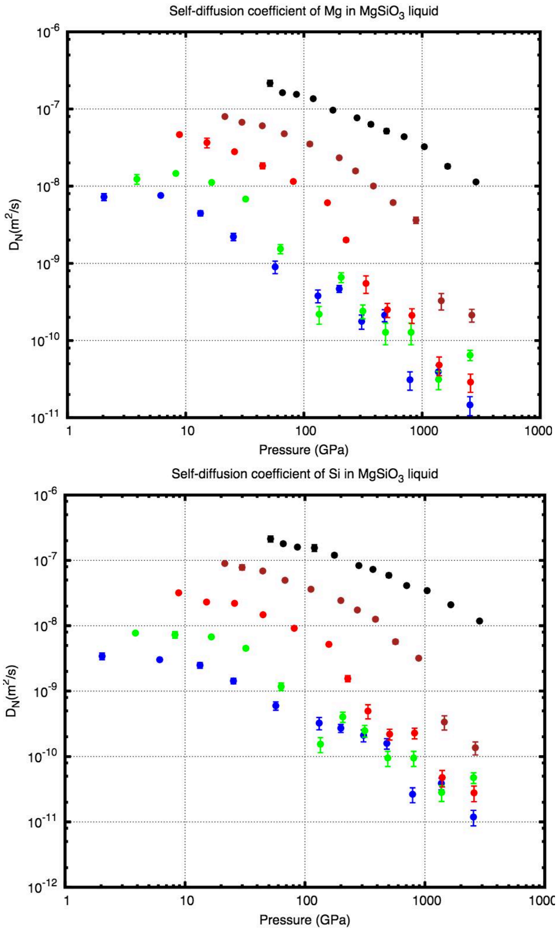

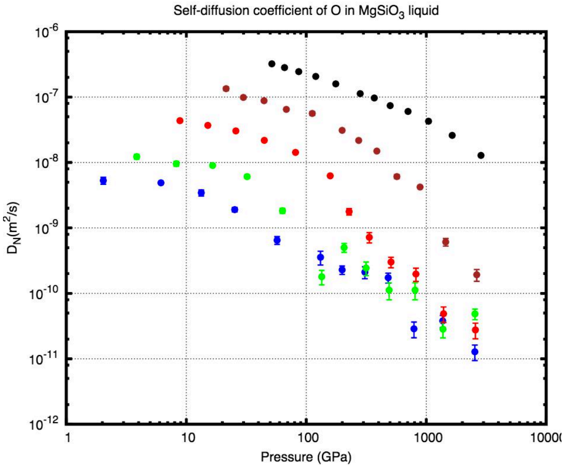

Figure 32: Diffusivity of Mg, Si and O in MgSiO$_3$ liquid, at temperatures ranging between 3000 K and 20,000 K and pressures ranging from 2 GPa to ~2.9 TPa, organized by species. The blue dots are at 3000 K, green 4000 K, red 6000 K, brown 10,000 K, black 20,000 K. Note that a formatting error removed the final '0' on the x axis – this should read 10,000 GPa.

Finally, it should be noted that the 20,000 K results always show a smooth curve in log-log space, unlike all other isotherms, suggesting that MgSiO$_3$ behaves entirely as a liquid across every examined pressure, without disruption. We will return to this finding at a later stage of the thesis.

5.4. HYDRATED MgSiO$_3$ STRUCTURAL PROPERTIES

Pressure is known to influence the speciation of water in hydrous silicate melts, with the lower pressure regimes being dominated by hydroxyls and water molecules, and the higher pressure (previously explored up to 135 GPa) regimes revealing a variety of species, including Si-O-H-O-Si polyhedral linkages O-H-O-H-chains, and edge decoration of SiO$_6$ octahedra with O-H-O molecules (Mookherjee et al., 2008). In our snapshot from relatively low pressure and low temperature conditions (see Fig. 12), we also find H$_2$O and OH units, in good agreement with the previous study.

5.5. HYDRATED MgSiO$_3$ THERMODYNAMIC PROPERTIES

5.5.1. EQUATION OF STATE

As per the unhydrated simulations, we first model the EOS on the Birch-Murgnahan third order EOS.

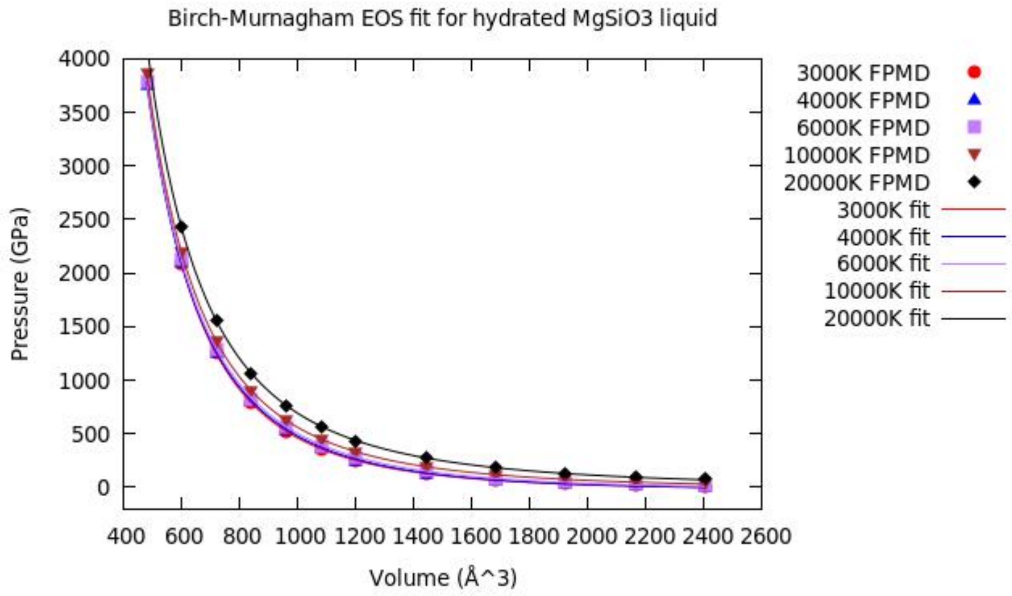

Figure 33: The BM-EOS for hydrous MgSiO$_3$ liquid, at temperatures ranging from 3000 K to 20000 K, and at pressures ranging from ~2 GPa to ~2.9 TPa. Note that the uncertainties in pressure are smaller than the FPMD symbols.

5.6. HYDRATED MgSiO$_3$ TRANSPORT PROPERTIES

5.6.1. MEAN SQUARED DISPLACEMENT

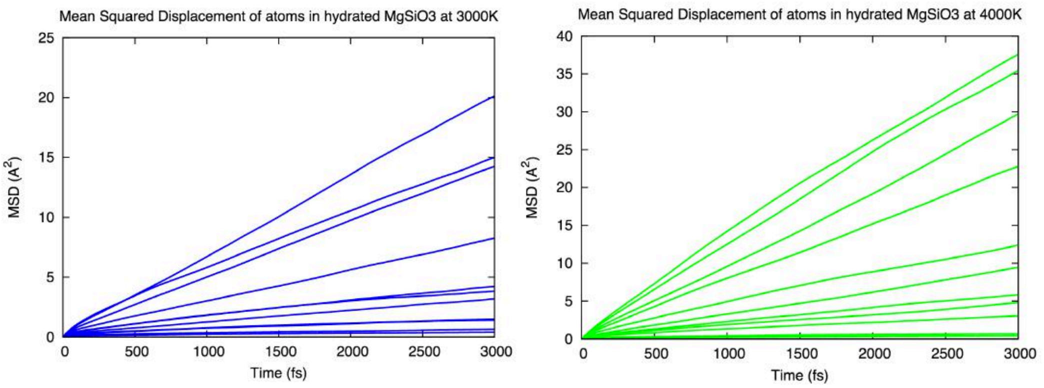

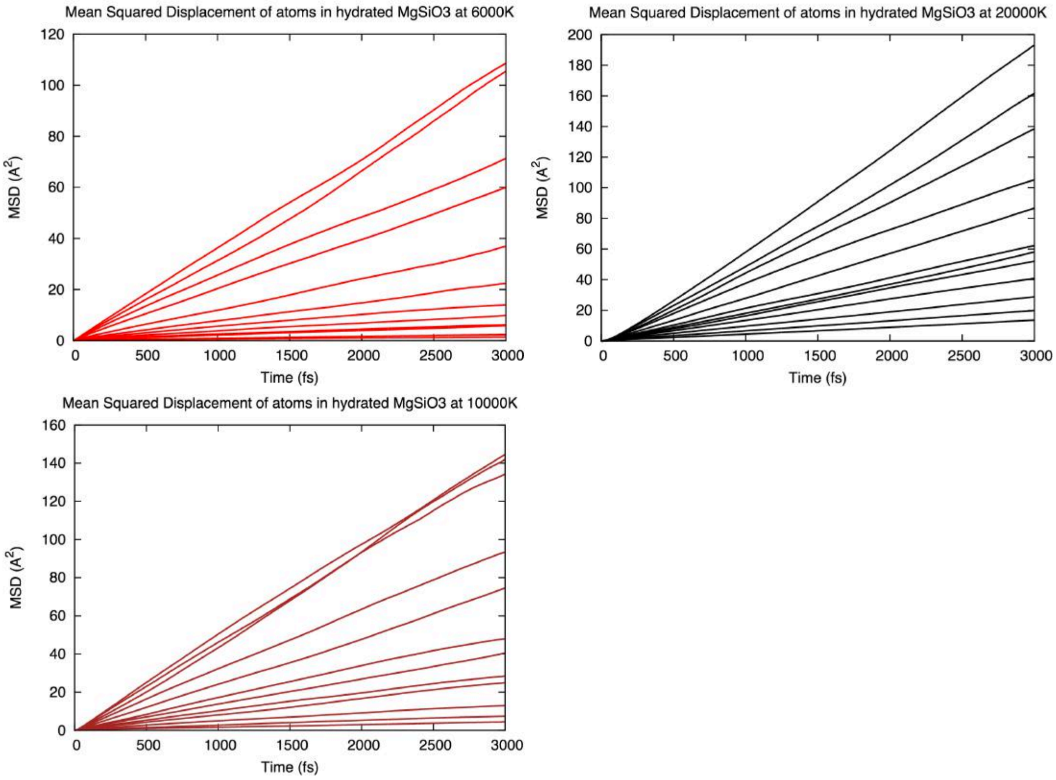

Figure 34: Mean Squared Displacements for atoms in hydrated $MgSiO_3$ liquid at temperatures ranging from 3000 K to 20,000 K. In each case, the line with the steepest gradient represents V/Vx = 1.0, while the line with the shallowest gradient represents V/Vx = 0.2. The blue lines are at 3000 K, green 4000 K, red 6000 K, brown 10,000 K, black 20,000 K.

Note that, as discussed earlier, the MSD’s are calculated as an average across all atoms in the system. The presence of hydrogen explains the comparatively steeper gradients of the hydrated system, despite the higher pressure on a per-volume basis (due to the inclusion of more atoms in the system).

5.6.2. SELF DIFFUSION COEFFICIENTS

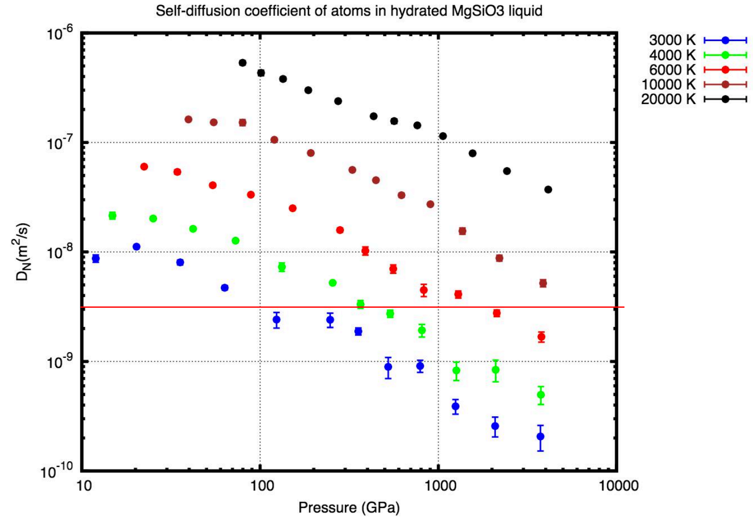

Figure 35: A log-log plot of the self-diffusion coefficient averaged across all atoms in the hydrated $MgSiO_3$ system, and across all temperatures. The area underneath the red line may be semi or fully vitrified, with a diffusion rate that averages roughly a typical Si-O bond length, or less.

Again, given that these results are averaged across all atoms, the presence of hydrogen is considerably raising the apparent diffusivity of the system as a whole. Thus, we need to examine the diffusivity of the component atoms before we can gain a clear picture of mass diffusion in the system.

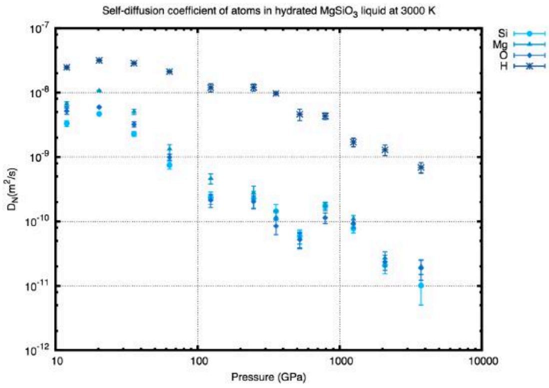

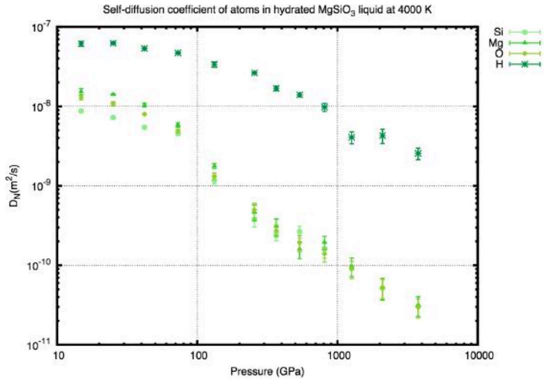

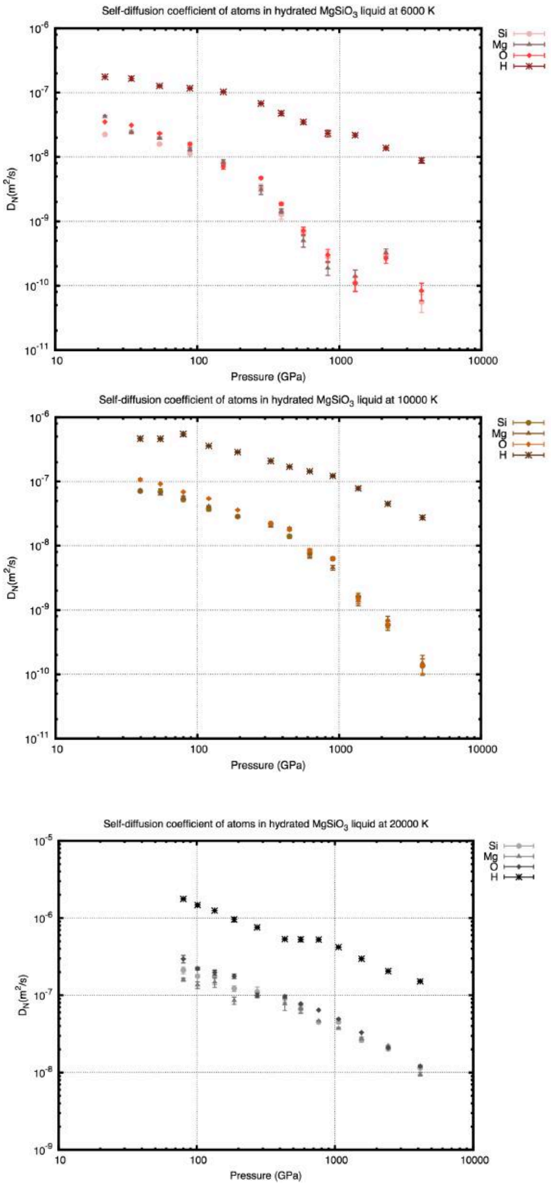

Figure 36: Diffusivity of Mg, Si, O and H in hydrated MgSiO$_3$ liquid, at temperatures ranging between 3000 K and 20,000 K and pressures ranging from 2 GPa to ~2.9 TPa, organized by temperature.

We can immediately see that hydrogen diffusivity is almost an order of magnitude greater than that of the other atomic species in the system, across all volumes and temperatures studied, and that the gap between hydrogen diffusivity and that of the other species increases with pressure.

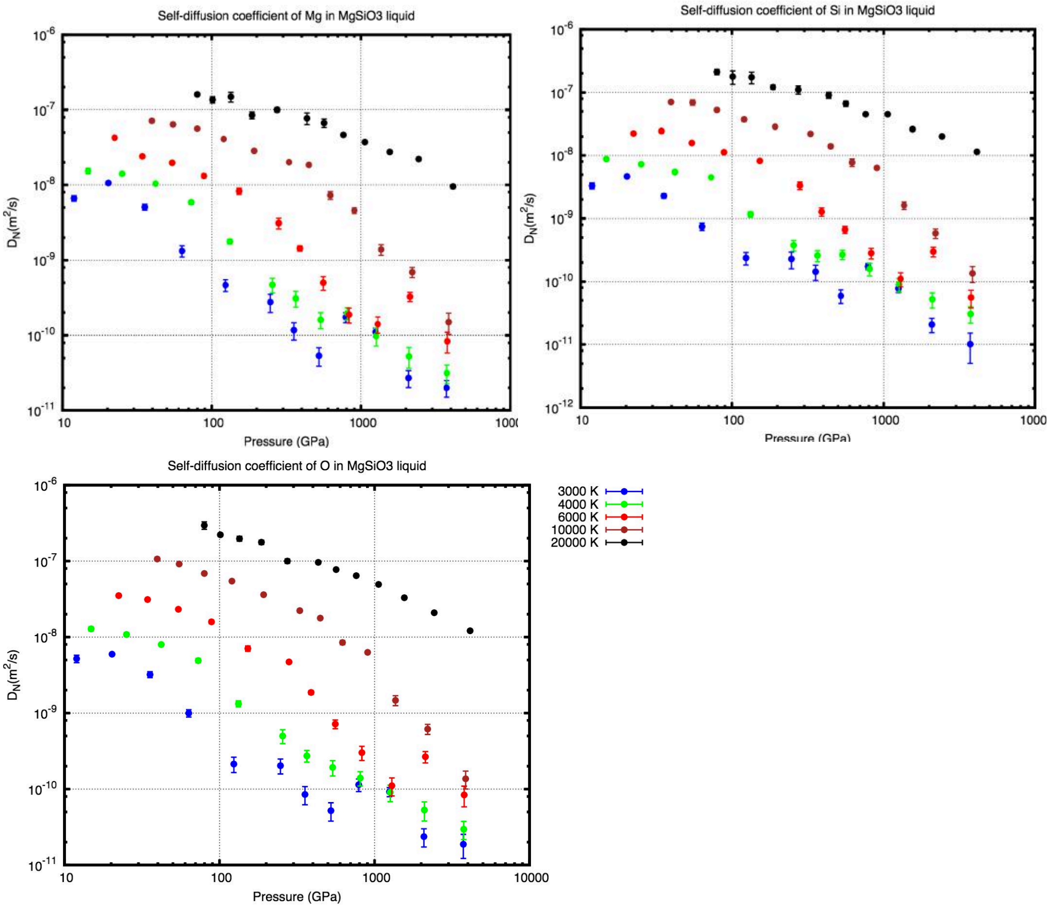

Figure 37: Diffusivity of Mg, Si, and O in hydrated MgSiO$_3$ liquid, at temperatures ranging between 3000 K and 20,000 K and pressures ranging from 2 GPa to ~2.9 TPa, organised by species. Please note that a small formatting error has obscured the x-axis of the top plots – the range should be read as 10,000 GPa at its uppermost boundary.

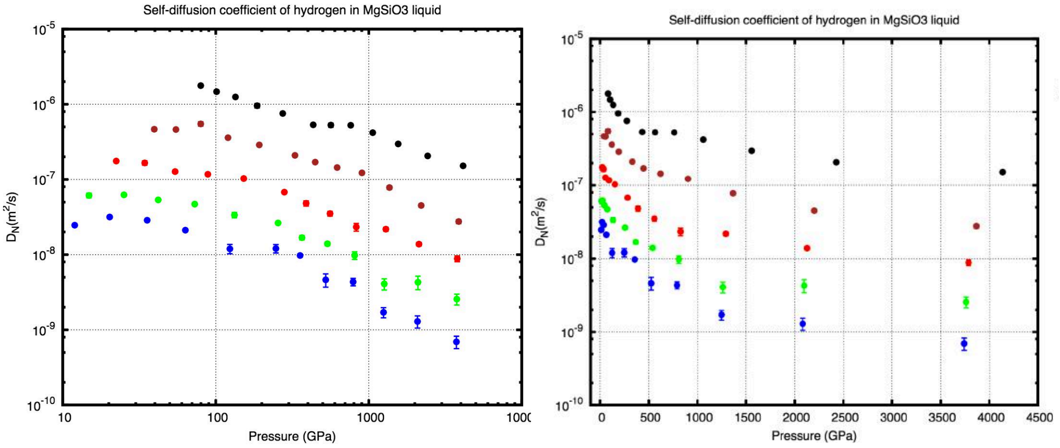

Figure 38: Diffusivity of hydrogen in hydrated MgSiO$_3$ liquid, shown in both log-log (left) and log-linear (right) format. Please note that a formatting error has obscured the x-axis of the top plot – the range should read as 10,000 GPa at its uppermost boundary. The blue dots are at 3000 K, green 4000 K, red 6000 K, brown 10,000 K, black 20,000 K. Note that the uppermost value of the x axis on the left plot should read 10,000 GPa

6. DISCUSSION, LIMITATIONS, FUTURE WORK

In this section, we will critically analyse the current body of work, paying particular attention to the robustness – and the limitations – of the given results, and their relevance to the Earth & Planetary Sciences. We will also make suggestions as to how the material in this thesis could be improved upon, in addition to highlighting some possible future avenues of research that could yield interesting outcomes.

The major structural change in $MgSiO_3$ liquid takes a remarkably simple form. The Si-O coordination number increases linearly with compression over a factor of five in volume. An exception here is the 20,000 K data, although this behaviour may be better explained by errors in post-processing, rather than fundamental differences in material properties at 10,000 K vs 20,000 K. The linear increase in coordination number with volume had previously been demonstrated over a factor of two in compression, corresponding to the pressure range of Earth's mantle (Stixrude & Karki, 2005). We extend these findings to much higher pressures here, comparable to those of super-Earth mantles. The maximum coordination number we find is eight.

At compressions greater than a factor of two compression becomes much more homogeneous as the liquid adopts a more close-packed arrangement of ions. The Si-O bond length initially increases on compression, but beyond V/Vx=0.5, it begins to decrease.

Although our results for the heat capacity still contain some uncertainty, it appears that the heat capacity decreases on compression. The heat capacity always exceeds the Dulong-Petit value characteristic of high temperature crystals, but closely approaches this value at the highest compressions. The large heat capacity of silicate liquids has previously been attributed to the additional structural degrees of freedom that they possess, and which are absent in a crystal (Stixrude & Karki, 2005). At high pressure, as the demands of close-packing become more restrictive, this structural freedom is diminished, accounting for the decrease in heat capacity with compression.

We find that the Grüneisen parameter increases on compression for $V/Vx > 0.5$, and then saturates and adopts a nearly constant value at higher compression. This result may be significant for magma oceans in super-Earths. Whereas the initial increase in Grüneisen parameter is important for understanding the steepness of the adiabatic temperature gradient in Earth's magma ocean, and the resultant initial crystallization from the mid-mantle and development of a basal magma ocean (Stixrude et al., 2009), super-Earth magma oceans may instead begin crystallizing from the bottom, and may not form basal magma oceans.

The activation volume governing self-diffusion decreases markedly with increasing pressure. From one perspective, our self-diffusion coefficients may reveal the limitations of the Arrhenius form, when applied to the very wide pressure-range explored herein. For example, extrapolation from the Arrhenius fits performed on lower-pressure FPMD results, to the conditions of super-Earth mantles, leads us to the inevitable conclusion that the self-diffusion coefficients reported here are much greater than expected. It logically follows that chemical exchange between magma oceans, the crystals freezing out of them and proto-cores in super-Earths are thus not so limited as might have been thought previously.

This conclusion is certainly valid, but it is only *unexpected* if we assume that the activation energy for self-diffusion is linear in pressure. The earlier results of e.g. De Koker et al. (2008) do indeed demonstrate this result. However, these earlier simulations reached much lower maximum pressures (~200 GPa), and covered a much smaller range, within which an Arrhenius fit was appropriate, as it accurately described the trends in the data. My initial finding that an Arrhenius fit is inappropriate over the pressure range explored in this work, does not necessarily demonstrate the limitations of the Arrhenius form for describing diffusivity in ultra-high pressure regimes, but instead illustrates the pressure-dependence of the activation energy is not linear at the conditions explored herein. The activation energy for a diffusing atom describes the difference between its energy at a starting position, and the energy barrier preventing further diffusion, both of which depend on quantum mechanical interactions with neighbouring atoms. We must therefore not expect the activation energy to be linear over pressure ranges as wide as those explored in the current work, where we have highly diffuse systems on one end, all the way to a range of ultra-compressed volumes, where atoms are packed extremely closely together. When dealing with such extremes, it is reasonable to assume that activation energies progress non-linearly.

In addition to the above, and in further considering the fundamental limitations of the current work, there are a number of key issues that should be addressed before any subsequent work is undertaken. One such issue involves how we identify vitrification in the system, and how that might affect the treatment of the data, and interpretation of the results. In this work, my method for ascertaining whether a given pressure-temperature regime led to vitrification, involved a mainly-qualitative method of examining the gradient of the MSD (averaged across species – another issue that we will address below), the mean diffusivity values, and the behaviour of the diffusivity data when visualised in a plot. Specifically, if the MSD gradient was very low, if atoms were moving, on average, less than roughly an atom's-length across the equilibrated portion of the simulation, and if the diffusivity data points began to fluctuate unpredictably, I assumed that the system was a partial-melt, or an amorphous glass. In either case, the system will have undergone a phase change from a liquid, to something else.

This is a crude, though nonetheless useful, method for estimating the basic state of the system. However, the more pressing issue is that this knowledge was not used to inform the treatment of my data in performing calculations, or in interpreting my results. For instance, in calculating my heat capacities, I take values obtained at given volumes, and then average them across a range of different temperatures. This was done, in the first instance, to compare to related earlier work (e.g. Karki et al. (2006)). However, it must be kept in mind that this earlier work spanned a much lower pressure and temperature range than that explored in the current work, and applying the same averaging method here may produce erroneous results due to the possibility of liquid-glass transitions, and the inclusion of data generated from vitrified systems. A more useful and reliable set of results for the thermodynamic properties of silicate liquids might be extracted from the data by *not* taking averaged values over such wide ranges, and by ensuring we do not include data generated from vitrified systems.

On the topic of averaged values, there's a further point to be made regarding the MSD results – and some of the self-diffusion results - given in this thesis, in terms of my calculations of system-averaged results. For example, we use the system-averaged MSD primarily as a basic diagnostic tool for helping judge whether the system is solid or liquid. As discussed previously, the limitations of this method (taking the average MSD of all atoms in the system) becomes apparent when the mass disparity between atoms in the system is relatively large, as is the case in the simulations that include hydrogen. As such, these averaged MSD results are arguably meaningless, outside of being a simple diagnostic tool, and a more useful set of results to include in this written work, would have been the MSD's for each of the constituent atoms in the system. This would have provided a set of quantitative results that could then have been compared to similar theoretical and experimental work completed by other researchers.

Finally, it is always desirable to ensure that the results generated through the course of a given investigation, are applied to understanding the original questions and context of the research. In this case, the original goal of my research was to use FPMD simulations to greater understand the nature of silicate liquids at temperature-pressure conditions relevant to giant impacts and super-Earth interiors. Regarding the latter, it would have been highly instructive to plot our various results atop relevant geotherms, and thus to eliminate data points that do not further our understanding of the central questions of the research. For example, it is highly unlikely that data generated for silicate materials at a temperature of 20,000 K and a pressure of 2 GPa would bear any kind of relevance to understanding super-Earth interiors, as these conditions would not exist there. Unfortunately, time restrictions prevented me from performing these analyses.

Improvements could also be made on the results that have already been generated. For example, while the third-order Birch-Murnaghan equation of state has been demonstrated to accurately represent the equation of state of silicate liquids across the pressure and temperature range of Earth's mantle (Stixrude & Karki, 2005; De Koker & Stixrude, 2009), this order of finite strain expansion may not be sufficient for the conditions explored in this work, which may require a fourth, or higher, order expansion. Some bias may therefore exist in the given values of V_0, K_0 and K_0'.

Given that we have already found good agreement between our $MgSiO_3$ calculations and earlier work, with respect to heat capacity and Grüneisen parameter, we thus are able to process these results in alternative manners, as is necessity in the case of hydrated $MgSiO_3$. As an example, we can calculate the heat capacities and Grüneisen parameters on a per-atom basis for all simulations, and visualize results as a function of pressure rather than volume. This will allow for a more 'fair' comparison of these properties across materials.

The raw data from simulations can be used to conduct a study of speciation in the particular case of hydrated $MgSiO_3$, to expand on the work completed by Mookherjee et al., 2008. Of particular interest could be the exploration of proton conductivity and its relationship with electrical conductivity in hydrated silicates; which of these dominates in extreme conditions, and are there any implications for electromagnetic field generation? What can we learn from studies of density, viscosity, and partial molar volume? Does the prediction of unlimited solubility of water across mantle conditions hold for the pressure-temperature regime of super-Earth mantles (Mookherjee et al., 2008)? This could have important implications for the ability of early-stage, molten super-Earths to act as a reservoir for the storage and delivery of water to its surface as it evolves, and thus, for the likelihood of finding life outside our solar system.

The importance of carbon in Earth's mantle is arguably much greater than its rather modest abundance (Hayden & Watson, 2008). The methods we have used could be extended to the $MgSiO_3$-CO_2 system. Can we learn something about the solubility and density of CO_2 in silicate melts, and, if so, what relevance might this information have? Recent seismic research has uncovered pervasive upper-mantle melting of carbonates under the Western USA (Hier-Majumder & Tauzin, 2017), and it is thought that the core and mantle contain vastly more carbon than all of the near-surface reservoirs combined (Shcheka et al., 2006). With careful processing, the data should provide some insight into the structural, thermodynamic, and, importantly, the transport properties of carbon in silicate melts.

This thesis represents a reasonable first step toward a complete set of results for all materials studied, including $MgSiO_3$, and hydrated $MgSiO_3$, across a wide temperature and pressure regime. Indeed, throughout the course of this work, I have identified some of the limitations of previously-used analytical methods in addressing these extremes of temperature and pressure, and, in doing so, my hope is that I will have helped guide future research in the field, and aided in the generation of more reliable results. The results given here, and that of any future related work, may have important implications for our understanding of the behavior of silicate liquids in super-Earth magma oceans, and as the result of high velocity impacts. The work being produced via FPMD simulations will motivate experimental studies of the structure and physical properties of amorphous silicates over a wider pressure-temperature regime than has hitherto been explored.

7. CONCLUSION

We use first-principles molecular dynamics to examine the structural, thermodynamic and transport properties of silicate liquids in the extreme conditions associated with super-Earth mantles and giant impacts. For the purposes of this study, temperatures range between 3000 K and 20,000 K, with pressures of up to ~4 TPa. We focus primarily on $MgSiO_3$ liquid, with some initial results reported for the hydrated form, with approximately 10 wt% water.

We find that mean Si-O coordination in $MgSiO_3$ increases linearly with pressure, from between 4 and 4.5 at conditions in the upper mantle of Earth (~2 GPa), to between 6 and 6.5 in Earth's lower mantle (~130 GPa), and finally to between 8 and 8.5 in the conditions associated with super-Earth mantles and giant impacts (~2.5 to 3 TPa).

Average heat capacity, in the case of $MgSiO_3$ decreases on compression from ~4.6 N k at the reference volume of $V/V_x=1$ to ~3.35 N k at the highest compression level of $V/V_x=0.2$. The latter value reports only the results obtained using the 'finite differences' method of analysis rather than those obtained using the fluctuation method, which was discovered to be unreliable for higher temperature runs using the techniques applied here. This issue has since been investigated and corrected (see Supporting Information in Scipioni *et al.* 2017).

REFERENCES

Adjaoud, O., Steinle-Neumann, G., Jahn, S., 2011. Transport properties of Mg_2SiO_4 liquid at high pressure: Physical state of a magma ocean. *Earth Plan. Sci. Lett.* 312, 463 – 470. doi:10.1016/j.epsl.2011.10.025

Ai, Y., and Lange, R.A., 2008. New acoustic velocity measurements on CaO-MgO-Al_2O_3-SiO_2 liquids: Reevaluation of the volume and compressibility of $CaMgSi_2O_6$-$CaAl_2Si_2O_8$ liquids to 25 GPa. *JGR Solid Earth*, 113, B4203.

Alle, M.P., Tildsley, D.J., 1987. *Computer Simulations of Liquids.* Oxford, Clarendon Press, UK.

Arp, V., Persichetti, J.M., Chen, G., 1984. The Grüneisen Parameter in Fluids. *J. Fluids Eng.* 106, 193–200. doi:10.1115/1.3243100

Asimow, P.D., 2012. Shock compression of preheated silicate liquids: Apparent universality of increasing Grüneisen parameter upon compression. *Shock Compress. Condense. Matter.* 2011 (Pt 1 & 2), 1426.

Barboni, M., Boehnke, P., Keller, B., Kohl, I.E., Schoene, B., Young, E.D., McKeegan, K.D., 2017. Early formation of the Moon 4.51 billion years ago. *Sci. Adv. 3*, e1602365. doi:10.1126/sciadv.1602365

Born, R., Oppenheimer, R., 1927. *Ann. Phys. (N.Y.)* 389, 457

Brandon, A., 2007. Planetary science: A younger Moon. *Nature* 450, 1169–1170. doi:10.1038/4501169a

Buehler, M.J., 2011. Continuum and Particle methods: Property Calculation II [Powerpoint Presentation], *Introduction to Modelling and Simulation, MIT.* Available at: https://ocw.mit.edu/courses/materials-science-and-engineering/3-021j-introduction-to-modeling-and-simulation-spring-2012/part-i-lectures-readings/MIT3_021JS12_P1_L4.pdf

Burkhardt, C., 2014. Isotopic Composition of the Moon and the Lunar Isotopic Crisis, in: Cudnik, B. (Ed.), *Encyclopedia of Lunar Science.* Springer International Publishing, pp. 1–13. doi:10.1007/978-3-319-05546-6_20-1

Canup, R.M., Asphaug, E., 2001. Origin of the Moon in a Giant Impact near the End of the Earth's Formation. *Nature* 412, 708-712.

Canup, R.M., 2004. Simulations of a late lunar-forming impact. *Icarus* 168, 433–456. doi:10.1016/j.icarus.2003.09.028

Canup, R.M., 2012. Forming a Moon with an Earth-Like Composition via a Giant Impact. *Science* 338, 6110, 1052-1055 doi:1126/science.1226073

Car, R., Parrinello, M., 1985. Unified Approach for Molecular Dynamics and Density-Functional Theory. *Phys. Rev. Lett.* 55, 2471–2474. doi:10.1103/PhysRevLett.55.2471

Ceperley, D.M., Alder, B.J., 1980. Ground State of the Electron Gas by a Stochastic Method. *Phys. Rev. Lett.* 45, 566–569. doi:10.1103/PhysRevLett.45.566

Chandler, D., 1987. *Introduction to Modern Statistical Mechanics*. Oxford University Press.

Chen, G.Q., Ahrens, T.J., Stolper, E.M., 2002. Shock-wave equation of state of molten and solid fayalite. *Phys. of Earth Plan. Int.* 134, 1-2, 35-52.

Ciesla, F.J., Davison, T.M., Collins, G.S., O’Brien, D.P., 2013. Thermal consequences of impacts in the early solar system. *Meteorit. Planet. Sci.* 48, 2559–2576. doi:10.1111/maps.12236

Courtial, P., Ohtani, E., Dingwell, D.B., 1997. High-temperature densities of some mantle melts. *Geo. et Cosmo. Acta* 61, 15, 3111-3119.

Crawford, D.A., Schultz, P.H., 1993. The production and evolution of impact-generated magnetic fields. *Int. Jour. of Impact Eng.* 14, 1-4, 205-216.

Ćuk, M., Stewart, S.T., 2012. Making the Moon from a Fast Spinning Earth: A Giant Impact Followed by Resonant Despinning. *Science* 338, 6110, 1047-1052.

Ćuk, M., Hamilton, D.P., Lock, S.J., Stewart, S.T., 2016. Tidal evolution of the Moon from a high-obliquity, high-angular-momentum Earth. *Nature* 539, 402–406. doi:10.1038/nature19846

Davies, G.F., 1982. Ultimate strength of solids and formation of planetary cores. *Geophys. Res. Lett.* 9, 11, 1267-1270.

De Koker, N.P., and Stixrude, L., 2009. Self-consistent thermodynamic description of silicate liquids, with application to shock melting of MgO periclase and MgSiO3 perovskite. *Geophys. J. Int.* 178, 162-179.

De Koker, N.P., Stixrude, L., Karki, B.B., 2008. Thermodynamics, structure, dynamics, and freezing of Mg2SiO4 liquid at high pressure. *Geo. et Cosmo. Acta* 72, 1427-1441.

Demichelis, R., Civalleri, B., Ferrabone, M., Dovesi, R., 2010. On the performance of eleven DFT functionals in the description of the vibrational properties of aluminosilicates. *Int. J. Quantum Chem.* 110, 406–415. doi:10.1002/qua.22301

De Pater, I., Lissauer, J.J., 2015. *Planetary Sciences.* Cambridge University Press.

Elkins-Tanton, L.T., 2012. Magma Oceas in the Inner Solar System. Ann. Rev. *Earth & Plan. Sci*. 40, 113-139

Elardo, S.M., Draper, D.S., Shearer, C.K., 2011. Lunar Magma Ocean crystallization revisted: Bulk composition, early cumulate mineralogy, and the source regions of the highlands Mg-suite. *Geo. et. Cosmo. Acta* 75, 11, 3024-3045

Feynman, R.P., 1939. Forces in Molecules. *Phys. Rev.* 56,4, 340.

Fock, V., 1930b. Naherungsmethode zur Losung des quantenmechanischen Mehrkorperproblems. *Zeitschrift für Physik*, 61, 126-148

Gerstenkorn, H., 1969. The Earliest Past of the Eath-Moon System. *Icarus* 11, 189-207.

Ghosh, D.B., Karki, B.B., 2017. Transport properties of carbonated silicate melt at high pressure. *Sci. Adv.* 3, 12, e1701840, doi: 10.1126/sciadv.1701840

Giustino, F., 2014. *Materials modelling using density functional theory : properties and predictions* | UTS Library. Oxford University Press.

Gomes, R., Levison, H.F., Tsiganis, K., Morbidelli, A., 2005., Origin of the Cataclysmic Late Heavy Bombardment Peroid of the Terrestrial Planets. *Nature* 435, 466-469.

Grossfield, A., Zuckerman, D.M., 2009. Quantifying uncertainty and sampling quality in biomolecular simulations. *Annu. Rep. Comput. Chem.* 5, 23–48. doi:10.1016/S1574-1400(09)00502-7

Hayden, L.A., Watson, E.B., 2008. Grain boundary mobility of carbon in Earth's mantle: a possible carbon flux from the core. *Proc. Nat. Acad. Sci.* USA. 105, 8537-8541.

Harrison, N.M., 2003. *An introduction to density functional theory.* ResearchGate.

Hartmann, W.K., 2014. The giant impact hypothesis: past, present (and future?). *Philos. Trans. R. Soc. Lond. Math. Phys. Eng. Sci.* 372, 20130249. doi:10.1098/rsta.2013.0249

Hartmann, W.K., Davis, D.R., 1975. Satellite-sized planetesimals and lunar origin. *Icarus* 24, 504–515. doi:10.1016/0019-1035(75)90070-6

Hartmann, W.K., 1997, A Brief History of the Moon. *The Planetary Report.* 17, 4-11.

Hier-Majumder, S., Tauzin, B., 2017. Pervasive upper mantle melting beneath the Western US. *Earth Planet. Sci. Lett.* 463, 25–35. doi:10.1016/j.epsl.2016.12.041

Hoover, W.G., 1985. Canonical dynamics: Equilibrium phase-space distributions. *Phys. Rev. A* 31, 1695–1697. doi:10.1103/PhysRevA.31.1695

Hohenburg, P., Kohn, W., 1964. Inhomogenous Electron Gas. *Phys. Rev.* 136, B864.

Hugoniot, P.H., 1887. Mémoire sur la propagation du mouvement dans les corps et ples spécialement dans les gaz parfaits. 1 Partie, *J. Ecole Polytech*. (Paris), 57, 3-97.

Hugoniot, P.H., 1889. Mémoire sur la propagation du mouvement dans les corps et plus spécialement dans les gaz parfaits, 2 Partie, *J. Ecole Polytech*. (Paris), 58,1-125.

Jeanloz, R.,Roufosse, M., 1982. Anharmonic properties: Ionic model of the effects of compression and coordination change. *JGR Solid Earth* 87, B13, 10763-10772.

Jing, Z., and Karato, S., 2011. A new approach to the equation of state of silicate melts: An application of the theory of hard sphere mixtures. *Geo. et Cosmo. Acta* 75, 6780-6802.

Jones, R.O., Gunnarsson, O., 1989. The density functional formalism, its applications and prospects. *Rev. Mod. Phys.* 61, 689–746. doi:10.1103/RevModPhys.61.689

Karki, B.B., Bhattarai, D., Stixrude, L., 2006. First-principles calculations of the structural, dynamical, and electronic properties of liquid MgO. *Phys. Rev. B* 73, 174208. doi:10.1103/PhysRevB.73.174208

Karki, B.B., Bhattarai, D., Stixrude, L., 2007. First-principles simulations of liquid silica: structural and dynamical behaviour at high pressure. *Phys. Rev. B* 76, 10.

Karki, B.B., Stixrude, L., Wentzcovitch, R.M., 2001. High-pressure elastic properties of major materials of Earth's mantle from first principles. *Rev. Geophys.* 39, 507–534. doi:10.1029/2000RG000088

Karki, B.B., Stixrude, L.P., 2010. Viscosity of MgSiO3 Liquid at Earth's Mantle Conditions: Implications for an Early Magma Ocean. *Science* 328, 740-742. doi: 10.1126/science.1188327

Kohn, W., Sham, L.J., 1965. Self-Consistent Equations Including Exchange and Correlation Effects. *Phys. Rev.* 140, A1133–A1138. doi:10.1103/PhysRev.140.A1133

Kresse, G., Hafner, J., 1993. Ab Initio Molecular Dynamics for Liquid metals. *Phys. Rev. B.* 47. 558.

Kresse, G., Furthmiller, J., 1996. Efficient Iterative Schemes for ab Initio Total-Energy Calculations Using a Plane-Wave Basis Set. *Phy. Rev. B* 54, 11169-11186.

Lacks, D.J., Rear, D.B., Orman, V., 2007. molecular dynamics investigation of viscosity, chemical diffusivities and partial molar volumes of liquids along the $MgO-SiO_2$ joins as functions of pressure. *Geo. et Cosmo. Acta* 71, 1312-1323

Lange, R.A., Carmichael, I.S.E., 1987. Densities of Na2O-K2O-CaO-MgO-FeO-Fe2O3-Al2O3-TiO2-SiO2 liquids: New measurements and derived partial molar properties. *Geo. et Cosmo. Acta* 51, 2931–2946. doi:10.1016/0016-7037(87)90368-1

Levy, M., 1979. Universal variational functionals of electron densities, first-order density matrices, and natural spin-orbitals and solution of the v-representability problem. *Proc. Natl. Acad. Sci.* U. S. A. 76, 6062–6065.

Lieb, E.H., 1983. Density functionals for coulomb systems. *Int. J. Quantum Chem.* 24, 243–277. doi:10.1002/qua.560240302

Low, F.J., Young, E., Beintema, D.A., Gautier, T.N., Beichman, C.A., Aumann, H.H., Gillett, F.C., Neugebauer, G., Boggess, N., Emerson, J.P., 1984. Infrared cirrus - New components of the extended infrared emission. *Astrophys. J.* 278, L19–L22. doi:10.1086/184213

Melosh, H.J., 1989. *Impact Cratering.* Oxford University Press, NY.

McQuarrie, D.A., 2000. *Statistical Mechanics*. University Science Books.

Mermin, N.D., 1965. Thermal Properties of the Inhomogeneous Electron Gas. *Phys. Rev.* 137, A1441–A1443. doi:10.1103/PhysRev.137.A1441

Millot, M., Dubrovinskaia, N., Černok, A., Blaha, S., Dubrovinsky, L., Braun, D.G., Celliers, P.M., Collins, G.W., Eggert, J.H., Jeanloz, R., 2015. Shock Compression of Stishovite and melting of Silica at Panetary Interior Conditions. *Science* 347, 6220, 418-420.

Mitler, H.E., 1975. Formation of an Iron-Poor Moon by Partial Capture, or: Yet Another Exotic Theory of Lunar Origin. *Icarus* 24, 256-268

Mookherjee, M., Stixrude, L., Karki, B., 2008. Hydrous silicate melt at high pressure. *Nature* 452, 983–986. doi:10.1038/nature06918

Morishima, R., Watanabe, S., 2004. Co-accretion of the Earth-Moon system after the Giant Impact: Reduction of the Total Angular Momentum by Lunar Impact Ejecta. *Icarus* 168(1), 60-79

Mosenfelder, J.L., Asimow, P.D., Ahrens, T.J., 2007. Thermodynamic properties of Mg2SiO4 liquid at ultra-high pressures from shock measurements to 200 GPa on forsterite and wadsleyite. *Journ. Geophys. Res.* 112, B6, doi.org/10.1029/2006JB004364

Murakami, M., Sinogeikin, S.V., Bass, J.D., Sata, N., Ohishi, Y., Hirose, K., 2007. Sound velocity of $MgSiO_3$ post-perovskite phase: A constraint on the D" discontinuity. *Earth and Plan. Sci. Lett.* 259, 1-2, 18-23.

Nevins, D., Spera, F.J., Ghiorso, M.S., 2009. Shear viscosity and diffusion in liquid MgSiO3: Transport properties and implications for terrestrial planet magma oceans. *Am. Mineral*. 94, 975–980. doi:10.2138/am.2009.3092

Nosé, S., 1984. A unified formulation of the constant temperature molecular dynamics methods. *J. Chem. Phys.* 81, 511–519. doi:10.1063/1.447334

Öpik, E.J., 1972, Comments on Lunar Origin. *Irish Astron. J.* 10, 190

Pahlevan , K., Morbidelli, A., 2015. Collisionless Encounters and the Origin of Lunar Inclination. *Nature* 527, 7579, 492-494.

Oran, R., Shprits, Y., Weiss, B.P., 2016. Can Impact-Amplified Magnetic Fields be Responsible for Magnetization on the Moon? *Proc. Lunar Planet. Sci. Conf.* 47th, 3057.

Perdew, J.P., Burke, K., Ernzerhof, M., 1996. Generalized Gradient Approximation Made Simple. *Phys. Rev. Lett.* 77, 3865–3868. doi:10.1103/PhysRevLett.77.3865

Perdew, J.P., Ruzsinszky, A., Csonka, G.I., Vydrov, O.A., Scuseria, G.E., Constantin, L.A., Zhou, X., Burke, K., 2008. Restoring the Density-Gradient Expansion for Exchange in Solids and Surfaces. *Phys. Rev. Lett.* 100, 136406. doi:10.1103/PhysRevLett.100.136406

Quintana, E.V., Barclay, T., Borucki, W., Rowe, J.F., Chambers, J.E., 2016. The Frequency of Giant impacts on Earth-like Worlds. *Astrophys. J.* 821, 126.

Rankine, W.J.M., 1870a. On the thermodynamic theory of waves of finite longitudinal disturbance, (Read 16th Dec 1869). *Phil. Trans. Roy. Soc. London* 160, 277-286.

Rankine, W.J.M., 1870b. On the thermodynamic theory of waves of finite longitudinal disturbance, *Phil. Trans. Roy. Soc. London* 160, 287-288.

Refson, K., 2001. *Moldy User's Manual*. Department of Earth Sciences, University of Oxford, UK.

Rigden, S.M., Ahrens, T.J., Stolper, E.M., 1988. Shock compression of molten silicate: Results for a model basaltic composition. *JGR Solid Earth* 93, B1, 367-382.

Robertson, E., 2007. The Interior of the Earth. *Geological Survey of the USA*. Available at: https://pubs.usgs.gov/gip/interior/ (accessed 1.20.17).

Rosenfeld, Y., Tarazona, P., 1998. Density functional theory and the asymptotic high density expansion of the free energy of classical solids and fluids. *Mol. Phys.* 95, 141–150. doi:10.1080/00268979809483145

Rufu, R., Aharonson, O., Perets, H.B., 2017. A multiple-impact origin for the Moon. *Nat. Geosci.* 10, 89–94. doi:10.1038/ngeo2866

Sakamaki, T., Suzuki, A., Ohtani, E., 2006. Stability of hydrous melt at the base of Earth's upper mantle. *Nature* 439, 192-194.

Schrödinger, E., 1926. An Undulatory Theory of the Mechanics of Atoms and Molecules. *Phys. Rev*. 6, 1049-1070

Scipioni, R., Stixrude, L., Desjarlais, M.P., 2017. Electrical conductivity of SiO2 at extreme conditions & planetary dynamos. *PNAS* 114 (34), 9009-9013.

Shcheka, S.S., Wiedenbeck, M., Frost, D.J., Keppler, H., 2006. Carbon solubility in mantle minerals. *Earth Planet. Sci. Lett*. 245, 730–742. doi:10.1016/j.epsl.2006.03.036

Spaulding, D.K., McWilliams, R.S., Jeanloz, R., Eggert, J.H., Celliers, P.M., Hicks, D.G., Collins, G.W., Smith, R.F., 2012. Evidence for a Phase Transition in Silicate Melt at Extreme Pressure and Temperature Conditions. *Phys. Rev. Lett.* 108, 65701. doi:10.1103/PhysRevLett.108.065701

Spera, F., Ghiorso, M.S., Nevins, D., 2011. Structure, themodynamic and transport properties of liquid $MgSiO_3$. *Geo. et Cosmo. Acta* 75, 1272-1296.

Stixrude, L., De Koker, N., Sun, N., Mookherjee, M., Karki, B.B., 2009. Thermodynamics of silicate liquids in the deep Earth. *Earth Planet. Sci. Lett*. 278, 226–232. doi:10.1016/j.epsl.2008.12.006

Stixrude, L., Karki, B., 2005. Structure and Freezing of MgSiO3 Liquid in Earth’s Lower Mantle. *Science* 310, 297–299. doi:10.1126/science.1116952

Stixrude, L., Lithgow-Bertelloni, C., 2005. Thermodynamics of mantle minerals – I. Physical properties. *Geophys. J. Int.* 162, 610–632. doi:10.1111/j.1365-246X.2005.02642.x

Stixrude, L., 2014. Melting in Super-Earths. Phil. Trans. R. Soc. A. 372. 20130076

Sugiura., N., Strangway, D.W., 1980. Comparison of magnetic paleointensity methods using a lunar sample. *Proc. Lunar Planet. Sci. Conf.* 11th, 1801-1813.

Sun, N., Stixrude, L., De Koker, N., Karki, B.B., 2011. First principles molecular dynamics simulations of diopside (CaMgSi2O6) liquid to high pressure. *Geo. et Cosmo. Acta* 75, 3792–3802. doi:10.1016/j.gca.2011.04.004

Swope, W.C., Andersen, H.C., Berens, P.H., Wilson, K.R., 1982. A computer simulation method for the calculation of equilibrium constants for the formation of physical clusters of molecules: Application to small water clusters. *J. Chem. Phys.* 76, 637–649. doi:10.1063/1.442716

Tarduno, J.A., Cotrell, R.D., Davis, W.J., Nimmo, F., Bono, R.K., 2015. *Science*. 349, 6247, 521-524.

Tonks, B., Melosh, H.J., 1993. Magma Ocean Formation due to Giant Impacts. *Journ. Geophys. Res. Plan.* 98, E3, 5319-5333.

Touma, J., Wisedom, J., 1998. Resonances in the Early Evolution of the Earth-Moon System. *Astro. J.* 115, 1653-1163.

Van de Walle, A., Ceder, G., 1999. Correcting overbinding in local-density-approximation calculations. *Phys. Rev*. B 59, 14992–15001. doi:10.1103/PhysRevB.59.14992

Vočadlo, L., Alfè, D., Gillan, M.J., Price, G.D., 2003. The properties of iron under core conditions from first principles calculations. *Phys. Earth Plan. Int*. 140, 101-125.

Vorberger, J., Tamblyn, I., Militzer, B., Bonev, S.A., 2007. Hydrogen-helium mixtures in the interiors of giant planets. *Phys. Rev. B* 75, 24206. doi:10.1103/PhysRevB.75.024206

Ward, W.R., Canup, R., 2000. Origin of the Moon's Orbital Inclination from Resonant Disk Interactions. *Nature* 403(6771), 741-743.

Wasserman, E., Stixrude., L., Cohen, R.E., 1996. Thermal properties of iron at high pressures and temperatures. *Phys. Rev. B* 53, 8296-8303.

Weidenschilling, S.J., Greenberg, R., Chapman, C.R., Davis, D.R., Hartmann, W.K., 1986. Origin of the moon from a circumterrestrial disk. *Presented at the Origin of the Moon, Kona, HI.* pp. 731–762.

Wiechert, U., Halliday A.N., Lee, D., Snyder., G., Taylor, L., Rumble, D., 2001. Oxygen Isotopes and the Moon-Forming Giant Impact. *Science* 294, 5541, 345-348

Wood, J.A., 1972. Thermal History and Early Magnetism in the Moon, *Icarus*16, 2, 229-240.

Williams, Q., Garnero, E.J., 1996. Seismic evidence for partial melt at the base of Earth's mantle. *Science* 273, 5281, 1528-1530.

Young, E.D., Kohl, I.E., Warren, P.H., Rubie, D.C., Jacobson, S.A., Morbidelli., A., 2016. Oxygen Isotope Evidence for Vigorous Mixing during the Moon-forming Giant Impact. *Science* 351, 6272, 493-496.

Ziegler, L.B., Stegman, D.R., 2013. Implications of a long-lived basal magma ocean in generating Earth’s ancient magnetic field. *Geochem. Geophys. Geosys.* 14, 4735–4742. doi:10.1002/2013GC005001